STUDIES IN VORTEX MOTION

Thesis by

Gregory Richard Baker

In Partial Fulfillment of the Requirements

for the Degree of

Doctor of Philosophy

California Institute of Technology

Pasadena, California

1977

(Submitted September 21, 1976)

ACKNOWLEDGEMENTS

I have enjoyed completing this thesis under the supervision of Professor Phillip Saffman. I greatly appreciate his insight and encouragement. I thank Dr. Fausto Milinazzo and Dr. Bengt Fornberg for many useful discussions on the numerical techniques used in this thesis.

Financial support during my stay here at Caltech has been gratefully received through CIT Tuition Scholarships and Teaching Assistantships.

STUDIES IN VORTEX MOTION

ABSTRACT

This thesis covers four different problems in the understanding of vortex sheets, and these are presented in four chapters.

In Chapter 1, free streamline theory is used to determine the steady solutions of an array of identical, hollow or stagnant core vortices in an inviscid, incompressible fluid. Assuming the array is symmetric to rotation through π radians about an axis through any vortex centre, there are two solutions or no solutions depending on whether $A^{1/2}/L$ is less than or greater than 0.38 where A is the area of the vortex and L is the separation distance. Stability analysis shows that the more deformed shape is unstable to infinitesimal symmetric disturbances which leave the centres of the vortices undisplaced.

Chapter 2 is concerned with the roll-up of vortex sheets in homogeneous fluid. The flow over conventional and ring wings is used to test the method of Fink and Soh (1974). Despite modifications which improve the accuracy of the method, unphysical results occur. A possible explanation for this is that small scales are important and an alternate method based on "Cloud-in-Cell" techniques is introduced. The results show small scale growth and amalgamation into larger structures.

The motion of a buoyant pair of line vortices of opposite circulation is considered in Chapter 3. The density difference between the fluid carried by the vortices and the fluid outside is considered small, so that the Boussinesq approximation may be used. A macroscopic model is developed which shows the formation of a detrainment filament and this is included as a modification to the model. The results agree well with the numerical solution as developed by Hill (1975b) and show that after an initial slowdown, the vortices begin to accelerate downwards.

Chapter 4 reproduces completely a paper that has already been published (Baker, Barker, Bofah and Saffman (1974)) on the effect of "vortex wandering" on the measurement of velocity profiles of the trailing vortices behind a wing.

TABLE OF CONTENTS

CHAPTER	TITLE		PAGE
	Acknowledgments		ii
	Abstract		iii
	Table of Contents		v
1	The Structure and Stability of a Hollow Array of Vortices		1
	1.I	Introduction	1
	1.II	Proof of Fore and Aft Symmetry	4
	1.III	Determination of Solutions	10
	1.IV	Stability of Solutions	18
	1.V	A Single Hollow Vortex in a Straining Field	31
	Appendix		36
2	Numerical Studies of the Roll-up of Two-Dimensional Vortex Sheets in Homogeneous Fluid		40
	2.I	Introduction	46
	2.II	The Calculation of the Velocity of a Vortex Sheet	47
	2.III	Redistribution of Vortex Points as a Way to Follow the Motion of a Vortex Sheet	59
	2.IV	Numerical Results for Methods Based on Redistribution of Vortex Points	65
	2.V	A Method Based on the Cloud-in-Cell Technique	88
3	A Study of the Motion of a Buoyant Pair of Line Vortices		119
	3.I	Introduction	119

TABLE OF CONTENTS (cont.)

CHAPTER	TITLE	PAGE
	3.II The Taylor Series in Time	128
	3.III A Macroscopic Model	147
4	Laser Anemometer Measurements of Trailing Vortices in Water	174
	4.1 Introduction	174
	4.2 Experimental Programme	175
	4.3 Theory and Analysis	179
	References	185
References		186

Chapter 1

The Structure and Stability of a Hollow Array of Vortices

I. INTRODUCTION

The work that is presented in this chapter arose mainly from an attempt by Moore and Saffman (1975) to understand the organised vortex structures in a turbulent mixing layer. It has been explicitly pointed out by Winant and Browand (1974) and Brown and Roshko (1974) that these structures are a result of a continual process of vortex amalgamation. Moore and Saffman (1975) noted that the straining fields induced by a regular array of vortices of finite cross-section become large as the spacing between the vortices decreases, and could provide the mechanisms by which vortices disintegrate and amalgamate. In their work, Moore and Saffman (1975) rely heavily on an exact solution for a single vortex, with constant vorticity in its core, in a uniform straining field (Moore and Saffman (1971)), and extrapolate to the case of a regular array of uniform vortices.

This chapter analyses the case of a regular array of hollow or stagnant core vortices in perfect fluid where the vorticity is concentrated on the surface of the vortices. The steady flow field can be found exactly by means of free streamline theory. All the vortices are identical and lie

evenly spaced along a straight line. With the array characterised by the number $A^{1/2}/L$ where A is the area of a vortex and L the distance between vortices, there are two steady solutions for a given $A^{1/2}/L < 0.38$. In the limit $A^{1/2}/L \to 0$, one solution describes an array of circular vortices with their separation distance much greater than their radius, while the other approaches the limit of a vortex sheet. This non-uniqueness makes the stability of the solutions important. It is shown that the more deformed shape is unstable to two-dimensional, periodic, symmetric disturbances which leave the centres undisplaced.

Thus this analysis provides direct verification of the idea that there is a minimum separation distance for an array to exist. Further, the case of a single, hollow or stagnant core vortex in a straining field has been calculated (Hill (1975a)), and so the validity of an extrapolation from the results for a single vortex to predictions for arrays can be explored analytically.

The details of this work are presented in four sections and an appendix. Assuming only reflectional symmetry, it is shown in Section II that there must in fact be fore and aft symmetry and that the vortices must be convex. The two steady solutions are obtained in Section III while their stability to two-dimensional, periodic, symmetrical disturbances is examined in Section IV. Further work is needed to study the more general stability associated with

displaced centres. This would in fact be determining whether the Lamb instability for an array of point vortices disappears if the cores have finite cross-section. Hill's (1975a) work is summarised for completeness in Section V. Also in this section is the discussion pertaining to the relationship between the array and the single vortex in a straining field. The proof that the symmetry assumed by Hill (1975a) is in fact required in order for a steady solution to exist is presented in the appendix at the end of this chapter.

The problem was studied jointly with J. S. Sheffield and the essence of the chapter has been published by Baker, Sheffield and Saffman (1976). The author's particular contribution appears in Section II and a large part of Section IV, especially the determination of the difference equation governing the Fourier coefficients of the infinitesimal disturbances in the stability analysis, and the appendix.

II. PROOF OF FORE AND AFT SYMMETRY

When approaching the problem of determining a solution for the array of hollow vortices, a natural question arises about the symmetry of the flow field. It will be shown in this section that the steady solutions which are symmetric to rotations through π radians about a vortex centre are also symmetric about the y and x axes (see Figure 1.1a for the definition of coordinate system). The vortices are considered to have the centres equally spaced along the x-axis. The flow is steady and so for hollow or stagnant cores, the boundary condition of constant pressure on the vortex surface means that the velocity has a constant magnitude, q_0 , on the vortex surface. The circulation, Γ , of each vortex is related to q_0 by

$$\Gamma = P q_0 \tag{1.1}$$

where P is the perimeter. At large distances the array looks like a vortex sheet of strength $2U_\infty$, where

$$U_\infty = \frac{\Gamma}{2L} \tag{1.2}$$

The array is characterised by a dimensionless ratio

$$R = \frac{U_\infty}{q_0} = \frac{1}{2}\frac{P}{L} \tag{1.3}$$

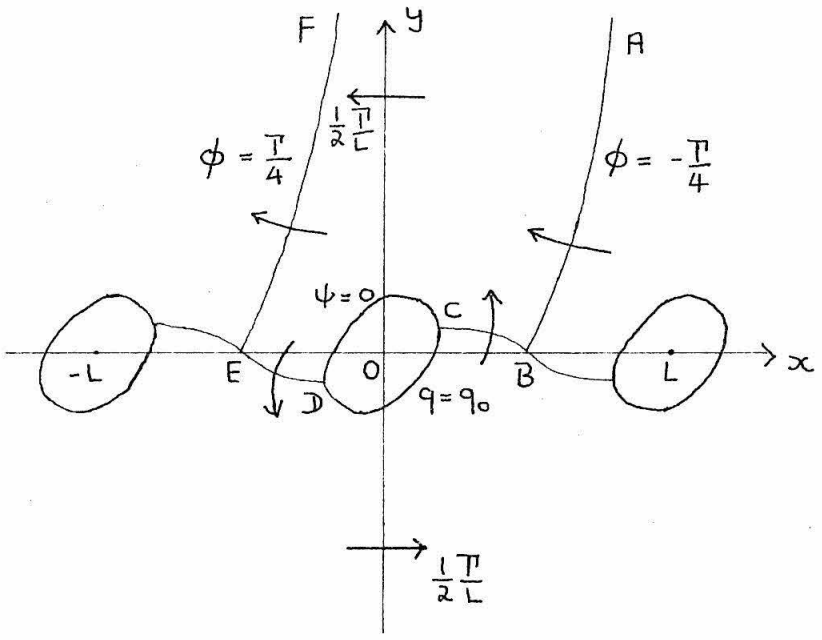

a) **The physical plane,** $z = x + iy$

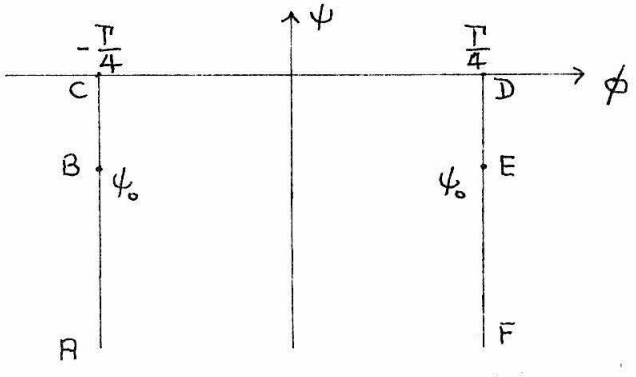

b) **The potential plane,** $w = \phi + i\psi$

Figure 1.1

Introducing the complex variable $z = x+iy$, the complex potential $w = \phi+i\psi$, the complex velocity

$$u - iv = \frac{dw}{dz} = qe^{-i\theta} \tag{1.4}$$

and the hodograph variable

$$\Omega = \log\left(\frac{q_0}{q}\right) + i\theta = \tau + i\theta \tag{1.5}$$

a solution is found in terms of a relationship between Ω and w.

The potential plane is as shown in Figure 1.1b. The boundary of the vortex must be a streamline and is chosen to be $\psi = 0$. There will be constant potential curves of unknown shape passing through the stagnation points B, E. Knowing the direction of the velocity along the potential curves establishes the variation of ψ. However, the periodicty of the array requires the velocity to be the same on corresponding points on EF, BA. Along BC, ED the magnitude of the velocity must be the same at corresponding points.

ϕ, ψ must satisfy Laplace's equation and this is also true for their derivatives. Since the potential and stream function provide a conformal transform of the physical plane, the velocity must satisfy Laplace's equation in the potential plane. In particular

$$\nabla^2 \tau = 0 \tag{1.6}$$

inside ABCDEF, and τ satisfies the following boundary conditions

$$\tau = 0 \quad \text{along CD} \tag{1.7}$$

$$\tau \text{ has period } \frac{\pi}{2} \text{ in } \phi \tag{1.8}$$

$$\tau \sim \log\left(\frac{q_0}{U_\infty}\right) = -\log R \quad \text{as } \psi \to -\infty \tag{1.9}$$

At the stagnation points, B,E , $\frac{dw}{dz} \sim (w-w_0)^{1/2}$ where w_0 is the potential there, i.e. $w_0 = \pm\frac{\pi}{4} + i\psi_0$. Subtracting this singular behaviour from τ , ensures that the remainder is an analytic function in ABCDEF and can be determined by the technique of separation of variables. Thus consider

$$\tau = \mathrm{Re}\left\{ -\log 2R - \tfrac{1}{2}\log\left(\cos\tfrac{2\pi w}{\pi} + i\sinh\tfrac{2\pi\psi_0}{\pi}\right) - \tfrac{1}{2}\log\left(\cos\tfrac{2\pi w}{\pi} - i\sinh\tfrac{2\pi\psi_0}{\pi}\right) + \tfrac{2\pi i}{\pi} w \right\} + H(\phi,\psi) \tag{1.10}$$

where H satisfies Laplace's equation, the conditions (1.7), (1.8) and is bounded on the strip. The above form meets the requirements of the solution since, in the first place, it is symmetric in ϕ with period $\frac{\pi}{2}$, and secondly its

behaviour at the stagnation point, B, is (let $\varepsilon = w - \frac{\pi}{4} - i\psi_0$)

$$\tau \sim \mathrm{Re}\left\{-\tfrac{1}{2}\log\left(\cos\tfrac{2\pi}{\pi}\left(\tfrac{\pi}{4}+i\psi_0+\varepsilon\right)+i\sinh\tfrac{2\pi\psi_0}{\pi}\right)\right\}$$

$$\sim -\tfrac{1}{2}\log\varepsilon \qquad (1.11)$$

Finally as $\psi \to -\infty$,

$$\tau \sim \mathrm{Re}\left\{-\log 2R - \log\left(\cosh\tfrac{2\pi\psi}{\pi}\right) - \tfrac{2\pi\psi}{\pi}\right\}$$

$$\sim -\log R + O\left(e^{4\pi\psi/\pi}\right) \qquad (1.12)$$

and so (1.9) is satisfied.

The solution for H is now straightforward;

$$H(\phi,\psi) = \sum_{n=0}^{\infty} e^{4\pi n\psi/\pi}\left(A_n \sin\tfrac{4\pi n\phi}{\pi} + B_n \cos\tfrac{4\pi n\phi}{\pi}\right) \qquad (1.13)$$

The remaining condition, (1.7), gives

$$-\log 2R - \tfrac{1}{2}\log\left(\cos^2\tfrac{2\pi\phi}{\pi} + \sinh^2\tfrac{2\pi\psi}{\pi}\right) + \sum_{n=0}^{\infty}\left(A_n \sin\tfrac{4\pi n\phi}{\pi}\right.$$

$$\left. + B_n \cos\tfrac{4\pi n\phi}{\pi}\right) = 0 \qquad (1.14)$$

It is immediately obvious that $A_n = 0$, $\forall n$, and the B_n are all uniquely determined. In particular, $B_0 = 0$. This gives

$$\log 2R + \frac{1}{T}\int_{-T/4}^{T/4} \log\left(\cos^2\frac{2\pi\phi}{T} + \sinh^2\frac{2\pi\psi_0}{T}\right) d\phi = 0 \qquad (1.15)$$

Substituting $\theta = \frac{4\pi\phi}{T}$ and defining $b = 1 + 2\sinh^2\frac{2\pi\psi_0}{T}$, (1.15) becomes

$$\log 2R - \frac{1}{2}\log 2 + \frac{1}{4\pi}\int_{-\pi}^{\pi} \log\left(b + \cos\theta\right) d\theta = 0 \qquad (1.16)$$

or

$$\log 2R - \frac{1}{2}\log 2 + \frac{1}{2}\log\left[\frac{b + (b^2-1)^{1/2}}{2}\right] = 0 \qquad (1.17)$$

Finally,

$$R^2\left[b + (b^2-1)^{1/2}\right] = 1 \qquad (1.18)$$

Since $b \geq 1$, this implies $R \leq 1$. Since $A_n = 0, \forall n$, the streamlines must be even in ϕ, i.e. symmetry about the y-axis. Symmetry about the x-axis follows from reflectional symmetry. Although the solution is now known it is in a form (fourier series) which is difficult to analyse. The next section provides a solution in a more understandable form.

III. DETERMINATION OF SOLUTIONS

Using the established symmetry, one is now able to draw the physical plane as in Figure 1.2a. Using the definitions $w = \phi + i\psi$ and (1.4-5) as before, the potential and hodograph planes can be drawn as shown in Figures 1.2b and c. θ is defined by $\theta = \arctan \frac{v}{u}$ and $-\pi \leq \theta \leq \pi$. It is not immediately obvious that the curvature of the boundary at D should be convex but recall that $R \leq 1$ means $u_\infty \leq q_0$ and that u cannot have a maximum along DE except at D or E (as a result of the well-known maximum modulus theorems for analytic functions). Thus $\tau > 0$.

The Schwarz-Christoffel transformation

$$w = \frac{i\Gamma}{2\pi} \log\left[(\zeta+1)^{1/2} - (\zeta-1)^{1/2}\right] - \frac{i\Gamma}{4\pi} \log 2 \qquad (1.19)$$

maps the interior ABCDE of the potential plane onto the upper half plane of the $\zeta = \xi + i\eta$ plane. The definition, $z^{1/2} = |z|^{1/2} e^{i\theta/2}$, $-\pi < \theta < \pi$, is the branch used throughout this section and the principal branch is used for the log function. It is easy to show (1.19) is the mapping required by considering $\zeta = \xi > 1$, then $(\xi+1)^{1/2}$, $(\xi-1)^{1/2}$ are both real and w is purely imaginary. At $\xi = 1$, $\psi = 0$ and, since

$$\frac{dw}{d\zeta} = -\frac{i\Gamma}{4\pi} (\zeta+1)^{-1/2} (\zeta-1)^{-1/2}, \qquad (1.20)$$

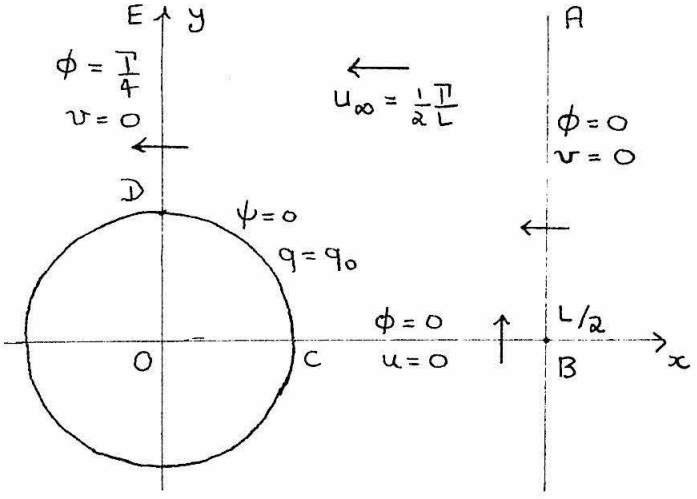

a) **The physical plane,**

$z = x + iy$

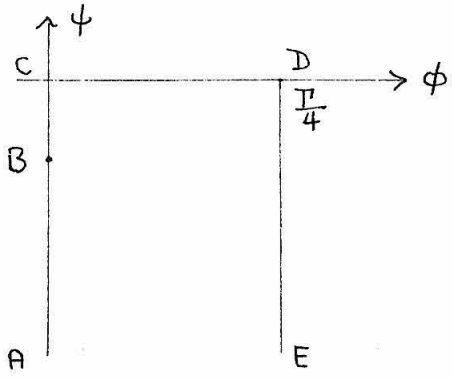

b) **The potential plane,**

$w = \phi + i\psi$

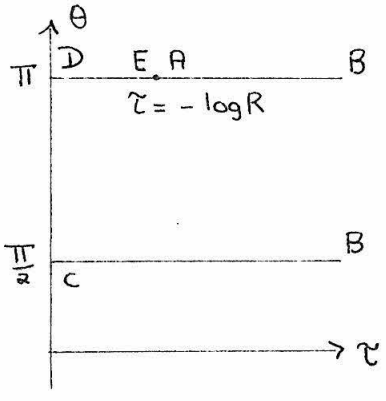

c) **The hodograph plane,**

$\Omega = \tau + i\theta$

Figure 1.2

then $\frac{\partial\psi}{\partial\xi} < 0$. This means CA is mapped onto $\eta = \xi$, $\xi \geq 1$ with C at $\xi = 1$, A at $\xi = \infty$. The point B will lie along this line, at $\xi = b$ say.

For $-1 \leq \xi \leq 1$, (1.19) gives $\omega = -\frac{T}{2\pi}\theta$, where $\tan\theta = -(1-\xi)^{1/2}/(1+\xi)^{1/2}$ and $-\frac{\pi}{2} < \theta < 0$. Thus the line CD is mapped onto $-1 \leq \xi \leq 1$ with D at $\xi = -1$.

For $\xi \leq -1$, (1.19) becomes $\omega = \frac{T}{4} + \frac{iT}{2\pi}\log\left[(1-\xi)^{1/2} - (-\xi-1)^{1/2}\right] - \frac{iT}{4\pi}\log 2$. At $\xi = -1$, $\omega = \frac{T}{4}$ as required and since $\frac{\partial\psi}{\partial\xi} > 0$ as $\xi \to -\infty$, $\psi \to -\infty$. Thus DE is mapped onto $\xi \leq -1$. The fact that the interior goes into the upper half plane is an obvious result of having evaluated the multivalued function with a small positive imaginary part for η when necessary.

Now Ω can be mapped onto the same region of the plane by the following transformation,

$$\Omega = -\log\left[\{(b-1)(\eta+1)\}^{1/2} - \{(b+1)(\eta-1)\}^{1/2}\right] + \frac{1}{2}\log(\eta-b) + \frac{1}{2}\log 2 \qquad (1.21)$$

$$\frac{d\Omega}{d\eta} = -\frac{1}{2}\frac{(b+1)^{1/2}(b-1)^{1/2}}{(\eta-b)(\eta+1)^{1/2}(\eta-1)^{1/2}} \qquad (1.22)$$

This mapping is checked by considering $\eta = \xi > b$, then the square roots are real but $(b-1)^{1/2}(\xi+1)^{1/2} < (b+1)^{1/2}(\xi-1)^{1/2}$ and the argument of the log function must be evaluated correctly i.e. by giving a small positive imaginary component to η ,

then $(b-1)^{1/2}(\xi+1)^{1/2}e^{i\theta_-/2} - (b+1)^{1/2}(\xi-1)^{1/2}e^{i\theta_+/2}$ has a small negative imaginary part, where $\zeta+1 = |\zeta+1|e^{i\theta_-}$ and $\zeta-1 = |\zeta-1|e^{i\theta_+}$.

$$\Omega = i\pi - \log\left[(b+1)^{1/2}(\xi-1)^{1/2} - (b-1)^{1/2}(\xi+1)^{1/2}\right]$$

$$+ \tfrac{1}{2}\log(\xi-b) + \tfrac{1}{2}\log 2 \qquad (1.23)$$

As $\xi \to \infty$, (1.23) becomes

$$\Omega = i\pi - \log\left[(b+1)^{1/2} - (b-1)^{1/2}\right] + \tfrac{1}{2}\log 2 \qquad (1.24)$$

This limit corresponds to the point A in the ζ plane and so for Ω to have the correct value at A, one requires

$$-\log R = -\log\left[(b+1)^{1/2} - (b-1)^{1/2}\right] + \tfrac{1}{2}\log 2 \qquad (1.25)$$

or after some trivial algebra,

$$b - (b^2-1)^{1/2} = R^2, \quad b = (1+R^4)/2R^2 \qquad (1.26)$$

This equation is essentially relating the position of the stagnant point to R. From (1.22) one obtains for $\zeta = \xi > b$, $\frac{\partial \tau}{\partial \xi} < 0$ so that as ξ decreases from ∞ at A, τ increases and reaches ∞ at B.

For the case where $\zeta = \xi$, $1 < \xi < b$, one finds

$(b-1)^{1/2}(\xi+1)^{1/2} > (b+1)^{1/2}(\xi-1)^{1/2}$ and thus

$$\Omega = -\log\left[(b-1)^{1/2}(\xi+1)^{1/2} - (b+1)^{1/2}(\xi-1)^{1/2}\right]$$

$$+ \tfrac{1}{2}\log(b-\xi) + \tfrac{1}{2}\log a \qquad (1.27)$$

The point C , as determined by $\xi \to 1^+$, is mapped to $\Omega = i\frac{\pi}{2}$ as required. Now $\frac{\partial \tau}{\partial \xi} > 0$ and so as $\xi \to b^-$, τ increases to ∞ .

The case $-1 < \xi < 1$ gives $\Omega = i\frac{\pi}{2} - i\theta$ where $\tan\theta = -(b+1)^{1/2}(1-\xi)^{1/2}/(b-1)^{1/2}(1+\xi)^{1/2}$ and θ goes from 0 to $-\frac{\pi}{2}$ as ξ goes from -1 to 1. Thus CD is mapped as required.

For $\xi < -1$, the expression $i(b-1)^{1/2}(-\xi-1)^{1/2} - i(b+1)^{1/2}(1-\xi)^{1/2}$ is a negative imaginary number and so

$$\Omega = i\pi - \log\left[(b+1)^{1/2}(1-\xi)^{1/2} - (b-1)^{1/2}(-\xi-1)^{1/2}\right]$$

$$+ \tfrac{1}{2}\log(b-\xi) + \tfrac{1}{2}\log a \qquad (1.28)$$

Clearly as $\xi \to -1^-$, $\Omega \to i\pi$ and as $\xi \to -\infty$, $\Omega \to -\log R$ by (1.25), and so the mapping achieves the required result.

There is thus a relationship between w and Ω through the common ζ plane. From (1.4) and (1.5),

$$\Omega = \log\left(q_0 / \frac{dw}{dz}\right) \; ; \quad \frac{dw}{dz} = q_0 e^{-\Omega} \qquad (1.29)$$

The physical plane follows from integrating

$$\frac{dz}{d\zeta} = \frac{dz}{dw}\frac{dw}{d\zeta} = \frac{e^{i\alpha}}{q_0}\frac{dw}{d\zeta} \tag{1.30}$$

Substituting (1.20) and (1.21) into (1.30) leads directly to

$$\frac{dz}{d\zeta} = -\frac{iRL}{2^{1/2}\pi}\frac{(\zeta-b)^{1/2}}{(\zeta-1)^{1/2}(\zeta+1)^{1/2}}\left[(b-1)^{1/2}(\zeta+1)^{1/2} - (b+1)^{1/2}(\zeta-1)^{1/2}\right] \tag{1.31}$$

However, it is the shape of the vortex that is most interesting and so consider $\zeta = \xi$, $-1 \le \xi \le 1$, then

$$\frac{dz}{d\xi} = -\frac{iRL}{2^{3/2}\pi}\frac{(b-1)^{1/2}(1+\xi)^{1/2} + i(b+1)^{1/2}(1-\xi)^{1/2}}{(b-\xi)^{1/2}(1-\xi)^{1/2}(1+\xi)^{1/2}} \tag{1.32}$$

or equivalently with $Z(\xi) = X(\xi) + iY(\xi)$,

$$\frac{dX}{d\xi} = \frac{RL}{2^{3/2}\pi}\frac{(b+1)^{1/2}}{(b-\xi)^{1/2}(1+\xi)^{1/2}} \; ; \; \frac{dY}{d\xi} = -\frac{RL}{2^{3/2}\pi}\frac{(b-1)^{1/2}}{(b-\xi)^{1/2}(1-\xi)^{1/2}} \tag{1.33}$$

The transformation, $\xi = -\cos 2\lambda$, allows direct integration. With $X = 0$ at $\lambda = 0$, $Y = 0$ at $\lambda = \frac{\pi}{2}$, corresponding to the centre of the vortex being chosen at the origin,

$$X = \frac{L}{2\pi}(1+R^2)\sin^{-1}\left(\frac{2R\sin\lambda}{1+R^2}\right) \; ; \; Y = \frac{L}{2\pi}(1-R^2)\sinh^{-1}\left(\frac{2R\cos\lambda}{1-R^2}\right) \tag{1.34}$$

where $0 \le \lambda \le 2\pi$ describes the complete perimeter. As

$R \to 0$,

$$X \to \frac{LR}{\pi} \sin\lambda \quad ; \quad Y \to \frac{LR}{\pi} \cos\lambda \tag{1.35}$$

which is a parametric representation for a circle. As $R \to 1$,

$$X \to \frac{L\lambda}{\pi} \quad ; \quad Y \to 0 \tag{1.36}$$

and the shape has the appearance of a slit. From (1.18), one knows $0 \leq R \leq 1$ and so the two cases are limiting forms.

The perimeter P is $2RL$ and is a measure of the deformation of the shape. The area has to be found numerically. The results are shown as a curve, $P/A^{1/2}$ versus $A^{1/2}/L$ in Figure 1.3. From this curve it is seen that for a given $A^{1/2}/L$ there are two or no solutions depending on whether $A^{1/2}/L$ is less than or greater than 0.38 respectively. An interesting problem presents itself in determining what happens to the array when $A^{1/2}/L > 0.38$. The stability of these solutions is important and is considered in detail in the next section.

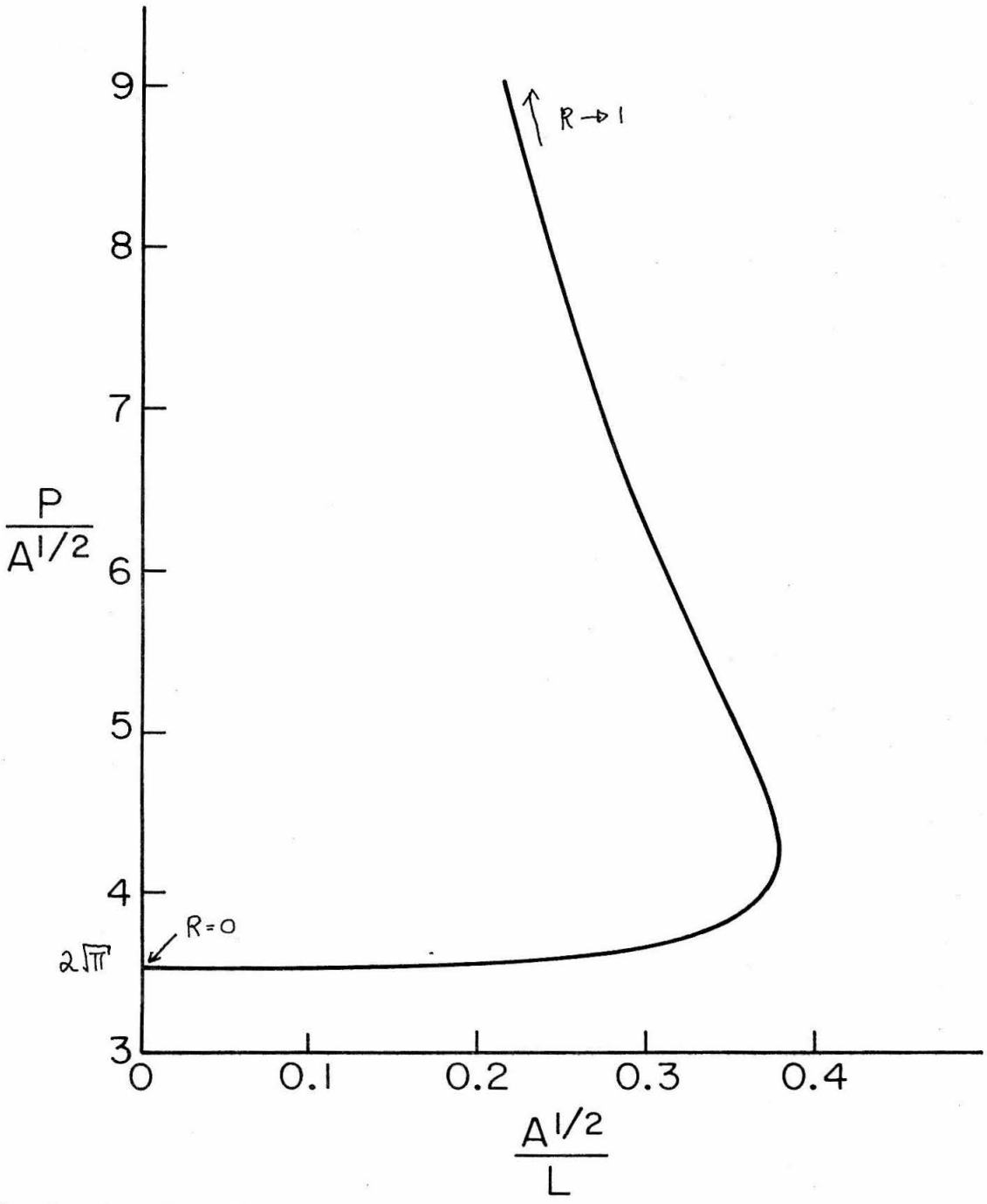

Perimeter length as a function of the inverse of the separation distance.

Figure 1.3

IV. STABILITY OF THE SOLUTIONS

The prime purpose of this section is to examine the stability of the hollow vortex to infinitesimal disturbances of its boundary which have reflectional symmetry. Displacements of the vortex centres which could result in an instability of the array of the type considered by Lamb (1932, § 156) for point values are not considered and is left as a subject for further study. To this end, one needs to consider only the region as shown in Figure 1.1a.

Only the hollow core vortex is being considered for the sake of simplicity, since the requirement of constant pressure at the vortex surfaces enables a simple treatment of the dynamic boundary condition. The stagnant core vortex would have to be considered separately, because of core motion, and is not studied here.

The easiest plane in which to do the analysis is the undisturbed potential plane (ϕ, ψ). If one defines the total potential as $\phi + \Phi$, then

$$\frac{\partial^2 \Phi}{\partial \phi^2} + \frac{\partial^2 \Phi}{\partial \psi^2} = 0 \qquad (1.37)$$

and

$$\Phi \to 0 \text{ , as } \psi \to -\infty \qquad (1.38)$$

The perturbed surface is defined by $\psi = \delta(\phi,t)$.

Before treating the kinematic and dynamic boundary conditions, one needs to know the scale factors for the curvilinear coordinate system (ϕ,ψ). Since

$$\frac{dz}{dw} = \frac{u+iv}{q^2} \quad , \quad q^2 = u^2 + v^2 \, , \tag{1.39}$$

$$\therefore \quad (dx)^2 + (dy)^2 = \frac{1}{q^2}(d\phi)^2 + \frac{1}{q^2}(d\psi)^2 \tag{1.40}$$

and q is a function of ϕ,ψ as determined by the unperturbed solution.

The kinematic condition, with $\vec{u}$ having components (u,v) in the potential plane, is

$$\left(\frac{\partial}{\partial t} + \vec{u}\cdot\nabla\right)\left(\psi - \delta(\phi,t)\right) = 0 \quad \text{at } \psi = \delta \tag{1.41}$$

This becomes (see Morse and Feshback (1953, Section 1.3) for a treatment of curvilinear coordinates)

$$-\frac{\partial\delta}{\partial t} - qu\frac{\partial\delta}{\partial\phi} + qv = 0 \quad \text{at } \psi = \delta \tag{1.42}$$

(1.42) can be linearised for infinitesimal disturbances by writing

$$u = \bar{u} + q\frac{\partial\Phi}{\partial\phi} \quad , \quad v = \bar{v} + q\frac{\partial\Phi}{\partial\psi} \tag{1.43}$$

where the overbar refers to undisturbed velocity components in the potential plane. To first order in perturbed quantities, (1.42) becomes

$$\frac{\partial \delta}{\partial t} + q_0^2 \frac{\partial \delta}{\partial \phi} = q_0^2 \frac{\partial \Phi}{\partial \psi} + q_0 \frac{\partial \bar{v}}{\partial \psi} \delta \quad \text{at } \psi = 0 \qquad (1.44)$$

The equation of continuity,

$$\nabla \cdot \vec{u} = q^2 \left[\frac{\partial}{\partial \phi}\left(\frac{u}{q}\right) + \frac{\partial}{\partial \psi}\left(\frac{v}{q}\right) \right] = 0 \qquad (1.45)$$

evaluated at $\psi = 0$ to lowest order,

$$\frac{1}{q_0} \frac{\partial \bar{u}}{\partial \phi} + \frac{1}{q_0} \frac{\partial \bar{v}}{\partial \psi} - \frac{\bar{v}}{q_0^2} \frac{\partial q}{\partial \psi} = 0 \qquad (1.46)$$

determines $\frac{\partial \bar{v}}{\partial \psi}$. Of course, $\bar{u} = q_0$, a constant, and $\bar{v} = 0$ and so (1.46) is

$$\frac{\partial \bar{v}}{\partial \psi} = 0 \qquad (1.47)$$

Thus (1.44) becomes

$$\frac{\partial \delta}{\partial t} + q_0^2 \frac{\partial \delta}{\partial \phi} = q_0^2 \frac{\partial \Phi}{\partial \psi} \qquad (1.48)$$

The dynamic condition is handled similarly. Choosing the pressure to be $P = 0$ inside the core gives

$$\frac{1}{2}(u^2+v^2) + \frac{\partial \Phi}{\partial t} = 0 \qquad \text{at } \psi = \delta \tag{1.49}$$

Expanding to include only first terms in perturbed quantities,

$$\bar{u}\frac{\partial \bar{u}}{\partial \psi}\delta + q\bar{u}\frac{\partial \Phi}{\partial \phi} + \frac{\partial \Phi}{\partial t} = 0 \qquad \text{at } \psi = 0 \tag{1.50}$$

Considering $\nabla \times \bar{u} = 0$ at $\psi = 0$, determines $\frac{\partial \bar{u}}{\partial \psi}$. To lowest order,

$$\frac{\partial}{\partial \psi}\left(\frac{\bar{u}}{q}\right) = \frac{\partial}{\partial \phi}\left(\frac{\bar{v}}{q}\right) = 0 \tag{1.51}$$

or

$$\frac{1}{q_0}\frac{\partial \bar{u}}{\partial \psi} = \frac{1}{q_0}\frac{\partial q}{\partial \psi} \tag{1.52}$$

From the exact solution as found in the previous section ((1.20), (1.22))

$$\frac{d\Omega}{dw} = -\frac{\partial \Theta}{\partial \psi} + i\frac{\partial}{\partial \psi}\log\left(\frac{q}{q_0}\right) \tag{1.53}$$

$$= \frac{d\Omega}{d\zeta}\frac{d\zeta}{dw}$$

$$= -i\frac{2\pi}{\Gamma}\frac{(b^2-1)^{1/2}}{(\zeta - b)} \tag{1.54}$$

Therefore at the boundary, $\zeta = \xi$, $-1 \le \xi \le 1$, and

$$\frac{1}{q_0}\frac{\partial q}{\partial \psi} = \frac{2\pi}{\Gamma}\frac{(b^2-1)^{1/2}}{(b-\xi)} \tag{1.55}$$

From (1.19), $\phi = \frac{\Gamma}{2\pi}\arctan\left[(1-\xi)^{1/2}/(1+\xi)^{1/2}\right]$, or $\xi = \cos\frac{4\pi\phi}{\Gamma}$ along $\psi = 0$. Thus (1.50) becomes

$$\frac{\partial \bar{\Phi}}{\partial t} + q_0^2\frac{\partial \bar{\Phi}}{\partial \phi} = -\frac{2\pi q_0^2}{\Gamma}\frac{(b^2-1)^{1/2}\,\delta}{b-\cos(4\pi\phi/\Gamma)} \quad \text{at } \psi = 0 \tag{1.56}$$

The equation (1.37) and the conditions (1.38), (1.48) and (1.56) form the system to be solved, but before doing this some other conditions can be checked. Mass conservation requires to first order

$$\int_0^{\Gamma/2} \delta\, d\phi = 0. \tag{1.57}$$

The circulation Γ remains constant. Since

$$\Gamma = 2\int_0^{\Gamma/2}\left(u + v\frac{\partial \delta}{\partial \phi}q\right)\frac{d\phi}{q}\,, \tag{1.58}$$

expanding to first order gives

$$\int_0^{\Gamma/2}\frac{\partial}{\partial \psi}\left(\frac{\bar{u}}{q}\right)d\phi = 0 \qquad \text{at } \psi = 0. \tag{1.59}$$

This is satisfied after recalling (1.51).

To proceed with the analysis, $\bar{\Phi}$ and δ are expressed in Fourier series

$$\Phi = \sum_{n=-\infty}^{\infty} \Phi_n e^{k|n|\psi} \sin(nk\phi + \omega t) \qquad (1.60)$$

and

$$\frac{\delta}{b - \cos k\phi} = \sum_{n=-\infty}^{\infty} a_n \cos(nk\phi + \omega t) \qquad (1.61)$$

where $k = \frac{4\pi}{\Gamma}$. The representation of δ , (1.61), satisfies (1.57). Now (1.37), (1.38) are satisfied and so (1.60) and (1.61) are substituted into (1.48) and (1.56) and after some algebra, one obtains

$$a_{n+1} + \left\{ \frac{|n| \sinh\beta}{(\sigma + n)^2} - 2\cosh\beta \right\} a_n + a_{n-1} = 0 \qquad (1.62)$$

for $-\infty < n < \infty$. The parameter σ is related to the frequency ω by $\sigma = \frac{\omega\Gamma}{4\pi q_0^2}$, where $b = \cosh\beta$, $\beta = -\log R^2$. This difference equation proves too difficult to solve exactly and a numerical approach is adopted to solve it. Since $a_n \to 0$ as $n \to \pm\infty$, there will be only certain values for σ for which a solution is possible. If any of these values for σ are complex, the motion is unstable.

There are limiting cases where the solution can be determined exactly. As $R \to 0$, or $\beta, b \to \infty$, the undisturbed array becomes a single hollow vortex which will be circular. This limiting case has a known stability, i.e.

$$\sigma = -n \pm \left(\frac{|n|}{2}\right)^{1/2} \tag{1.63}$$

It is possible to find a perturbation solution for large b. Equation (1.62) becomes

$$(a_{n+1} + a_{n-1})\frac{1}{b}\left(1 + \frac{1}{2b^2} + \cdots\right) + \left\{\frac{|n|}{(\sigma+n)^2} - 2\left(1 + \frac{1}{2b^2} + \cdots\right)\right\} a_n = 0 \tag{1.64}$$

The following asymptotic forms will be assumed,

$$a_N = A_N + \frac{a_N^1}{b} + \frac{a_N^2}{b^2} + \cdots \tag{1.65}$$

$$a_n = \frac{a_n^1}{b} + \frac{a_n^2}{b^2} + \cdots \quad \text{for } n \neq N \tag{1.66}$$

$$\sigma = \sigma_0 + \frac{\sigma_1}{b} + \frac{\sigma_2}{b^2} + \cdots \tag{1.67}$$

The perturbation is around the n = N mode for the circular hollow vortex, thus $\sigma_0 = -N \pm (|N|/2)^{1/2}$ as in (1.63). The first order terms in (1.64) give

$$A_N + \left(\frac{|N-1|}{(\sigma_0 + N-1)^2} - 2\right) a_{N-1}^1 = 0 \quad \text{for } n = N-1 \tag{1.68}$$

$$\left(\frac{|N|}{(\sigma_0+N)^2} - 2\right) a'_N - \frac{2\sigma_1 |N|}{(\sigma_0+N)^3} A_N = 0 \quad \text{for } n = N \qquad (1.69)$$

$$A_N + \left(\frac{|N+1|}{(\sigma_0+N+1)^2} - 2\right) a'_{N+1} = 0 \quad \text{for } n = N+1 \qquad (1.70)$$

This analysis requires $N \neq 0$, i.e. $\sigma = 0$ will be considered separately. From (1.69) one must have $\sigma_1 = 0$ and as usual the next order determines σ_2. For all other n, $a'_n = 0$.

The next order becomes

$$\left(\frac{|N|}{(\sigma_0+N)^2} - 2\right) a^2_N - \frac{2\sigma_2 |N|}{(\sigma_0+N)^3} A_N - 2A_N + a'_{N+1} + a'_{N-1} = 0 \quad \text{for } n = N \qquad (1.71)$$

Substituting (1.68), (1.70) into (1.71) gives

$$\frac{2|N|\sigma_2}{(\sigma_0+N)^3} = -2 - \frac{(\sigma_0+N+1)^2}{|N+1| - 2(\sigma_0+N+1)^2} - \frac{(\sigma_0+N-1)^2}{|N-1| - 2(\sigma_0+N-1)^2} \qquad (1.72)$$

So provided the asymptotic expansion is valid, a solution has been found for large b, i.e. small R, which shows stable solutions.

The other important limit, $\sigma = 0$, establishes the possibility of unstable solutions for certain β or R. The equation (1.62) becomes for $n > 0$

$$a_{n+1} + \left[\frac{\sinh\beta}{n} - 2\cosh\beta \right] a_n + a_{n-1} = 0 \qquad (1.73)$$

For large n, this has the general solution (as will be shown later, (1.80))

$$a_n \sim C_0 n^{1/2} e^{-\beta n} + C_1 \frac{e^{\beta n}}{n^{1/2}} \qquad (1.74)$$

The generating function, $G(z) = \sum_{n=0}^{\infty} a_n z^n$ satisfies

$$z(1 - 2\cosh\beta.z + z^2)\frac{dG}{dz} + (z^2 + \sinh\beta.z - 1)G$$

$$= -a_0 + a_0 \sinh\beta.z \qquad (1.75)$$

This has solution

$$G(z) = \frac{a_0 e^{\beta}}{(e^{\beta} - z)} + \frac{2a_0 \sinh\beta.z}{(e^{\beta} - z)^{3/2}(e^{-\beta} - z)^{1/2}} \log\left\{ (e^{\beta} - z)^{1/2} + (e^{-\beta} - z)^{1/2} \right\} + \frac{Cz}{(e^{\beta} - z)^{3/2}(e^{-\beta} - z)^{1/2}} \qquad (1.76)$$

where C is a constant to be determined. For large n, $G(z)$ has terms like $C_0 n^{1/2} e^{-\beta n} z^n + C_1 \frac{e^{\beta n}}{n^{1/2}} z^n$. So requiring $G(z)$ to be analytic at $z = e^{-\beta}$ ensures that $C_1 = 0$, i.e. there is no divergent component to the series. Thus, $C = -a_0 \sinh\beta. \log(e^{\beta} - e^{-\beta})$, and by expanding (1.76),

$$\frac{a_1}{a_0} = e^{-\beta}\left[1 + \sinh\beta . \log\left\{\frac{\cosh\beta+1}{\sinh\beta}\right\}\right] \qquad (1.77)$$

Since for $\sigma = 0$, the difference equation (1.62) is even in n, one has

$$\frac{a_1}{a_0} = \frac{a_{-1}}{a_0} \qquad (1.78)$$

and from the equation (1.62) for $n = 0$,

$$\frac{a_1}{a_0} = \cosh\beta = e^{-\beta}\left[1 + \sinh\beta . \log\left\{\frac{\cosh\beta+1}{\sinh\beta}\right\}\right] \qquad (1.79)$$

This has a solution $\beta = 0.434$ and the numerical method to be described shows this to be the transition point between stable and unstable solutions.

In order to solve (1.62) numerically it is convenient to follow the method of Laplace (Jeffreys and Jeffreys, 1950, p. 486). The idea is to obtain for a fixed β a solution for $\frac{a_1}{a_0}$ and $\frac{a_{-1}}{a_0}$ for which $a_n \to 0$ as $n \to \infty$ and $a_{-n} \to 0$ as $n \to -\infty$ respectively. These two quantities are functions of σ and matching them through the difference equation for $n = 0$ allows σ to be determined. The key to this method is knowing the asymptotic solution. The form of the equation suggests trying, for $n > 0$

$$a_n = e^{-\beta n}(n+1)^{\nu}\phi_n$$

and

$$\phi_n = 1 + \frac{c_1}{n} + \frac{c_2}{n^2} + \cdots \tag{1.80}$$

Substituting into (1.62) and equating coefficients of $\frac{1}{n}$, determines ν, c_1, c_2 etc.

$$\nu = \frac{1}{2} \tag{1.81}$$

$$c_1 = \sigma - \frac{3e^{\beta} - 5e^{-\beta}}{8(e^{\beta} - e^{-\beta})} \tag{1.82}$$

Writing (1.62) in terms of ϕ_n gives

$$e^{-\beta}\phi_{n+1} + \left[\frac{n\sinh\beta}{(n+\sigma)^2} - 2\cosh\beta\right]\left(\frac{n+1}{n+2}\right)^{1/2}\phi_n + e^{\beta}\left(\frac{n}{n+2}\right)^{1/2}\phi_{n-1} = 0 \tag{1.83}$$

The change in variable

$$1 + \psi_n = \frac{\phi_{n+1}}{\phi_n} \tag{1.84}$$

leads to

$$\psi_{n-1} = -1 - \frac{e^{\beta}\left(\frac{n}{n+2}\right)^{1/2}}{\left[\frac{n\sinh\beta}{(n+\sigma)^2} - 2\cosh\beta\right]\left[\frac{(n+1)}{(n+2)}\right]^{1/2} + e^{-\beta}(1+\psi_n)} \tag{1.85}$$

The form of the asymptotics shows

$$\psi_n \sim -\frac{c_1}{n^2} + \frac{c_1 - 2c_2 + c_1^2}{n^3} + O\left(\frac{1}{n^4}\right) \qquad (1.86)$$

The numerical procedure is as follows. For fixed β, N is taken large enough so that (1.86) is a good approximation, then (1.85) is used successively until ψ_0 is determined. In this way, $\psi_0^+ = \psi_0^+(\beta,\sigma)$, where the plus superscript refers to $n > 0$.

For $n < 0$, if one lets $a_{-n} \to a_n$, $-n \to n$ then one obtains the identical difference equation (1.62) with $\sigma \to -\sigma$. Thus one can consider (1.86) with $\sigma = -\sigma$ (now $\psi_n = \psi_n^- = \left(\frac{n+1}{n+2}\right)^{1/2} \frac{a_{-n-1}}{a_{-n}} e^{\beta} - 1$) and $\psi_0^-(\beta,\sigma) = \frac{e^{\beta}}{\sqrt{2}} \frac{a_{-1}}{a_0} - 1$. There is the obvious symmetry relation,

$$\psi_0^-(\beta,\sigma) = \psi_0^+(\beta,-\sigma) \qquad (1.87)$$

σ is finally determined by the relation obtained from the difference equation (1.62) for $n = 0$.

i.e. $$\frac{a_1}{a_0} + \frac{a_{-1}}{a_0} = 2\cosh\beta$$

or

$$\psi_0^+ + \psi_0^- = \sqrt{2}\, e^{\beta} \cosh\beta - 2 \qquad (1.88)$$

Using (1.87), it is clear that the roots occur in pairs, $\pm\sigma$. Starting with large β where the asymptotic roots are known, the roots can be followed as β decreases. The smallest positive root σ_1, turns out to be the one of interest. σ_1 is real from $\beta=\infty$, where $\sigma_1 = 1 - 1/\sqrt{2}$, to $\sigma_1 = 0$ at $\beta = 0.434$ (corresponding to the analytic solution obtained for $\sigma=0$, see (1.79)). For $\beta < 0.434$, roots can be found numerically which are complex establishing a transition to instability. The other roots remain real. The value for β which gives the onset of instability corresponds to $R = 0.805$ and occurs at the maximum $A^{1/2}/L$ as shown in Figure 1.3. Unfortunately, it proves too difficult to establish this fact analytically. Thus it has been shown that for $R > 0.805$, corresponding to the upper curve in Figure 1.3, the more deformed solution is unstable. There is an interesting parallel with the case of a uniform elliptic vortex core (Moore and Saffman (1971)). The next section discusses the relevance of this work.

V. A SINGLE HOLLOW VORTEX IN A STRAINING FIELD

For the sake of completeness, a brief summary of Hill's (1975a) work for the single hollow vortex in a straining field is included. Figures 1.4 a,b,c and d give diagrams of the physical plane and the mapped planes. Once again it can be shown (see the Appendix) that the steady solutions have symmetry about the x and y axes. The usual notation is used, $z = x + iy$, $w = \phi + i\psi$, $\frac{dw}{dz} = u - iv$ and $\Omega = \tau + i\Theta = \log\left(\frac{dw}{dz}/q_0\right)$. The shape of the vortex may be convex or concave at the point B and this manifests itself in the Ω plane where B' lies on the τ-axis for a convex shape and on the Θ-axis for a concave shape.

The following Schwarz-Christoffel transformations take w, Ω to the ζ plane. Γ is the circulation concentrated on the boundary.

$$w = \frac{-i\Gamma}{4\pi}\log\left[2\zeta + 1 + 2\zeta^{1/2}(\zeta+1)^{1/2}\right] - \frac{i\Gamma}{2\pi}\frac{\zeta^{1/2}(\zeta+1)^{1/2}}{2\beta-1} \qquad (1.89)$$

$$\Omega = \frac{1}{2}\log\left[2\zeta + 1 + 2\zeta^{1/2}(\zeta+1)^{1/2}\right] - 2\log\left[\beta^{1/2}(\zeta+1)^{1/2} + \zeta^{1/2}(\beta-1)^{1/2}\right] + \log(\zeta+\beta) - \frac{i\pi}{2} \qquad (1.90)$$

or

$$\frac{1}{q_0}\frac{dw}{dz} = \frac{-i(\zeta+\beta)\left[2\zeta + 1 + 2\zeta^{1/2}(\zeta+1)^{1/2}\right]}{\left[\beta^{1/2}(\zeta+1)^{1/2} + \zeta^{1/2}(\beta-1)^{1/2}\right]} \qquad (1.91)$$

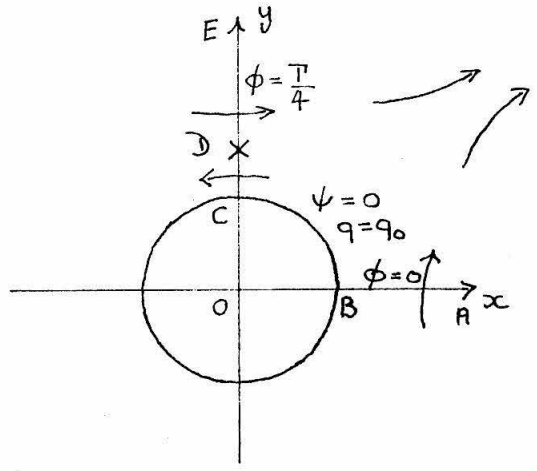

a) **The physical plane,** $z = x + iy$

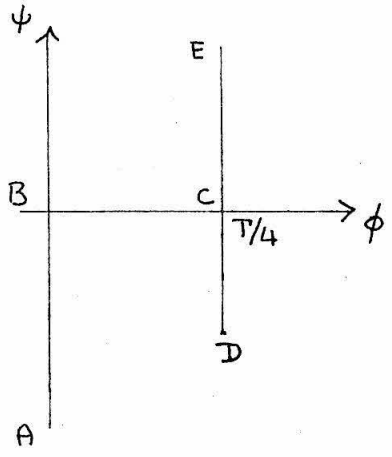

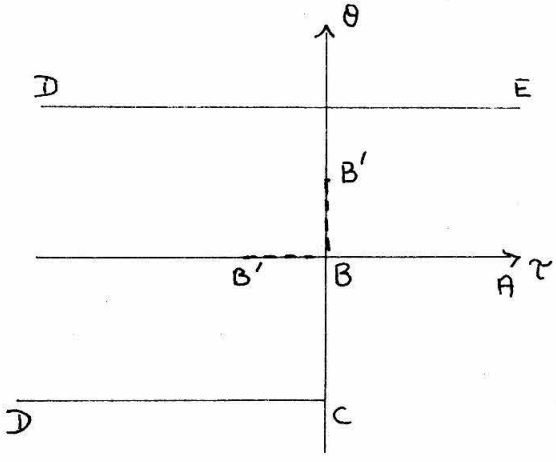

b) **The potential plane,** $w = \phi + i\psi$

c) **The hodograph plane,** $\Omega = \tau + i\theta$

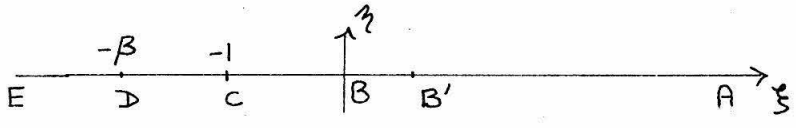

d) **The** ζ **plane,** $\zeta = \xi + i\eta$

Figure 1.4

β is determined by the requirement that far from the vortex the flow is a straining field and hence

$$\frac{dw}{dz} \sim -i\varepsilon\left(\frac{2iw}{\varepsilon}\right)^{1/2} \tag{1.92}$$

where ε is the rate of strain. This leads to

$$\frac{4\pi(2\beta-1)}{\left[\beta^{1/2}+(\beta-1)^{1/2}\right]^4} = E \equiv \frac{\varepsilon P^2}{\Gamma} \tag{1.93}$$

where P is the perimeter. The shape is found by integrating

$$\frac{dz}{d\zeta} = \frac{dz}{dw}\frac{dw}{d\zeta} = \frac{P}{2\pi}\frac{1}{(2\beta-1)}\frac{\left[\beta^{1/2}(\zeta+1)^{1/2}+\zeta^{1/2}(\beta-1)^{1/2}\right]^2}{\left[\zeta^{1/2}+(\zeta+1)^{1/2}\right]\zeta^{1/2}(\zeta+1)^{1/2}} \tag{1.94}$$

and leads to a parametric solution, $0 \le t \le 1$,

$$X = \frac{P}{2\pi}\frac{1}{(2\beta-1)}\left[-\frac{2}{3}\left\{\beta-2\beta^{1/2}(\beta-1)^{1/2}\right\}(1-t)^{3/2}+2(\beta-1)t(1-t)^{1/2}\right.$$
$$\left.+\frac{4}{3}(\beta-1)(1-t)^{3/2}\right] \tag{1.95}$$

$$Y = \frac{P}{2\pi}\frac{1}{(2\beta-1)}\left[\frac{2}{3}\left\{2\beta^{1/2}(\beta-1)^{1/2}-2\beta+1\right\}t^{3/2}+2\beta t^{1/2}\right] \tag{1.96}$$

The area, A, can be calculated directly and the solutions are represented as a curve of $P/A^{1/2}$ against $\varepsilon A/\Gamma$ in Figure 1.5. It shows that for $0 < \varepsilon A/\Gamma < 0.035$ there is one solution, for $0.035 < \varepsilon A/\Gamma < 0.10$, two solutions and for $\varepsilon A/\Gamma > 0.10$ no solutions. It should be mentioned that

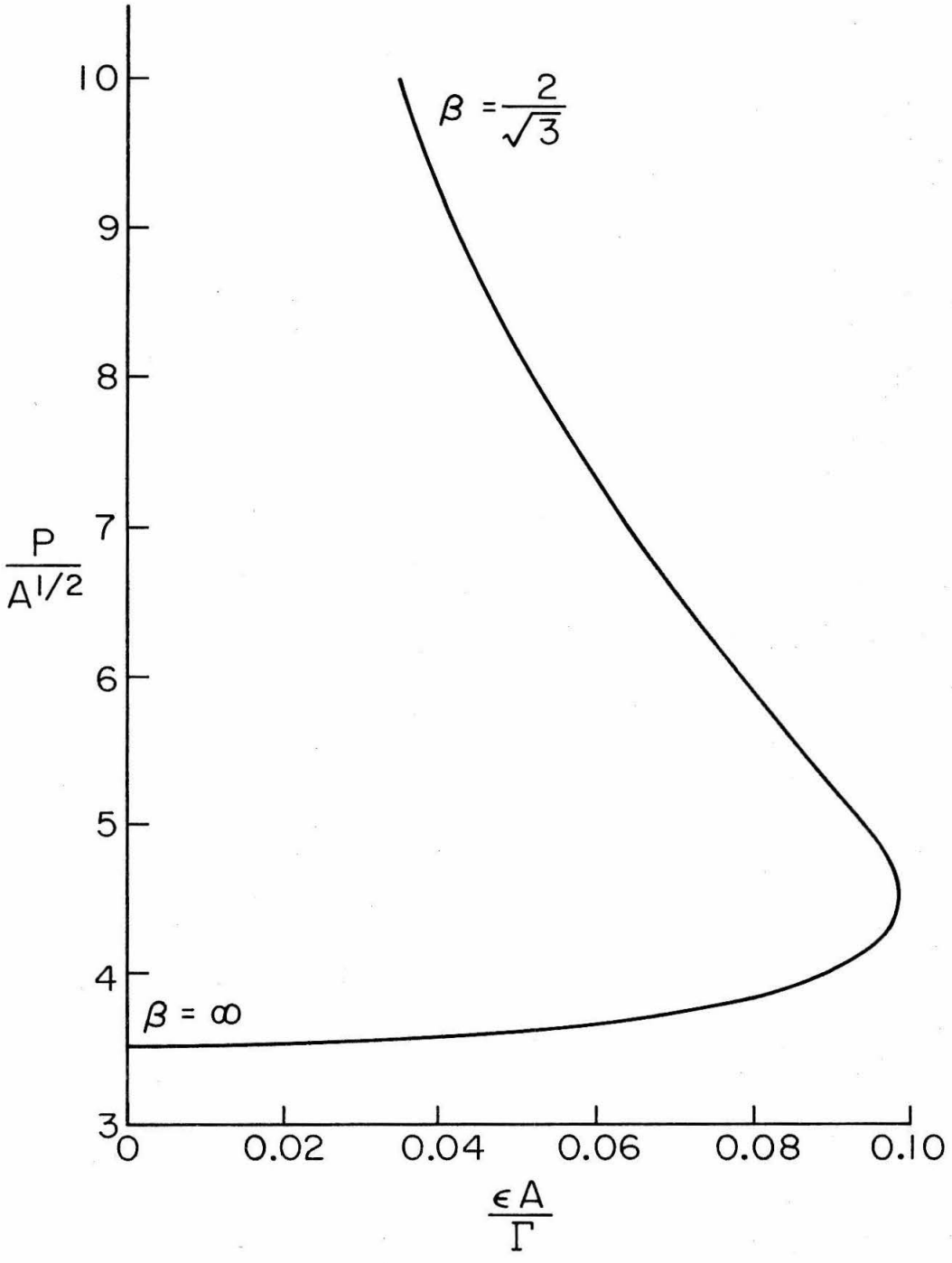

The perimeter length, a measure of the deformation, as a function of the rate of strain.

Figure 1.5

$\beta \to \infty$ corresponds to $\varepsilon \to 0$ and the solution is circular, but as $\beta \to \frac{2}{\sqrt{3}}$, the shape is pinched in the middle. Some interesting questions arise about whether the shape separates and if there is a continuation of the solution for increasing strain rate. Unfortunately analysis is algebraically complex for determining the stability of the solution found for the single hollow vortex and has not been pursued.

The question of what happens to the vortex or the array in the region where no steady solutions exist is unresolved. There could be stable periodic solutions or alternatively and perhaps more likely, there is a disintegration process. Moore and Saffman (1975) related the single vortex with uniform core of constant vorticity in a straining field to a member of a regular array by approximating the rate of strain with $\varepsilon = \pi\Gamma/6L^2$. Taking the maximum value $\varepsilon A/\Gamma = 0.10$ and using $\varepsilon = \pi\Gamma/6L^2$ one obtains an estimate for the critical value of $A^{1/2}/L = 0.43$ for the array where steady solutions cease to exist. The exact value as calculated in Section III is $A^{1/2}/L = 0.38$ and suggests the approximation is not unreasonable. Moreover $P/A^{1/2}$ has the values 4.2 and 4.5 respectively for the two cases.

APPENDIX

Here, the calculation is presented which demonstrates that the symmetry assumed in Hill's (1975a) solution is in fact required. The physical plane and mapped planes are shown in Figures 1.6a,b,c and d. Once again $z = x + iy$ and $w = \phi + i\psi$

The Schwarz-Christoffel transformations which take first the w plane to ζ plane ($\zeta = \xi + i\eta$) and then to the t plane ($t = r + is$) are

$$w = \frac{iT}{2\pi} \frac{\zeta(\zeta+1)^{1/2}(\zeta-1)^{1/2}}{(2\alpha^2-1)} - \frac{iT}{2\pi} \log\left[\zeta + (\zeta+1)^{1/2}(\zeta-1)^{1/2}\right] - \frac{T}{4} \qquad (A.1)$$

$$\zeta = \sin t \qquad (A.2)$$

If one considers $\Omega = \log\left(\frac{dw}{dz}\frac{1}{q_0}\right) = \tau + i\sigma$ then Ω must be an analytic function in the ζ plane except at the stagnation points. The correct behaviour at the stagnation points must be taken into account and the asymptotic behaviour must be like a straining field. The behaviour near a stagnation point is $\frac{dw}{dz} \sim (w - w_0)^{1/2}$ and so for ζ near $-\beta, \beta$ one finds

$$\frac{dw}{dz} \sim (\zeta + \beta)\ ,\ (\zeta - \beta) \quad \text{respectively} \qquad (A.3)$$

Therefore

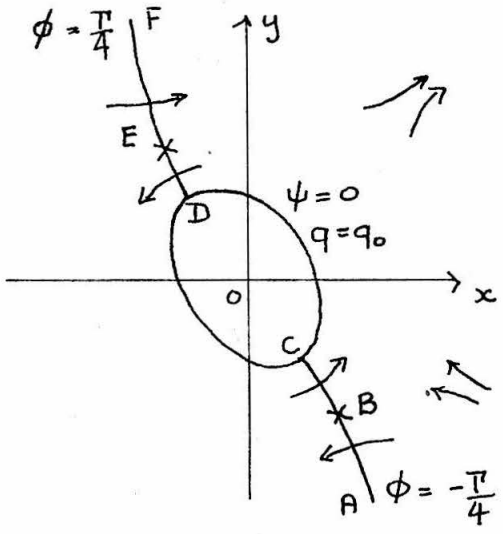

a) **The physical plane,** $z = x + iy$

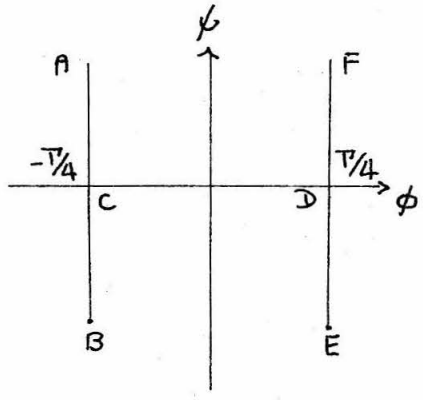

b) **The potential plane,** $w = \phi + i\psi$

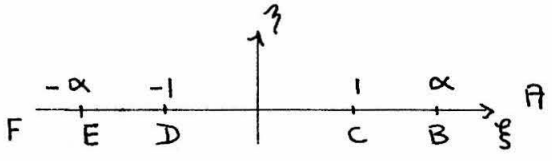

c) **The** ζ **plane,** $\zeta = \xi + i\eta$

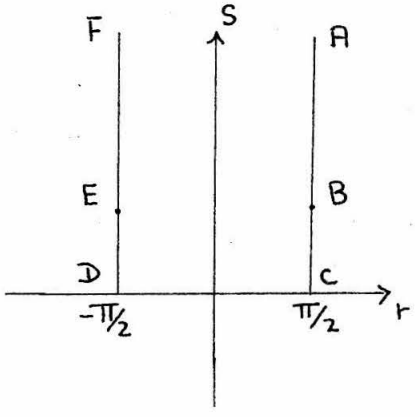

d) **The** t **plane,** $t = r + is$

Figure 1.6

$$\tau \sim \log|\zeta+\beta| + \log|\zeta-\beta| \tag{A.4}$$

Since a stagnation point looks locally like a straining flow it is easy to see that far from the vortex, i.e. $\zeta \to -\infty$ in upper half plane,

$$\frac{dw}{dz} \sim -i\varepsilon\left(\frac{2iw}{\varepsilon}\right)^{1/2} \sim -\frac{(\varepsilon\Gamma)^{1/2}}{\pi^{1/2}}\frac{1}{(2\alpha^2-1)^{1/2}}\zeta \tag{A.5}$$

From the reflectional symmetry requirement, one sees that τ and its normal derivative must be equal at corresponding points along AC,DF. By considering

$$\tau = \log|\sin t-\beta| + \log|\sin t+\beta| - s + \log 4\frac{(\varepsilon c)^{1/2}}{q_0} + H(r,s) \tag{A.6}$$

where $C = \frac{\Gamma}{\pi}\frac{1}{(2\alpha^2-1)}$, H satisfies Laplace's equation and the symmetry conditions. As $s \to \infty$,

$$\tau \to s + \log\frac{4(\varepsilon c)^{1/2}}{q_0} \tag{A.7}$$

as required, provided $H(r,s)\to 0$. And so the solution for H(r,s) is

$$H(r,s) = \sum_{n=0}^{\infty}\left(a_n \sin 2nr + b_n \cos 2nr\right)e^{-2ns} \tag{A.8}$$

For $s = 0$, $\tau = 0$ implies

$$\log(\beta + \sin r) + \log(\beta - \sin r) + \log \frac{4(\varepsilon C)^{1/2}}{q_0}$$

$$+ \sum_{n=0}^{\infty} (a_n \sin 2nr + b_n \cos 2nr) = 0 \qquad \text{(A.9)}$$

Clearly $a_n = 0$, and this establishes the symmetry as assumed by Hill (1975a), i.e. symmetry about $\phi = 0$. Finally, $b_0 = 0$ reduces to the condition (1.93) with $\alpha = \beta^{1/2}$.

Chapter 2

Numerical Studies of the Roll-up of Two Dimensional Vortex Sheets in Homogeneous Fluid

I. INTRODUCTION

In this chapter, the unsteady motion of a two-dimensional vortex sheet in a homogeneous fluid will be considered. Inviscid theory predicts that sharply defined sheets of vorticity will move with fluid and maintain their sharpness. The equations describing the motion are non-linear and there are no known analytic results which describe the complete solution for the unsteady case. This chapter is concerned with numerical techniques which can be used to study the time evolution of vortex sheets. In particular, two-dimensional approximations to the vortex sheets generated by the flow past conventional wings and past ring wings will be used as examples, as the way in which these roll up into circular vortices of finite core size is of considerable interest and importance.

The first numerical studies of vortex sheet roll-up were by Rosenhead (1931) and Westwater (1935). The vortex sheet is replaced by a finite number of discrete vortices and their motion followed in time. The subsequent positions of the point vortices are considered markers for the vortex sheet. With the advent of high speed computers, this basic discretisation has been used by a large number of authors.

However, unsatisfactory features of this method have been uncovered, namely that chaotic motion ensued. The first reports of this are by Birkhoff and Fisher (1959), Takami (1964) and Moore (1971). They find that although the vortices appear to give a qualitative description of the roll-up, irregularities always occur, particularly in the roll-up region.

Takami (1964) increases the number of point vortices from eight to twenty per half-wing, but he finds no improvement in the details of the vortex sheet in the roll-up region. Moore (1971) uses even larger numbers of vortices and integrates the equations of motion for the point vortices very accurately in an attempt to establish whether the growth of truncation errors in the numerical integration is causing the chaotic state of the vortices. His results leave no doubt that the cause of the difficulties is elsewhere.

Ad hoc methods have been introduced to overcome these difficulties. Chorin and Bernard (1972) introduce a finite core to the point vortex inside of which the singular behaviour of the velocity is removed. Instead of the exact equations of motion for a collection of point vortices, whose positions are $\{(x_i, y_i)\}$ and whose circulations are $\{K_i\}$,

$$\frac{dx_i}{dt} = -\frac{1}{2\pi} \sum_{j \neq i} \frac{K_j (y_i - y_j)}{r_{ij}^2} \qquad (2.1)$$

$$\frac{dy_i}{dt} = \frac{1}{2\pi} \sum_{j \neq i} \frac{K_j (x_i - x_j)}{r_{ij}^2} \qquad (2.2)$$

where $r_{ij}^2 = (x_i - x_j)^2 + (y_i - y_j)^2$, they use

$$\frac{dx_i}{dt} = -\frac{1}{2\pi\sigma} \sum_{j \neq i} \frac{K_j (y_i - y_j)}{r_{ij}} \tag{2.3}$$

$$\frac{dy_i}{dt} = \frac{1}{2\pi\sigma} \sum_{j \neq i} \frac{K_j (x_i - x_j)}{r_{ij}} \tag{2.4}$$

whenever $r_{ij} < \sigma$ and (2.1), (2.2) for $r_{ij} > \sigma$. As a result, smooth spirals are achieved for much longer times. Chorin and Bernard (1972) report that the results do not depend on σ if it lies within a wide range around the smallest initial spacing between the point vortices. They also claim that this cut-off in the velocity near a point vortex is analogous to incorporating an artificial viscosity.

Kuwahara and Takami (1973) also introduce an artificial viscosity. Instead of (2.1) and (2.2), they use

$$\frac{dx_i}{dt} = -\frac{1}{2\pi} \sum_{j \neq i} K_j \left\{ 1 - \exp\left(-\frac{r_{ij}^2}{4\nu t} \right) \right\} \frac{(y_i - y_j)}{r_{ij}^2} \tag{2.5}$$

$$\frac{dy_i}{dt} = \frac{1}{2\pi} \sum_{j \neq i} K_j \left\{ 1 - \exp\left(-\frac{r_{ij}^2}{4\nu t} \right) \right\} \frac{(x_i - x_j)}{r_{ij}^2} \tag{2.6}$$

Although each term of the sums represent the velocity of a viscous vortex which at $t = 0$ is a point vortex, the non-linearity of the Navier-Stokes equations does not permit the superposition of the velocity fields. Kuwahara and Takami (1973) find that, although the details of the spiral are restored, the way in which this occurs depends on the choice

for ν .

Moore (1974), on the other hand, incorporates vortices into a main vortex at the centre of the spiral whenever a measure of the curvature becomes larger than some chosen value. As Moore (1974) points out, there are unsatisfactory factors in the methods adopting cut-off radii in the calculation of the velocity. In particular, in Chorin and Bernard's (1974) work, the point vortices accumulate towards the centre of the spiral in contradiction to the analysis by Kaden (1931) who shows that the sheet is increasingly stretched towards the spiral centre. Since a finite number of vortices cannot represent the infinite number of turns of a spiral, Moore (1974) suggests that the flow field is poorly approximated by a few point vortices in the region of the spiral centre and so he amalgamates them in an attempt to regularise the approximation to the flow. His results show smooth spirals beyond the time at which previous authors stopped. Moreover, the vortex points move apart, indicating that the sheet is stretching in agreement with Kaden's (1931) analysis.

Fink and Soh (1974) are the first authors who attempt to obtain error estimates for the approximation of a vortex sheet by a finite collection of point vortices. In particular, they show that unless the vortices are evenly spaced in arclength, the error in calculating the velocity by means of (2.1) and (2.2) is $O(\log h_1/h_2)$ where h_1, h_2 are adjacent

spacings between points. This suggests that as the vortex points move and lose their uniform spacing, the error in calculating the velocity will grow and eventually destroy the description of the sheet. They therefore propose a method whereby the vortices are continually redistributed to ensure even spacing. Their results looked promising and one of the purposes of this chapter is to examine their approach in detail.

The first section discusses the errors in numerically calculating, by different methods, the velocity of a vortex sheet at certain points, i.e. mesh points. There is confirmation of Fink and Soh's (1974) estimate of the error when calculating the velocity by means of certain principal value integrals of the vortex sheet strength using the usual point vortex discretisation. It is necessary therefore to ensure that the vortices are evenly spaced at all times. For a closed sheet (e.g. the sheet generated by a ring wing), an accurate method ($O(h^3)$) is developed using the trapezoidal rule and the analysis is checked by some test examples. It is also concluded that the velocity of a vortex sheet generated by a conventional wing (i.e. finite in length) cannot be accurately calculated near the wing tip, unless some consideration of the asymptotic behaviour in the inner regions of the spiral (Kaden (1931)) is included.

Section III incorporates these results in detailing Fink and Soh's (1974) method. Ways to improve the accuracy

of their method are suggested and the results are presented in Section IV. However, it is found that instabilities unphysical in nature keep occurring despite variations of the details of the method. Increasing the number of vortex points used in the method fails to suppress the instabilities and there appear to be only two possibilities to account for the failure of the numerical method. The instabilities may be entirely numerical in origin or small scale structures may be important in influencing the flow.

The latter possibility means that many vortex points are required and the usual methods, including the one developed by Fink and Soh (1974), prove uneconomical. An alternative method based on "Cloud in Cell" techniques is presented in Section V. Christiansen (1973) makes use of the particle simulation techniques developed in plasma physics and adopts them to vortex flow in an incompressible, two-dimensional laminar fluid. For more details about particle simulation techniques, see Alder, Fernbach and Rotenberg (1970).

To explore the role of small scales and their growth, a test case is considered. The results are interesting, in particular the indications of the cascade process of small scales to larger ones. This method is applied to the ring wing case and the results are presented in Section V. There is clear evidence of the development of large structures and this occurs in two ways. In some cases, two different but

neighbouring vortex structures amalgamate, and in other cases, a vortex structure is pulled apart and absorbed by its neighbours. These results must still be regarded as tentative until the numerical errors associated with the technique are fully understood.

II. THE CALCULATION OF THE VELOCITY OF A VORTEX SHEET

Before an outline of Fink and Soh's (1974) method is given, it is useful to examine the ways in which the velocity of a vortex sheet can be calculated. It is this calculation which essentially determines the accuracy of the method in terms of the number of vortex points used. Numerical consistency will be an important requirement, i.e. as the number of vortex points is increased, the velocity calculated numerically must approach the exact velocity of the vortex sheet. In terms of an error analysis, the error associated with the discretisation must vanish as the spacing between the vortex points tends to zero.

Perhaps it should be emphasized here that questions of stability for any numerical method applied to vortex sheets remain unresolved. In fact, the straight uniform vortex sheet is known to be unstable (Batchelor (1970), Ch 7.1) and the modes with shortest wavelengths have the greatest growths. This suggests a basic ill-posedness, i.e. as the length scales of the numerical method are decreased, the more different is the behaviour of the solutions. On the other hand, Moore (unpublished) has examined the stability of a vortex sheet in some cases and shows that stretching of the sheet may stabilise its motion. The lack of knowledge about the stability of vortex sheets is a disadvantage in testing any numerical method.

In two dimensions, the velocity components of the

fluid are related to the vortex strength by

$$u(x,y) = -\frac{1}{2\pi}\int \frac{\gamma(s)\,(y'(s)-y)}{r^2}\,ds \tag{2.7}$$

$$v(x,y) = \frac{1}{2\pi}\int \frac{\gamma(s)\,(x'(s)-x)}{r^2}\,ds \tag{2.8}$$

where $(x'(s), y'(s))$ describes the location of the sheet parametrically determined by s, the arclength. The integration is along the sheet and

$$r^2 = (x'(s)-x)^2 + (y'(s)-y)^2 \tag{2.9}$$

In particular, the velocity of a point $(x'(s_0), y'(s_0))$ on the sheet is given by the principal value integrals

$$u(s_0) = -\frac{1}{2\pi}\,\mathcal{P}\int \frac{\gamma(s)\,(y'(s)-y'(s_0))}{r^2}\,ds \tag{2.10}$$

$$v(s_0) = \frac{1}{2\pi}\,\mathcal{P}\int \frac{\gamma(s)\,(x'(s)-x'(s_0))}{r^2}\,ds \tag{2.11}$$

There are two distinct cases to consider depending on whether the vortex sheet forms a closed curve or an open one. An example of each case is presented and it will be seen that there are crucial differences in the accuracy of the numerical approximations when applied to each case. For the case of vortex sheet forming an open curve, a two-dimensional approximation to the sheet shed from a conventional

wing is used as an example. It is very difficult to analyse the accuracy in determining the velocity of the sheet for this case due to the singular nature of the flow at the wing tip. In contrast, the flow over a ring wing (see Figure 2.8) forms a closed vortex sheet with no difficulty in examining the error in the calculated velocity and so accurate numerical methods can be devised.

For an elliptically loaded wing, γ does not vanish at the wing tips; the integrals (2.10) and (2.11) diverge and appear to predict infinite velocities. What actually happens was elucidated by Kaden (1931). At $t = 0$, the sheet lies along the span of the wing. Since $\gamma \sim s^{-\frac{1}{2}}$ at the wing tip, the velocity is infinite there, but for $t > 0$, the sheet possesses a completely new description. It becomes infinitely long, ending in a spiral which grows in size with time. This nonuniform change in behaviour and the singularity at the tip present great difficulty in solving numerically the evolution of the sheet in time.

Since the infinite sheet is approximated by a finite number of vortex points, the question of how well the spiral is represented is important. The vortex point closest to the spiral centre has to approximate the effect of the infinite number of turns in the inner part of the spiral and the validity of this approximation is still an open question. Moore (1975) has shown that the asymptotic form of the roll-up depends on information from the complete sheet and is not

determined by local considerations only. The converse may equally be true. The motion of any part of the sheet may depend on the structure of the spiral.

Furthermore, the initial discretisation of the vortex sheet may introduce large errors near the wing tip. If the sheet lies along the x-axis $0 \le x \le 2L$, the velocities are determined from (2.10) and (2.11) as

$$u(x_0) = 0$$

$$v(x_0) = \frac{1}{2\pi} \oint \frac{\gamma(x)}{x - x_0}\, dx \qquad (2.12)$$

Dividing the sheet into N equal intervals and using a centred Euler difference approximation to calculate (2.12), one finds the largest error occurs at the point closest to the wing tip singularity.

$$v\left(\tfrac{h}{2}\right) - \frac{h}{2\pi} \sum_{n=1}^{N-1} \frac{\gamma\left((n+\tfrac{1}{2})h\right)}{nh} = \frac{1}{2\pi} \oint_0^h \frac{\gamma(x)}{x - h/2}\, dx$$
$$+ \frac{1}{2\pi} \sum_{n=1}^{N-1} \left[\int_{nh}^{(n+1)h} \frac{\gamma(x)}{x - h/2}\, dx - \frac{h\,\gamma\left((n+\tfrac{1}{2})h\right)}{nh} \right] \qquad (2.13)$$

where $Nh = L$. The right hand side of (2.13) gives the error in using evenly spaced point vortices to represent the vortex sheet. Substituting the behaviour of the vortex sheet strength of an elliptically loaded wing near the wing tip, $\gamma \sim s^{-1/2}$, the error is $O\left(h^{-1/2}\right)$ for the vortex point

closest to the tip. The initial vertical velocity, $v(x)$, is constant along the sheet, except at the wing tips (Batchelor (1970), Ch 7.8). The point vortices, however, give a velocity which immediately distorts the sheet from a straight line. The error estimate of $O(h^{-\frac{1}{2}})$ may be slightly inappropriate since the more important question is whether the velocity determined by the point vortices approximates well the initial sheet with infinitesimal spirals at its tips. The analytic complexity involved in the integrals (2.10) and (2.11) prevents an easy answer to this question. It does seem unlikely though, that a finite number of point vortices is a good approximation to even this case.

The best numerical methods therefore are those which attempt to take into special consideration the initial motion of the sheet and also the centre region of the spiral. Moore (1974) amalgamates vortices into the vortex point closest to the spiral centre whenever the curvature at the next nearest vortex point becomes too large. Fink and Soh (1974) have an independent way of accumulating circulation at the spiral centre, and their results agree well with Moore (1974). These results are presented in more detail in the following sections. However, there can be little hope of knowing how accurate these approximations are until methods are developed which incorporate the asymptotic form of the roll-up found by Kaden (1931) and extended by Moore (1975), and there is a better treatment of the initial motion

of the sheet.

There is a further error in calculating the velocity of a vortex sheet if the vortex points representing it are not evenly spaced. If a centred Euler difference is adopted to integrate (2.10) and (2.11) and the initial vortex sheet is discretised by evenly spaced vortex points, then, for later times, the centredness of the difference formulae is destroyed as the vortices move apart more rapidly at some places than others. Fink and Soh (1974) point out that in this situation the error in calculating the velocity of the vortex sheet has order, $O\left(\log \frac{h_1}{h_2}\right)$ where h_1 and h_2 are adjacent spacings between the vortex points. It is therefore important to maintain a discretisation of the sheet which has uniform spacing between vortex points.

The second case to consider is where the vortex sheet forms a closed curve in the (x,y) plane. A simple example of this is the flow around a ring wing, and it will be seen that there are none of the difficulties associated with the singularity at the wing tip in the previous case. If the sheet is continuous and of finite length, then all the quantities associated with the sheet are periodic functions of the arclength, and this fact enables one to develop improved numerical methods to determine the velocity.

The integrals (2.10) and (2.11) are, in this case,

$$u(s_0) = -\frac{1}{2\pi} \oint_{-L}^{L} \frac{\gamma(s)\,(y'(s) - y'(s_0))\,ds}{[x'(s) - x'(s_0)]^2 + [y'(s) - y'(s_0)]^2} \qquad (2.14)$$

$$v(s_0) = \frac{1}{2\pi} \oint_{-L}^{L} \frac{\gamma(s)\,(x'(s) - x'(s_0))\,ds}{[x'(s)-x'(s_0)]^2 + [y'(s)-y'(s_0)]^2} \tag{2.15}$$

where all quantities have the same value at $S = -L$ as they do at $S = L$. There is no loss in generality in taking $S_0 = 0$. Subtracting from (2.14), the integral

$$-\frac{1}{2\pi} \oint_{-L}^{L} \frac{\gamma(0)}{s} \frac{\partial y'(0)}{\partial s}\,ds = 0 \tag{2.16}$$

and from (2.15), the integral

$$\frac{1}{2\pi} \oint_{-L}^{L} \frac{\gamma(0)}{s} \frac{\partial x'(0)}{\partial s}\,ds = 0 \tag{2.17}$$

leads to the following integrands

$$\frac{-\gamma(s)\,(y'(s)-y'(0))}{[x'(s)-x'(0)]^2 + [y'(s)-y'(0)]^2} + \frac{\gamma(0)}{s}\frac{\partial y'(0)}{\partial s} \tag{2.18}$$

$$\frac{\gamma(s)\,(x'(s)-x'(0))}{[x'(s)-x'(0)]^2 + [y'(s)-y'(0)]^2} - \frac{\gamma(0)}{s}\frac{\partial x'(0)}{\partial s} \tag{2.19}$$

Using a Taylor's expansion for small S and noting $\left(\frac{\partial x'}{\partial s}\right)^2 + \left(\frac{\partial y'}{\partial s}\right)^2 = 1 \quad \forall s$,

$$[x'(s)-x'(0)]^2 + [y'(s)-y'(0)]^2 = s^2 + \left[\frac{1}{4}\left(\frac{\partial^2 x'}{\partial s^2}\right)^2 + \frac{1}{4}\left(\frac{\partial^2 y'}{\partial s^2}\right)^2 + \frac{1}{3}\frac{\partial x'}{\partial s}\frac{\partial^3 x'}{\partial s^3} + \frac{1}{3}\frac{\partial y'}{\partial s}\frac{\partial^3 y'}{\partial s^3}\right]_{s=0} s^4 \tag{2.20}$$

The integrands, (2.18) and (2.19) have no singularities provided the sheet is smooth, i.e. has a continuous tangent, and γ has no singularities.

In order to obtain error estimates when using the trapezoidal rule on the integrands (2.18) and (2.19), a small digression is made. If $f(s) \in C^{2m+1}[-L,L]$, the Euler-McLaurin summation formula used on a mesh $S = \{nh\}$, $-N \le n \le N$ $Nh = L$, gives,

$$\int_{-L}^{L} f(s)\,ds = \frac{h}{2}\left[f(-L) + f(L)\right] + h\sum_{n=-N+1}^{N-1} f(nh) + \sum_{k=0}^{m} C_k h^{2k+2}\left[f^{(2k+1)}(L) - f^{(2k+1)}(-L)\right] + C_m h^{2m+2} f^{(2m+1)}(\xi) \quad (2.21)$$

where C_k are constants independent of h and $f(s)$, and $-L \le \xi \le L$. It is easy to recognise the first two terms as the trapezoidal rule and that the error is given by

$$E = \sum_{k=0}^{m} C_k h^{2k+2}\left[f^{(2k+1)}(L) - f^{(2k+1)}(-L)\right] + C_m h^{2m+2} f^{(2m+1)}(\xi) \quad (2.22)$$

The first terms of the integrands (2.18) and (2.19) are periodic and so their contributions to the sum in (2.22) vanish. Since $\left(\frac{1}{s}\right)^{(2k+1)} \sim \frac{1}{s^{2k+2}}$ is even, the second term in the integrand also produces no contribution to the sum, and the conclusion is that $E \sim Ch^{2m+2}$. However, there is

another contribution to the error resulting from evaluating the integrands at $s=0$ (or $\eta=0$). They have indeterminate form there but have the following limits

$$-\frac{\partial\gamma(0)}{\partial s}\frac{\partial y'(0)}{\partial s} - \frac{\gamma(0)}{2}\frac{\partial^2 y'(0)}{\partial s^2} \tag{2.23}$$

$$\frac{\partial\gamma(0)}{\partial s}\frac{\partial x'(0)}{\partial s} + \frac{\gamma(0)}{2}\frac{\partial^2 x'(0)}{\partial s^2} \tag{2.24}$$

Difference formulae have to be used to evaluate (2.23) and (2.24) and provided the integrands have the property that m is large enough, the error introduced by using the difference formulae will dominate for h small enough. In particular, using the central difference formulae ,

$$\frac{\partial f}{\partial s}(nh) = \left[f((n+1)h) - f((n-1)h)\right]/2h \tag{2.25}$$

$$\frac{\partial^2 f}{\partial s^2}(nh) = \left[f((n+1)h) - 2f(nh) + f((n-1)h)\right]/h^2 \tag{2.26}$$

the error in determining (2.23) and (2.24) is $O(h^2)$ and the error in using the trapezoidal rule is therefore $O(h^3)$.

This analysis is checked here for two cases where the velocities and hence vortex sheet strength are both known instantaneously. At this stage the motion of the sheet is not important; the check is to see how well the velocity is calculated by the method outlined. Taking the sheet to be circular, the fluid velocities are easily known from the

velocity potential. When the sheet is elliptic, elliptic coordinates can be used to determine the velocity potential. In particular, the flow which has a stagnant core inside the ellipse and a non-zero circulation around it, is also used as a check on the method. The results presented in tabular form in Figure 2.1, clearly show the $O(h^3)$ behaviour, i.e. doubling the number of vortex points decreases the error by a factor of eight. The relative error for $L/40$ is typically 10^{-4} and is the limit obtainable using single precision, on IBM 370/158.

Finally, the considerations above have assumed the sheet does not fold back on itself so that different parts of the sheet come close together. When this occurs, large errors will appear unless additional vortex points are added to resolve the large peaks that arise in the integrands (2.14) and (2.15) as the denominator becomes small (see Maskew (to be published)).

In summary, the roll-up of the vortex sheet behind a conventional wing cannot be accurately calculated until some account is taken of the asymptotic nature of the inner turns of the spiral. Since there is no singular behaviour in the vortex sheet behind a ring wing, this case presents a far less complicated test of any numerical method designed to calculated the evolution of vortex sheets.

Having demonstrated the importance of calculating the velocity by using evenly spaced points in arclength, the

N	Calculated u	Error in u	Calculated v	Error in v
5	0.2129180	-0.003588	-0.1238720	0.001128
10	0.2160456	-0.000460	-0.1248536	0.000146
20	0.2164471	-0.000059	-0.1249822	0.000018
40	0.2164967	-0.000010	-0.1249989	0.000001
80	0.2165025	-0.000004	-0.1250024	0.000002.

a) Circular sheet, radius = 1 ; $\gamma = \sin\theta$; velocities determined at $\theta = \pi/3$
Exact velocities, $u = 0.2165063$, $v = -0.125$

N	Calculated u	Error in u	Calculated v	Error in v
10	-0.6465092	0.001254	-0.5326822	-0.002677
20	-0.6476290	0.000134	-0.5303204	-0.000315
40	-0.6477448	0.000019	-0.5300345	-0.000029

b) Elliptic sheet, $\frac{x^2}{2} + y^2 = 1$ **; stagnant core and rotating flow outside**

$$\gamma = -2/\left\{\left[(x-1)^2 + y^2\right]^{1/4}\left[(x+1)^2 + y^2\right]^{1/4}\right\}$$

Exact velocities, $u = -0.6477635$, $v = -0.5300051$

Table showing errors for velocity calculation.

Figure 2.1

next section establishes how to calculate the time evolution with this condition.

III. REDISTRIBUTION OF VORTEX POINTS AS A WAY TO FOLLOW THE MOTION OF A VORTEX SHEET

This section provides the details of the method originally used by Fink and Soh (1974) and discusses different ways of improving the accuracy. The basic outline is as follows. A function $\Gamma(s)$ is introduced which measures the total circulation along the sheet from some reference point, s_0. The vortex sheet strength is $\gamma(s) = \frac{d\Gamma}{ds}$. Knowing $\Gamma(s)$ at mesh points $\{(x_i, y_i)\}$ which are evenly spaced in arclength gives a set of values $\{\Gamma_i\}$ which convect with the points $\{(x_i, y_i)\}$ as they move with the fluid. γ_i is calculated from $\gamma = \frac{d\Gamma}{ds}$ and the velocity $\{(u_i, v_i)\}$ can be determined by integrating along the sheet as described in Section II. Fink and Soh (1974) use simple Euler integration to move forward in time with time step Δt,

$$\bar{x}_i = x_i + u_i \Delta t \tag{2.27}$$

$$\bar{y}_i = y_i + v_i \Delta t \tag{2.28}$$

The points $\{(\bar{x}_i, \bar{y}_i)\}$ no longer satisfy the requirement of being evenly spaced in arclength. An interpolation polynomial is used to determine the new points $\{(x_i^*, y_i^*)\}$ which are evenly spaced. Knowing the circulation $\{\Gamma_i\}$ at $\{(\bar{x}_i, \bar{y}_i)\}$ means an interpolation can be made and $\{\Gamma_i^*\}$ found at $\{(x_i^*, y_i^*)\}$. These values $\{(x_i^*, y_i^*)\}$ and $\{\Gamma_i^*\}$ provide the starting values,

$\{(x_i, y_i)\}$ and $\{\Gamma_i\}$, for the next time step.

The details of the various steps are as follows. In the first place, to calculate γ_i , Fink and Soh (1974) use an interpolation polynomial through the points $\{\Gamma_i\}$ known at $\{s_0 + ih\}$ where h is the uniform spacing in arclength. The values of the circulation $\{\Gamma_{i+1/2}\}$ are then found at the midpoints $\{s_0 + (i + 1/2)h\}$ and a central difference formula gives

$$\gamma_i = (\Gamma_{i+1/2} - \Gamma_{i-1/2})/h \qquad (2.29)$$

The accuracy in determining γ_i is $O(h^2)$ provided a suitably accurate interpolation polynomial is used. Fink and Soh (1974) tried both a local three-point and four-point Lagrange interpolation polynomial and the error will be $\frac{h^3}{16}\frac{d^3\Gamma(\xi)}{ds^3}$, $\frac{3}{128}h^4\frac{d^4\Gamma(\xi)}{ds^4}$ respectively, where ξ lies somewhere in the interval of s used in the interpolation (see Isaacson and Keller (1966), p. 264). Alternatively, if a spline interpolation is used, the error in determining γ_i as the derivative of the spline function will be $O(h^3)$. This provides one way to improve on Fink and Soh's (1974) accuracy in determining γ_i .

The determination of the circulation of the vortex point closest to the spiral centre is handled in a slightly different way than by using (2.29). The circulation accredited this vortex point is that which ensures that the total

circulation remains constant in time. This means in essence that the circulation that would be distributed along the inner turns of the spiral, which are beyond the resolution of the finite number of vortex points, is assigned to this vortex point. The accuracy of this procedure is unknown. Using the derivative of a spline interpolation as an alternative method in determining the vortex sheet strength, means that there is no attempt to approximate the inner region of the spiral and the invariance of the total circulation can be used as a check on the error in neglecting this region.

The calculation of the velocity proceeds as detailed in the previous section and so what remains to be done here is to describe the redistribution of the mesh points. Fink and Soh (1974) use the chordlength between mesh points as an approximation to the arclength. There is a simple way to improve on this procedure; the chordlength between points can be calculated and the total chordlength, $\{\lambda_i\}$, from some reference point defines a parametric representation for the sheet.

An interpolating spline can be used through the points $\{\bar{x}_i\}$, $\{\bar{y}_i\}$ as functions of $\{\lambda_i\}$, and the derivatives $\{\frac{d\bar{x}_i}{d\lambda}\}$, $\{\frac{d\bar{y}_i}{d\lambda}\}$, are determined at equal intervals along λ, $\{\lambda_{ei}\}$. The arclength measured from the reference point is defined by

$$S = \int_0^{\lambda} \left[\left(\frac{d\bar{x}}{d\lambda}\right)^2 + \left(\frac{d\bar{y}}{d\lambda}\right)^2 \right]^{1/2} d\lambda \qquad (2.30)$$

This integral can be evaluated numerically. To ensure that the arclength is calculated accurately enough, it is found necessary to evaluate $\{\frac{d\bar{x}_i}{d\lambda}\}$, $\{\frac{d\bar{y}_i}{d\lambda}\}$ at four times as many places as there are mesh points $\{\bar{x}_i\}, \{\bar{y}_i\}$. Although the trapezoidal rule is used to calculate (2.30), the accuracy should be limited mainly by the accuracy of the spline which has an error of $O(h^4)$.

At this point, S is known at $\{s_i\}$ corresponding to equal spacings of λ , $\{\lambda_{ei}\}$. The relationship can be inverted by using an interpolating spline, i.e. consider $\{\lambda_{ei}\}$ as a function of $\{s_i\}$ and determine $\{\lambda_i^*\}$ corresponding to even spacings of S , where the spacing is chosen to give the required number of new mesh points. Finally, the new mesh points $\{x_i^*\}, \{y_i^*\}$ are obtained at $\{\lambda_i^*\}$ by using an interpolating spline passing through $\{\bar{x}_i\}, \{\bar{y}_i\}$ known at $\{\lambda_i\}$.

To complete the process of determining new mesh points, one needs to know the circulation values $\{\Gamma_i^*\}$ at these points. Since $\Gamma(s)$ is constant along the path lines, $\frac{dx}{dt} = u$, $\frac{dy}{dt} = v$, $\{\Gamma_i\}$ is known at the points $\{(\bar{x}_i, \bar{y}_i)\}$, which have resulted from an integration through one time step. Thus $\{\Gamma_i\}$ **is known** at $\{\lambda_i\}$ **and an interpolating spline gives** $\{\Gamma_i^*\}$ **at** $\{\lambda_i^*\}$ **corresponding to** $\{(x_i^*, y_i^*)\}$.

The case of a vortex sheet with infinite arclength needs special consideration. Only a finite number of points are used and so there is no way to redistribute them so that they are evenly spaced along the whole sheet. The point closest to the spiral centre is considered given and the remaining points are redistributed along the finite part of the sheet. This procedure is consistent with the way in which the circulation per vortex point is calculated. As discussed previously in this section, the vortex point closest to the spiral centre is regarded as representing the inner turns of the spiral.

Finally, one can use a more accurate integration procedure to move forward in time than the simple Euler used by Fink and Soh (1974). The modified Euler approach is the essence of this improvement. Using (2.27) and (2.28), a first estimate of the new position is obtained, $\{(\bar{x}_i, \bar{y}_i)\}$. Redistribution gives the points $\{(x_i^*, y_i^*)\}$ where the velocity can be calculated. Interpolation now provides the velocity $\{(\bar{u}_i, \bar{v}_i)\}$ at the points $\{(\bar{x}_i, \bar{y}_i)\}$ and an improved estimate for the new values is obtained by

$$\bar{\bar{x}}_i = x_i + \frac{1}{2}(u_i + \bar{u}_i)\,\Delta t \qquad (2.31)$$

$$\bar{\bar{y}}_i = y_i + \frac{1}{2}(v_i + \bar{v}_i)\,\Delta t \qquad (2.32)$$

The procedure then continues as before.

In conclusion, a note should be made about the interpolation formulae used. A three-point Lagrangian interpolation polynomial is used locally to reproduce the results claimed by Fink and Soh (1974). However, for the improvements listed in this section, a spline can be used with a high degree of accuracy, $O(h^4)$. This is achieved by either using information about the derivatives at the end points, for instance symmetry sometimes requires some derivatives to vanish or take on specific values, or else by using an end point condition suggested by Professor H. B. Keller, i.e.

$$\frac{h_1}{h_1+h_0}\left[\frac{d\tau}{dx}(x_1)-\frac{d\tau}{dx}(x_0)\right]/h_0+\frac{h_0}{h_1+h_0}\left[\frac{d\tau}{dx}(x_2)-\frac{d\tau}{dx}(x_1)\right]/h_1=\frac{d^2\tau}{dx^2}(x_1) \qquad (2.33)$$

where $\tau(x)$ is the spline function and $h_1=x_2-x_1$, $h_0=x_1-x_0$. A similar condition may be applied at the other end. The author is indebted to Professor H. B. Keller for this suggestion.

Results and criticisms of this method are presented in the next section.

IV. NUMERICAL RESULTS FOR METHODS BASED ON REDISTRIBUTION OF VORTEX POINTS

Before giving the results for the conventional wing and the ring wing, the results for a test case are presented indicating that the method works as described in Section III. Although not more than four steps are calculated in the time integration, the exact errors are known and their behaviour with changes in the arclength spacing and in the time step show the correct behaviour.

The details are as follows. An irrotational flow circulating around a stagnant circular core is known to be unstable (see Moore and Griffith-Jones (1974)). However, there are modes which do not grow and one of these can be followed at least for small times. If a is the radius of the circle and V the undisturbed velocity of the outside fluid at the interface, then the undisturbed potential is $\phi = aV\theta$ for $r>a$. Considering perturbations of the form,

$$\zeta = a + \varepsilon \cos(n\theta + \omega t) \tag{2.34}$$

$$\phi = aV\theta + \frac{B}{r^n}\sin(n\theta + \omega t), \qquad r>\zeta \tag{2.35}$$

$$\phi = Ar^n \sin(n\theta + \omega t), \qquad r<\zeta \tag{2.36}$$

and linearising, the dispersion relation is

$$\omega^2 + n\omega\frac{V}{a} + \frac{V^2}{2a^2}n(n-1) = 0 \tag{2.37}$$

The two modes tested, $n=1$, $\omega=0$ and $n=2$, $\omega=-\frac{V}{a}$ are stable. For these cases, $\alpha=0$, $\frac{\varepsilon V}{2a^2}$ respectively inside the boundary and $\beta=\varepsilon V a$, $\varepsilon V\frac{a^2}{2}$ respectively outside the boundary. The method applied includes the following improvements to the basic method described by Fink and Soh (1974); arclength is calculated accurately for redistribution purposes and spline derivatives are used to find the new vortex sheet strengths (instead of (2.79)). In Figure 2.2 there is a table of errors using simple Euler or modified Euler integration for different time steps. As expected, halving the time step Δt reduces the error for simple Euler by half, confirming $O(\Delta t)$ behaviour. Since modified Euler integration works exactly for circular motion, the errors obtained using this method are small. Comparison with Figure 2.1 shows that the errors in calculating the velocity are much smaller than those for the time integration. This is confirmed by finding no change in the errors in Figure 2.2 when the number of points is varied from 20, 40 to 80. Although this confirms the accuracy of the method, it says nothing about its stability. Questions concerning numerical stability will remain unanswered.

The method is now applied to the flow associated with the vortex sheet shed by an elliptically loaded wing. Making use of the symmetry of the flow, one need consider only one side of the flow field; see Figure 2.3 for details. Non-dimensionalising the problem by introducing a characteristic

Timestep	Simple Euler	Modified Euler
0.1	0.00125	~0.00001
0.05	0.000625	~0.00001
0.025	0.00031	~0.00001

Errors obtained at $t=0.1\frac{a}{V}$ for both modes considered.

Figure 2.2

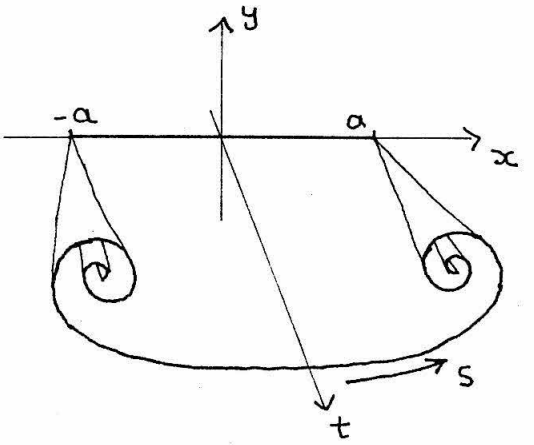

The roll-up of the vortex sheet

Figure 2.3

distance, a, which is half the total span of the wing, a characteristic velocity, V, which is the instantaneous speed downwards of the initial vortex sheet and a characteristic time, a/V, the initial vortex sheet strength is

$$\gamma(s) = \frac{2s}{(1-s^2)^{1/2}} \tag{2.38}$$

and the initial circulation is

$$\Gamma(s) = -2(1-s^2)^{1/2} \tag{2.39}$$

N points are introduced at $y_i = 0$, $x_i = (i-\frac{1}{2})h$, $1 \le i \le N$, and $Nh = 1$. Before reproducing the results obtained by Fink and Soh (1974), the formula used in assigning circulation to the point closest to the spiral centre is given explicitly. Knowing the circulation at $\Gamma(s_N - \frac{h}{2})$ where h is the latest even spacing between redistributed points, the circulation assigned to the vortex point (x_N, y_N) is

$$h\gamma_N = -\Gamma(s_N - \tfrac{h}{2}) \tag{2.40}$$

This ensures the conservation of circulation and Fink and Soh (1974) use the vertical impulse, another invariant of the flow,

$$I_v = \frac{1}{2}\int_0^L x\,\gamma(s)\,ds = \frac{\pi}{4} \tag{2.41}$$

as a check on the accuracy of their computation.

Figure 2.4 shows the results for the roll-up at $t^* = \frac{tV}{a} = 0.25$ with time step 0.0025 and the number of points is twenty. The curves are obtained by use of Fink and Soh's method with the end-condition (2.40). The profile of the roll-up looks qualitatively like the results they published, (1974). Unfortunately, quantitative agreement with their results is not possible since the non-dimensionalisation they use is not clear and the scales on their Figure 11 are not indicated. However, there is good agreement with the variation of the vertical impulse. They report the centroid remained at $0.7915 \pm 0.0008a$ compared to the author's result of 0.7917 ± 0.0013 . The slight difference may be a result of the comparison being made for different numbers of mesh points.

Fink and Soh (1974) did not comment on the profile of the vortex sheet strength. It is found to develop oscillations in the region of the roll-up. Examples of this are seen in Figures 2.4 and 2.5. The strength of the oscillations and their particular form depend on the actual method used. In some cases the vortex sheet strength actually becomes negative, which is unphysical in behaviour.

It is interesting to compare the results as shown in Figure 2.4 with the result obtained by Moore (1974) and presented in his Figure 5. The agreement is reasonable and suggests there may be some validity in specifically

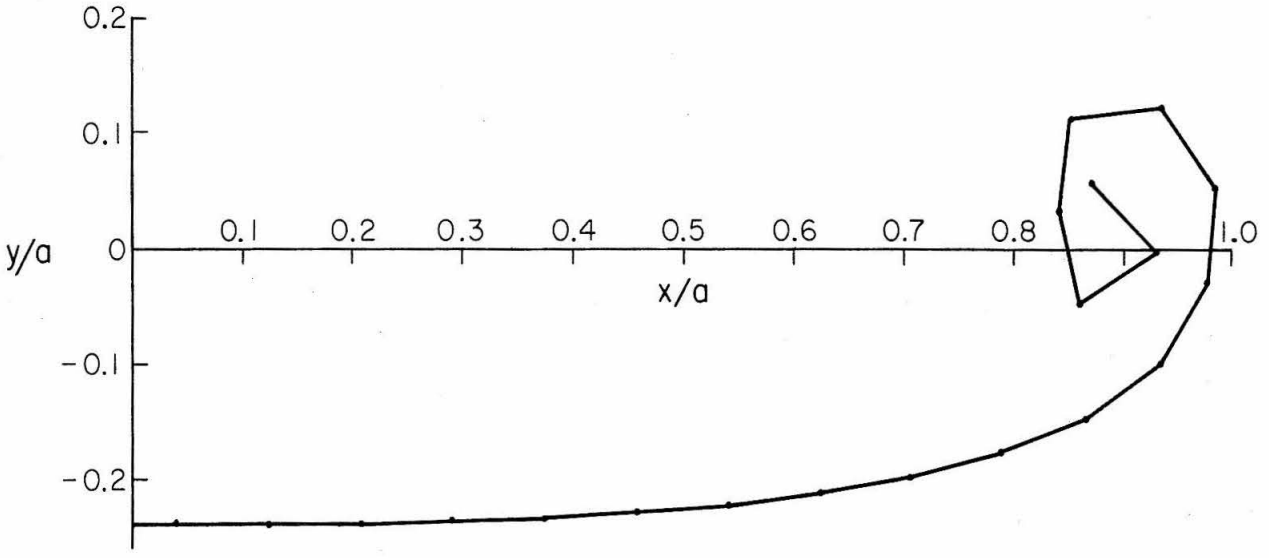

The roll-up of the vortex sheet at $t = 0.25\, a/V$

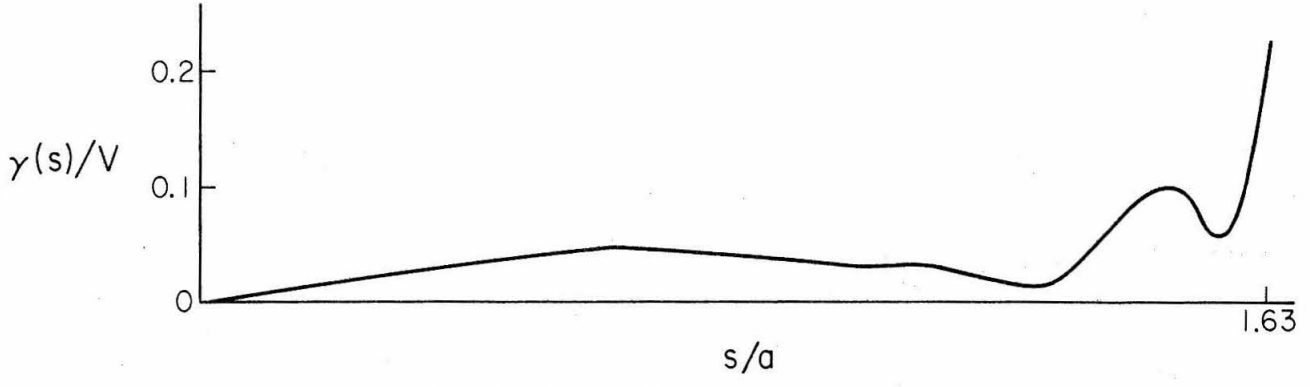

The vortex sheet strength as a function of arclength

Figure 2.4

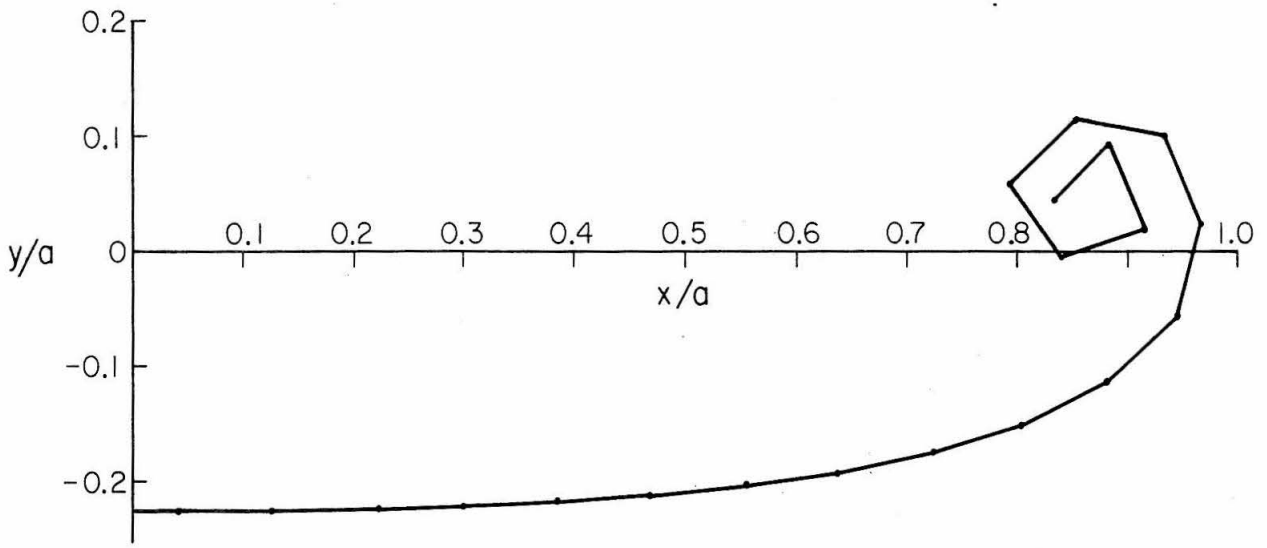

The roll-up of the vortex sheet at $t = 0.25\, a/V$

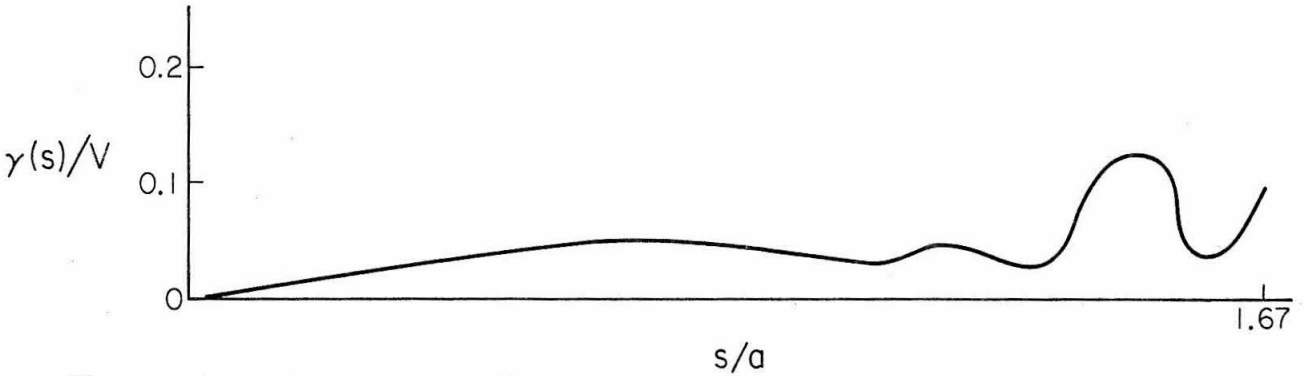

The vortex sheet strength as a function of arclength

Figure 2.5

accumulating vorticity at the spiral centre.

Figure 2.5 shows the alternative profiles when some improvements are implemented. The arclength of the sheet is calculated using intermediate points obtained by spline interpolation and then using Simpson's formula for the integration (2.30). Spline derivatives are used to evaluate $\gamma = \frac{d\Gamma}{ds}$ at the mesh points but the integration forward in time is still only using a simple Euler time step. The improved accuracy results in a tighter spiral with more turns. The oscillations in the vortex sheet strength are larger. The variations in the circulation for half the wing lie between $1.74\ V_\infty$ and $1.94\ V_\infty$ while the variations in the x-coordinate of the centroid lie between $0.758\ a$ and $0.775\ a$. The circulation for half the wing should in fact be a constant, $2.0\ V_\infty$. Thus, at worst, about fifteen percent of the circulation is not accounted for and probably is the circulation that would correspond to the innermost part of the spiral. This also suggest a rough estimate of the importance of accumulating vorticity at the spiral centre.

It is in the process of improving the accuracy of the time integration that an interesting restriction on the method comes to light. Figure 2.6 shows the motion of the point vortices in the vicinity of the tip during roll-up using the Euler integration formula with time step $0.0005\ \frac{a}{V}$ but still only twenty mesh points. The spiral appears to unroll! A simple explanation reveals a restriction on the time step

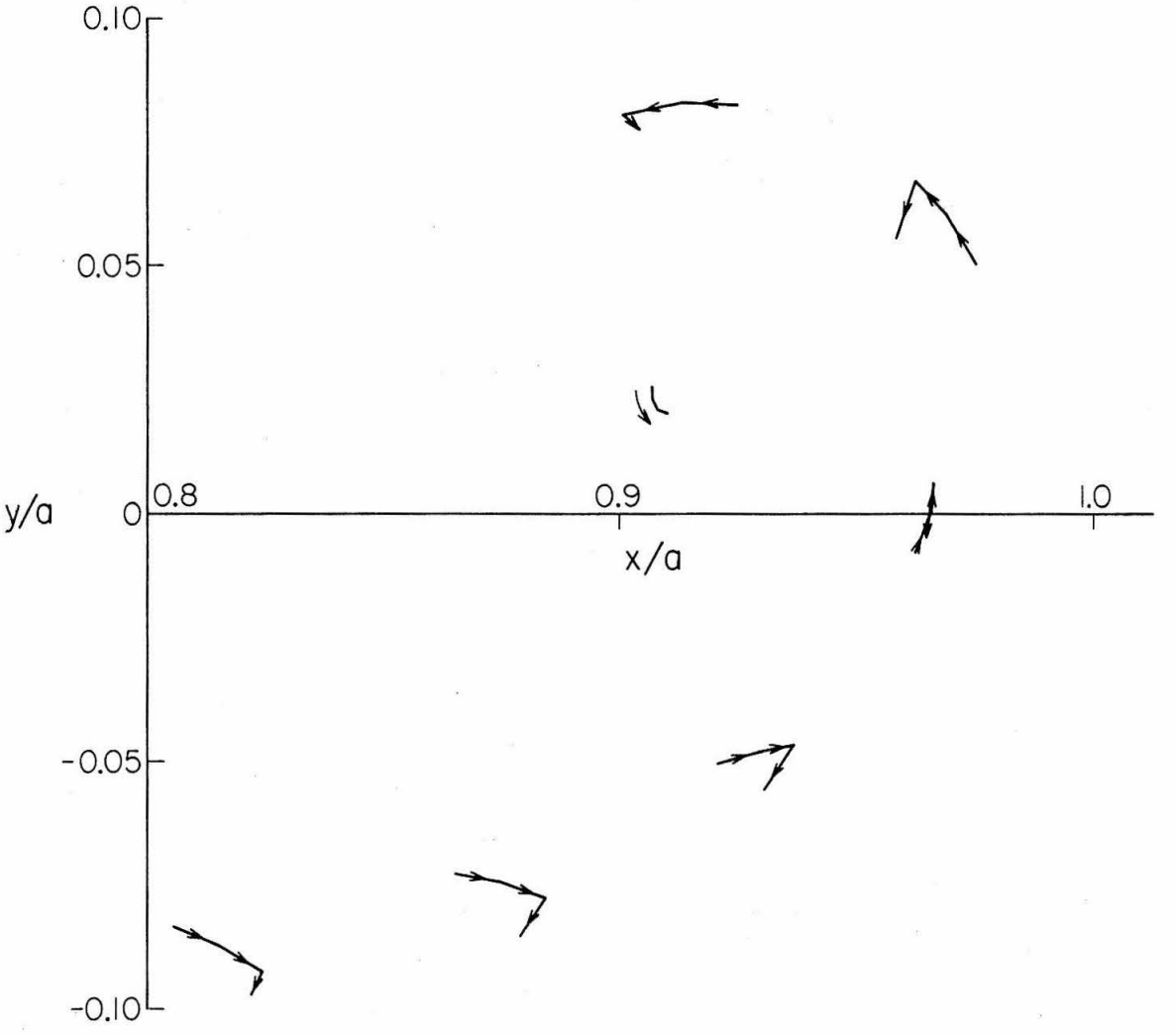

The position of the vortex points at $vt/a = 0.10, 0.11, 0.12, 0.13$.
The arrow indicates the displacement of the vortex points forward in time.

Figure 2.6

compared to the spacing between mesh points and the curvature of the sheet. Figure 2.7 illustrates the idea. If the motion of a mesh point is much smaller than its "motion" due to redistribution, then the resultant evolution does not represent the solution required. It is clear and has been confirmed that increasing the resolution of the sheet by increasing the number of mesh points will influence this effect. For forty points and the same time step, the spiral has more terms and now the unwinding occurs only in the central turn where again the number of points is too small to resolve the curvature very accurately. Thus, depending on the curvature and the actual motion, the time step cannot be smaller than some critical value related to the spacing. This behaviour is confirmed by finding that a time step of $0.0025\frac{a}{V}$ produces the unwinding of the spiral when using modified Euler integration. This also appears to be the likely explanation for the behaviour reported by Fink and Soh (1974) when applying their method to the Kelvin-Helmholtz instability (see their Figure 10).

A far better test of the method is presented by following the motion of the vortex sheet generated by a ring wing. Experimental data has recently been obtained by Bofah (1975). The vortex sheet lies on a closed curve and as discussed in Section II, the velocity calculation can be done accurately, i.e. $O(h^3)$. The ring wing generates a vortex sheet which is initially circular with radius that of

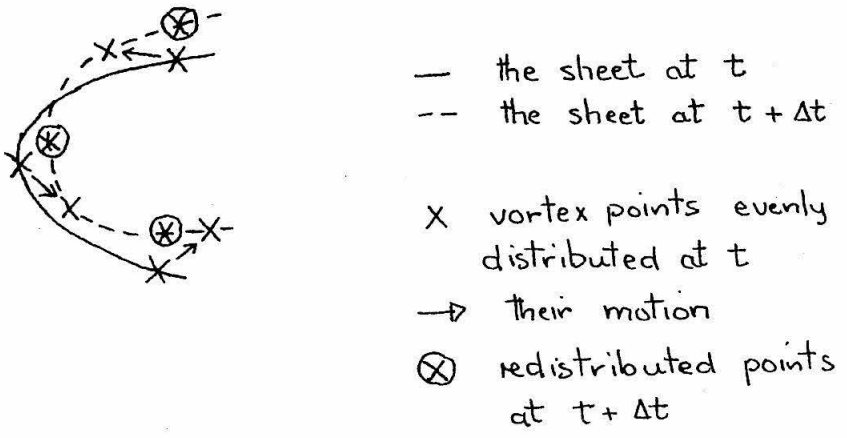

The unwinding of the vortex sheet

Figure 2.7

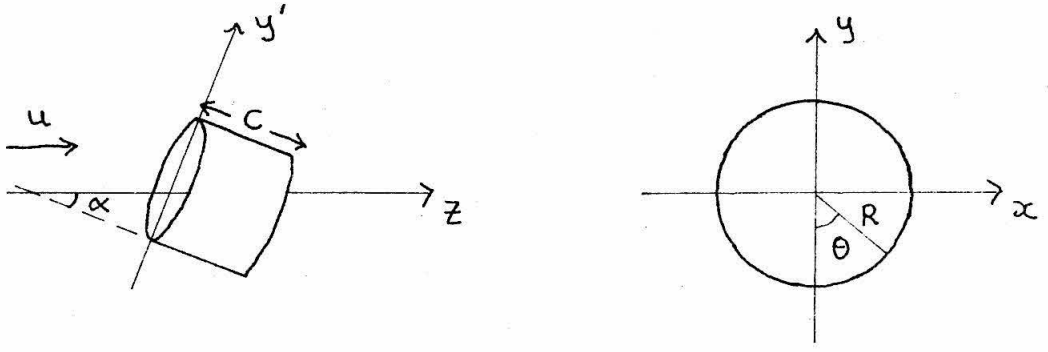

The coordinate system and parameters for the ring wing

Figure 2.8

the wing, R say, and whose strength is given by

$$\gamma(\theta) = \frac{\Gamma_0}{R} \sin\theta \qquad (2.42)$$

The definition of θ and the flow parameters are shown in Figure 2.8. Γ_0 is the root circulation and is given by

$$\Gamma_0 = \frac{\pi U \alpha C}{1 + \pi C/4R} \qquad (2.43)$$

It is convenient to non-dimensionalise the problem as follows. The vorticity strength is scaled by Γ_0/R, distances by R, time by R^2/Γ_0 and velocities by Γ_0/R.

The basic numerical approach fails to produce good results. Although all the improvements mentioned in Section III were tried, namely the calculation of arclength instead of chordlength, interpolation using spline functions and time intergration by modified Euler, there were always unphysical oscillations appearing in the results, i.e. γ becomes negative. Figures 2.9-11 show the vortex sheet at $t = 1.55 R^2/\Gamma_0$ with N the number of mesh points, increasing from 40, 60 through to 90. The corresponding profiles of the circulation measured along the sheet from $\theta = 0$ as functions of the arclength show, in Figure 2.12, the oscillatory behaviour. Bearing in mind there is an increase in arclength with increasing N, one finds that the instability occurs in the same place, the upper branch of the spiral. The crossing

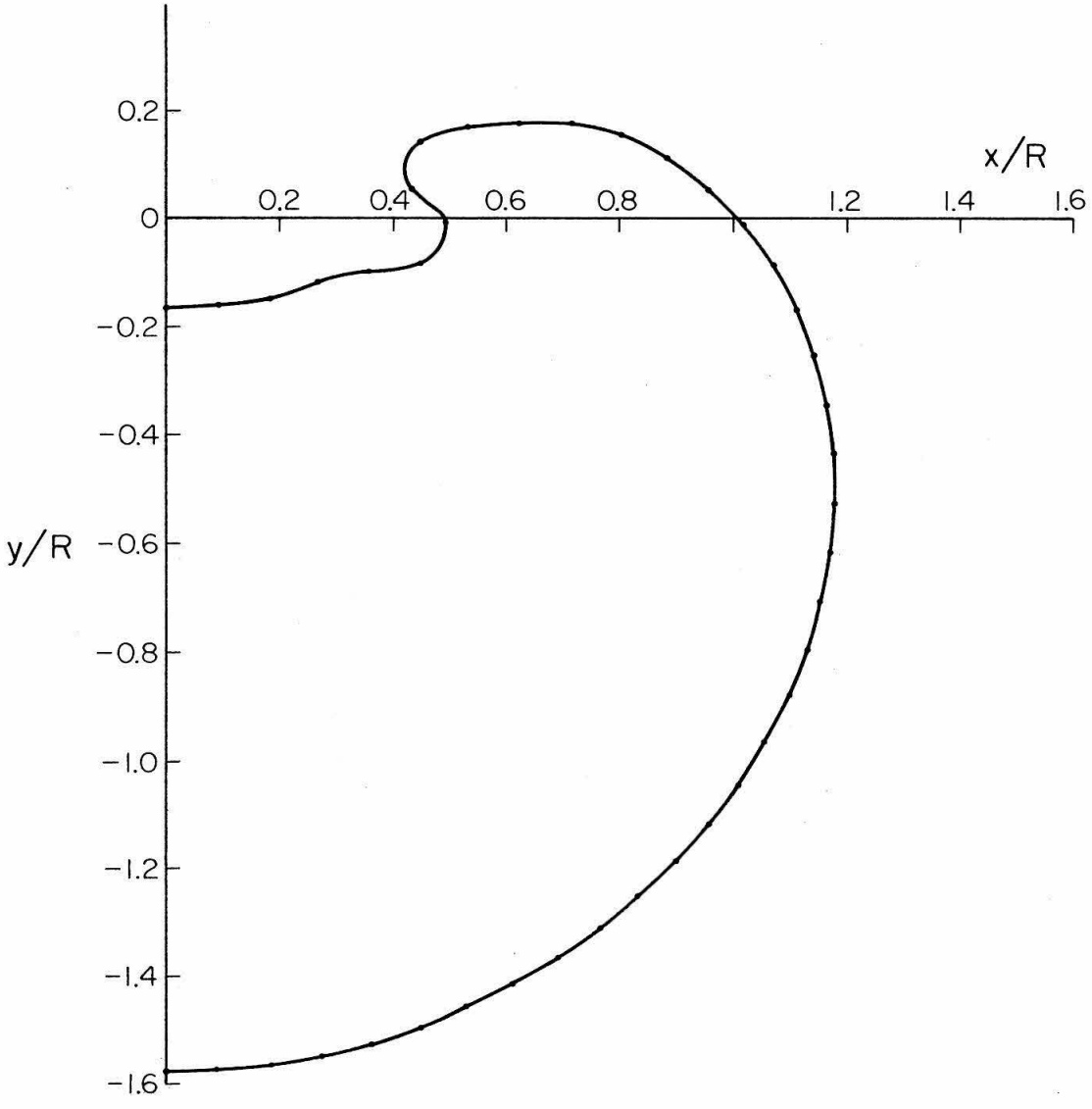

**The vortex sheet behind a ring wing at
The number of vortex points is 40.**

Figure 2.9

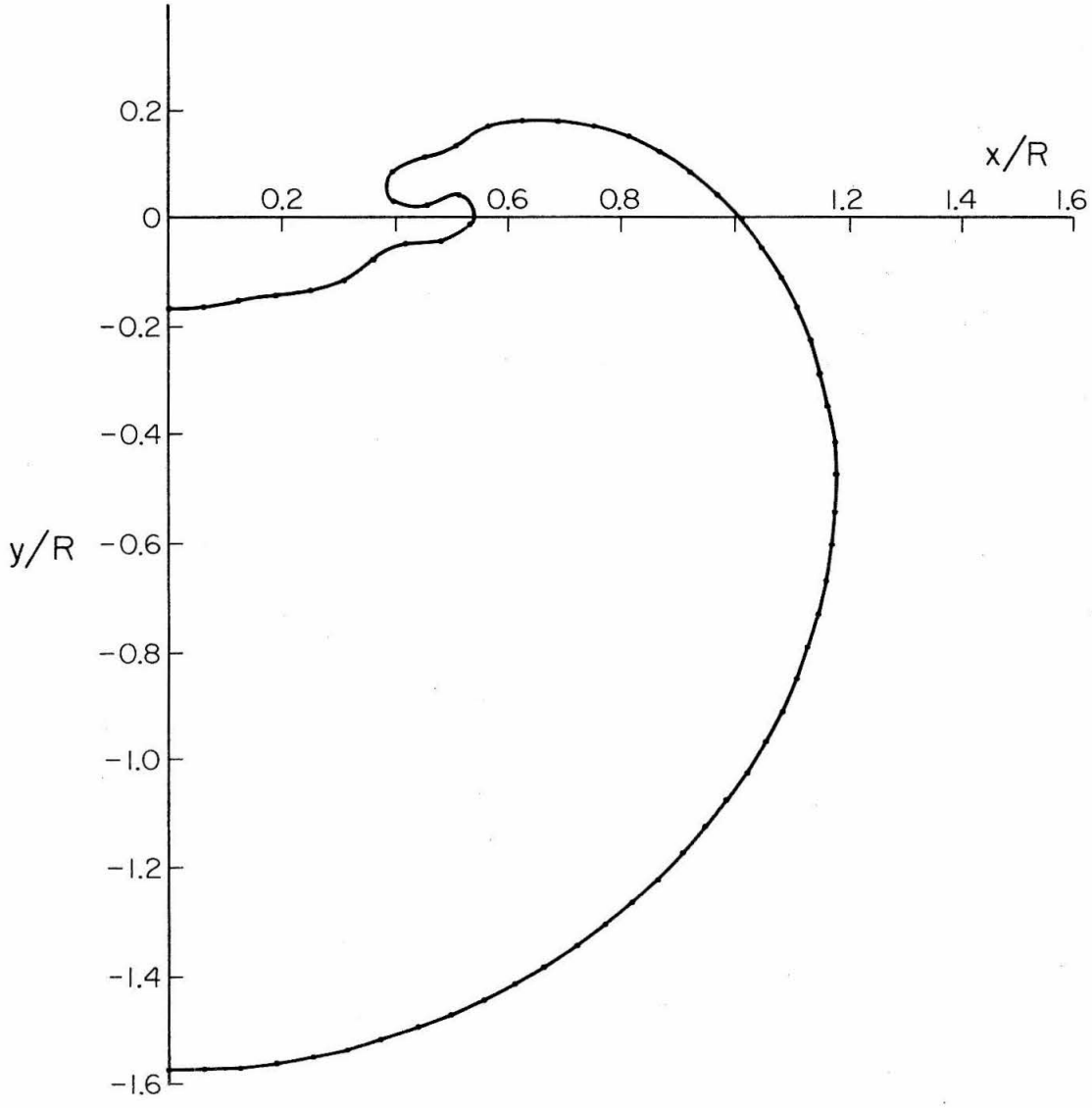

**The vortex sheet behind a ring wing at
The number of vortex points is 60.**

Figure 2.10

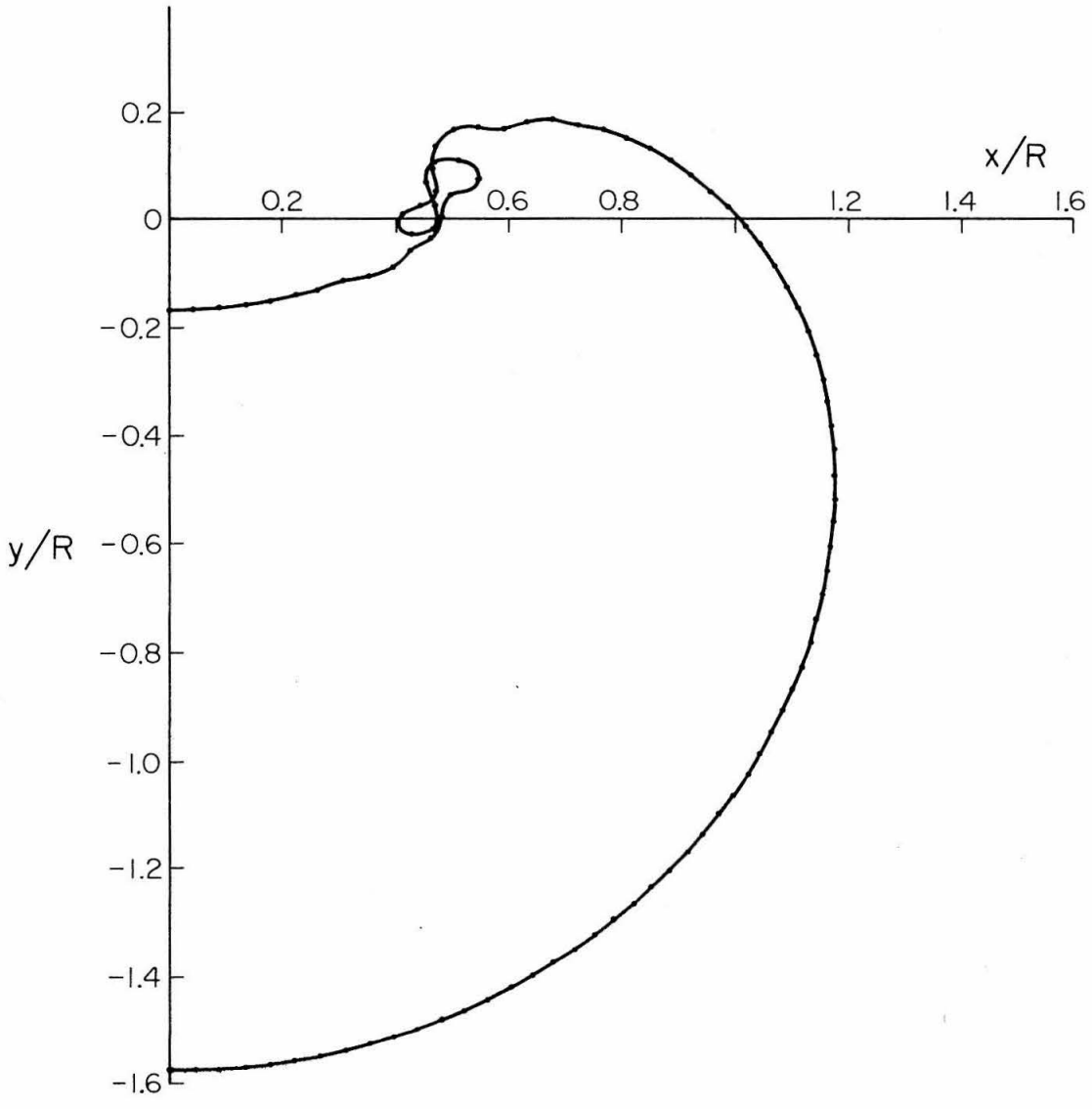

**The vortex sheet behind a ring wing at
The number of vortex points is 90.**

Figure 2.11

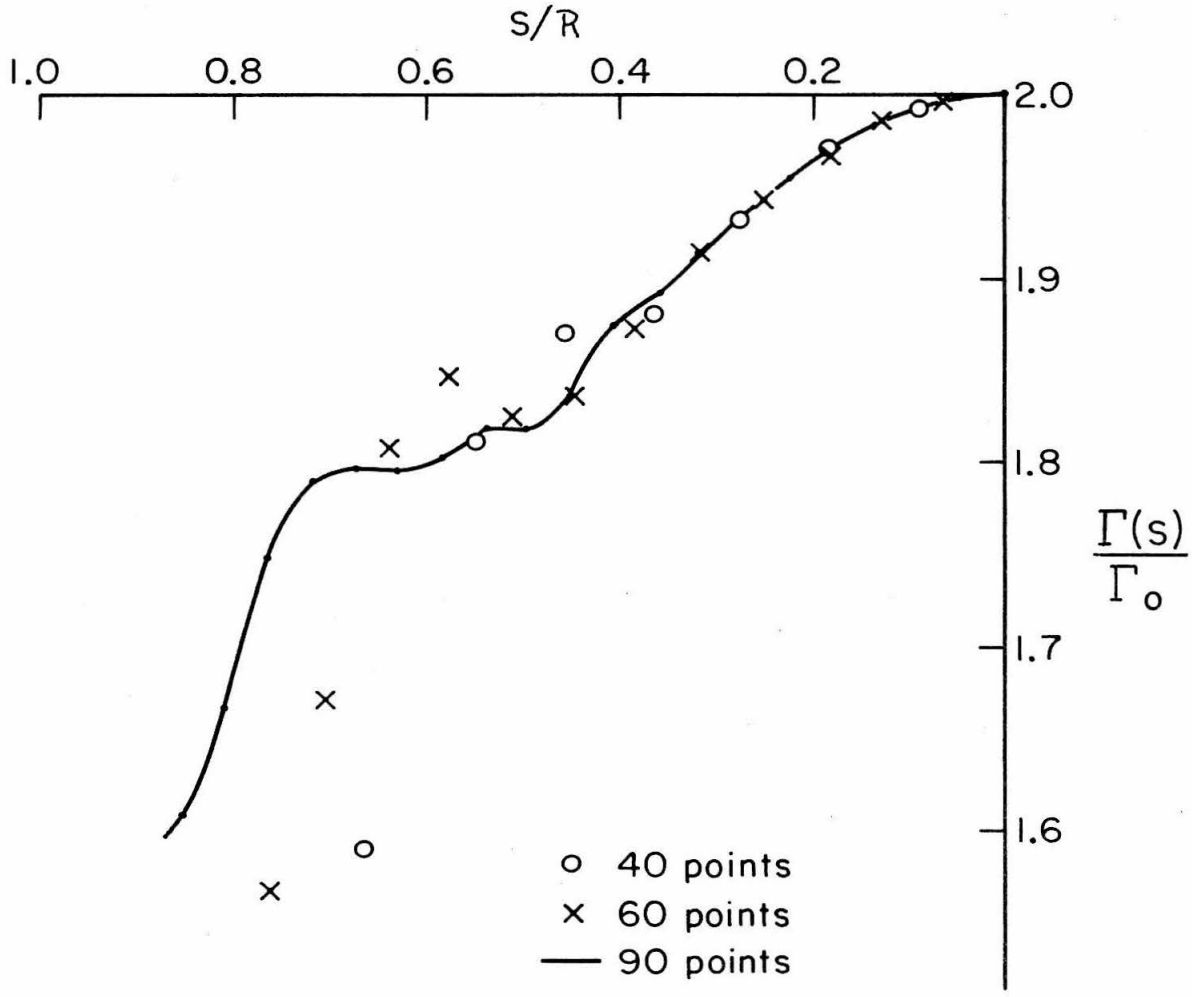

The circulation $\Gamma(s)$ along the sheet as a function of arclength s measured from the top stagnation point, for different numbers of vortex points.

Figure 2.12

of the sheet in Figure 2.11 is probably due to the inaccuracy in calculating the velocity when two separate parts of the sheet approach each other closely. To avoid this it is necessary to refine the description of the sheets locally by temporarily introducing more mesh points, e.g. see Maskew (to be published). With increasing N, the accuracy of the invariants, circulation for half the ring wing and the vertical impulse, improve and their values remain in very narrow bounds.

In an attempt to determine what causes this numerical breakdown, different ways of implementing the method are tried. For interpolation, both spline functions and Lagrangian interpolation give basically the same results. Using chordlength or the more accurate arclength makes no difference. The accuracy of the velocity calculation is improved to $O(h^5)$ but this does not indicate that curvature effects are destroying the accuracy in determining the velocity. Even an alternative method in reassigning the vortex sheet strength to the new mesh points during the redistribution process is tried. As the points move their vortex sheet strength changes as $\gamma^* = \gamma \frac{ds}{ds^*}$ where s^* is their new arclength value. It is then easy to interpolate to find the values of vortex sheet strength at evenly spaced mesh points. Since the oscillatory behaviour occurs in the region of maximum γ it was thought that the interpolation formulae when being applied to reassigning the circulation, may

develop large errors due to the large value of the slope of the circulation, i.e. γ . This alternative method, however, should always have $\frac{ds}{ds^*}$ close to 1 and so this aspect would be circumvented. However, there is no improvement in the result.

Finally, as a check on the means of redistribution to see whether it is associated with numerical **instability, a** simple one-dimensional problem is tried.

$$\frac{d\Gamma}{dt} = 0 \tag{2.44}$$

along the characteristics,

$$\frac{ds}{dt} = \frac{d\Gamma}{ds} \tag{2.45}$$

with the initial condition,

$$\Gamma(s) = 1 - \cos s \tag{2.46}$$

This problem is equivalent to solving

$$\frac{\partial\Gamma}{\partial t} + \left(\frac{\partial\Gamma}{\partial s}\right)^2 = 0 \tag{2.47}$$

and has the solution in parametric form

$$\gamma = \frac{\partial\Gamma}{\partial s} = \sin\xi \quad , \quad s = 2\sin\xi . t + \xi \tag{2.48}$$

The solution becomes multivalued at $S=\pi$ when $t=\frac{1}{2}$ but until then, applying the method of redistribution results in an accurate numerical solution with no instability. Of course this is only a one-dimensional analogue and so curvature effects are ignored but it does give some reason to believe that the redistribution is basically sound.

Often, numerical instabilities can be suppressed by appropriate smoothing. Provided the smoothing affects only the oscillations which are spurious, the accuracy will not be impaired. Unfortunately in this case it is difficult to find a means of suppressing the oscillations associated with the instability and leave the basic solution unchanged. The profile of the circulation is smoothed by applying a difference formula corresponding to the standard diffusion equation. This should suppress only high frequency components in the profile provided the diffusion time step is much smaller than the actual time step. The difference formula is

$$u_i^* = u_i + \varepsilon(u_{i+1} - 2u_i + u_{i-1}) \qquad (2.49)$$

where the superscript * indicates the smoothed values and the subscripts refer to the discretised arclength position.

Although it is easy to estimate the comparison between the two different time steps, it is simpler to compare the results obtained when ε has the minimum value

which suppresses the oscillatory behaviour and when ε has a value which only just permits oscillations. This comparison is shown in Figures (2.13) and (2.14) where $\varepsilon = 0.1$ and 0.01 respectively. Smoothing clearly destroys the details of the spiral and so is useless as a means of continuing the calculation of the roll-up.

In conclusion, calculating the evolution of a vortex sheet by redistributing mesh points fails to provide a reliable method despite the fact that this method no longer regards the sheet as collection of discrete vortices but takes into account its curvature, and so is a more appropriate physical description. Even though the discretisation errors in the approximations decrease as the number of mesh points increases, the position of the vortex sheet for a time level greater than $1.5\,R^2/\Gamma_0$ does not appear to approach a limit. This suggests the original problem may be ill posed, perhaps due to the basic instability of the vortex sheet to small wavelength disturbances. To fully explore this idea, it would be necessary to introduce many more mesh points and the method becomes uneconomical. The operation count for calculating the velocity is $O(N^2)$.

Finally, it is important to remember that the limit of small viscosity may not correspond to inviscid flow and so it may be more appropriate to look for methods which take into account some small viscous effects. Since viscosity damps the growth of small scales, it is obviously important

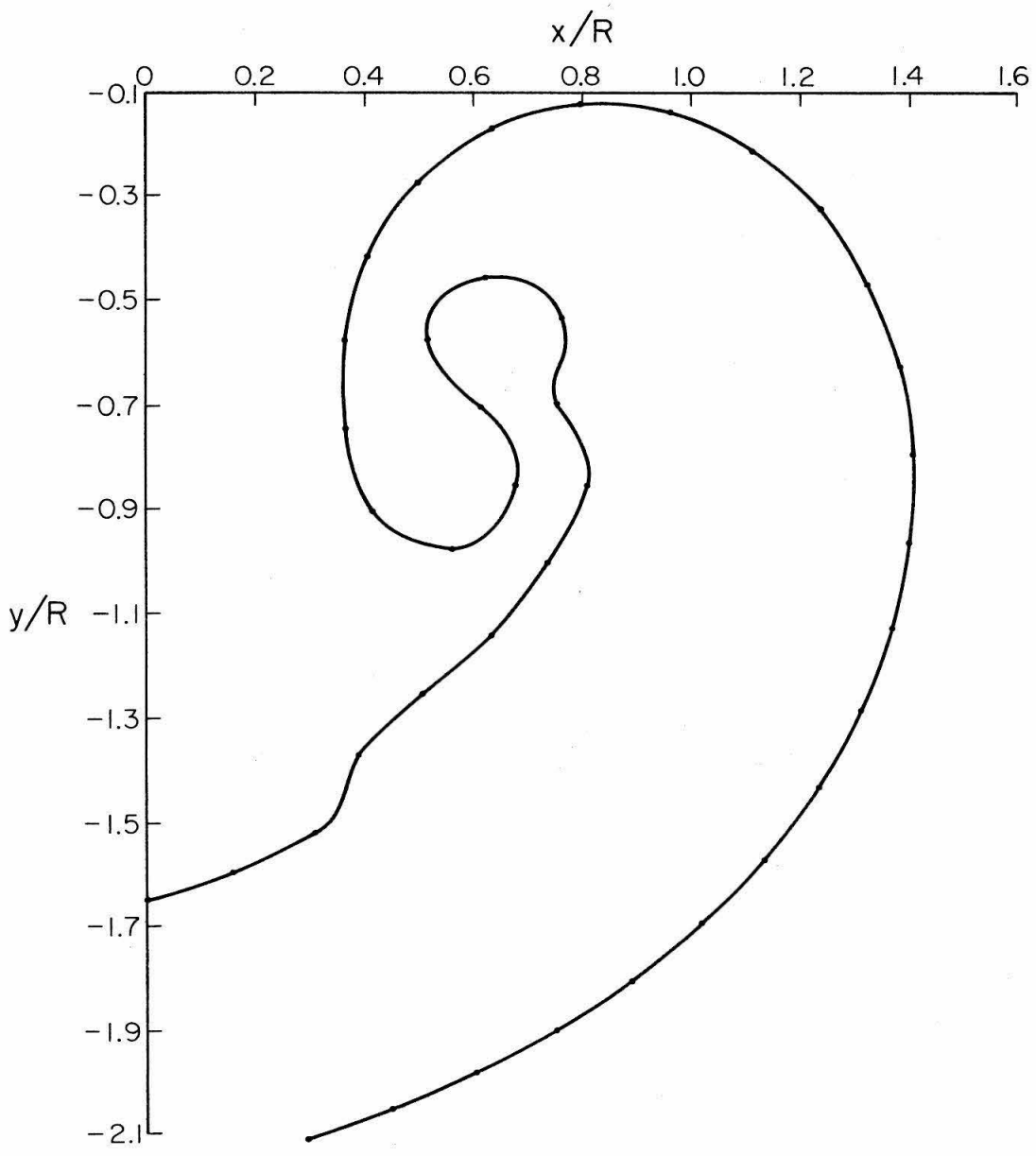

The roll-up of the vortex sheet behind a ring wing at $t = 3.87588\ R^2/\Gamma_0$. Smoothing parameter, $\varepsilon = 0.1$

Figure 2.13

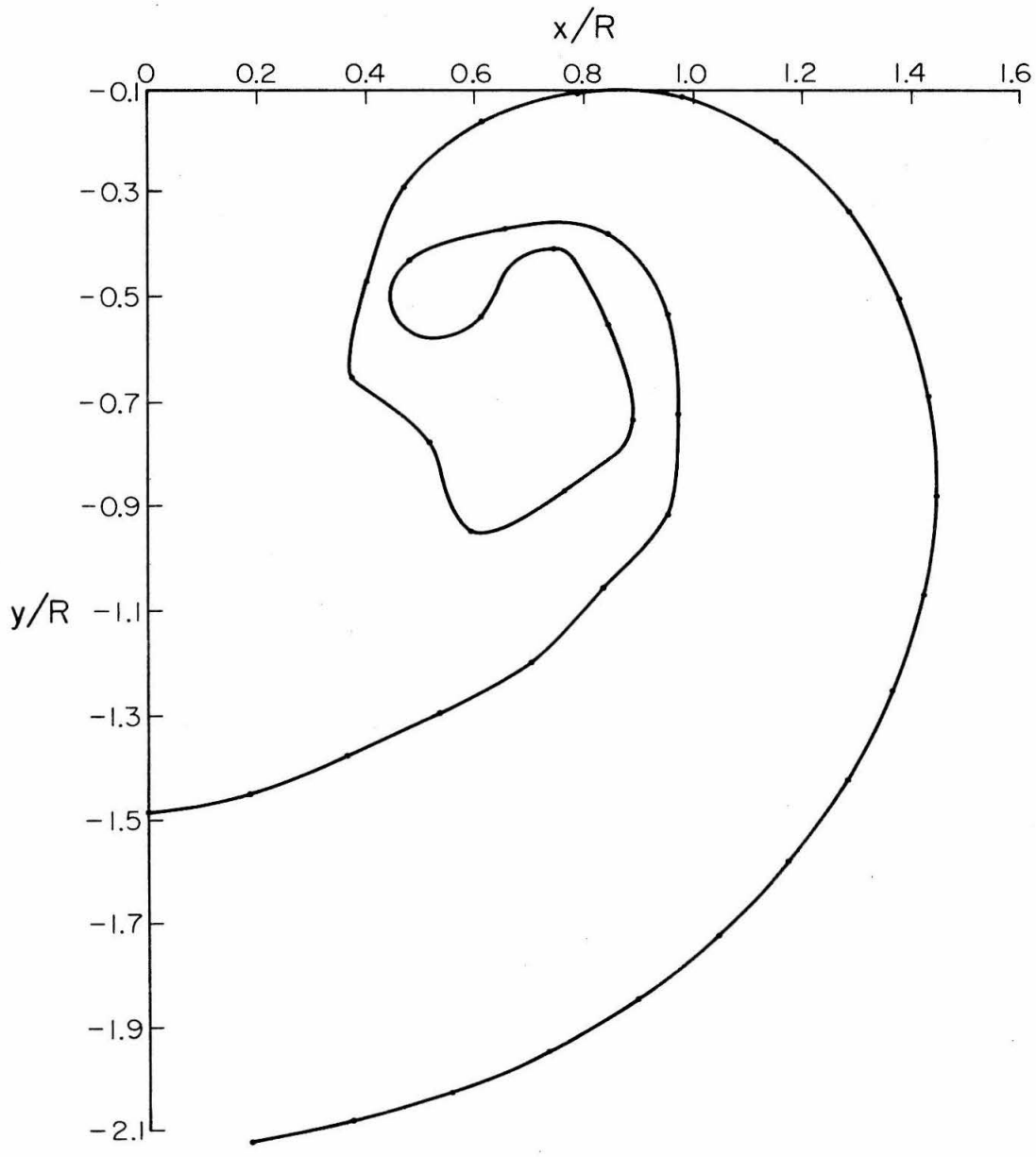

The roll-up of the vortex sheet behind a ring wing at $t = 3.87588\ R^2/\Gamma_0$ **. Smoothing parameter,** $\varepsilon = 0.01$

Figure 2.14

in the question of the stability of the sheet.

V. A METHOD BASED ON THE CIC TECHNIQUE

From the conclusion of the previous section, a method is needed which can calculate the velocity of a large number of point vortices. The most sensible method is one based on the CIC Technique. It seems appropriate to give the details before discussing the many facets of the method.

For an incompressible, two-dimensional fluid with velocity, $\vec{u} = (u_x, u_y, 0)$, and vorticity, $\vec{\omega} = (0, 0, \omega)$,

$$\nabla \cdot \vec{u} = 0 \quad ; \quad u_x = \frac{\partial \psi}{\partial y} \quad , \quad u_y = -\frac{\partial \psi}{\partial x} \tag{2.50}$$

where ψ is the streamfunction.

$$\omega = \frac{\partial u_y}{\partial x} - \frac{\partial u_x}{\partial y} . \tag{2.51}$$

The momentum equation can be written for an inviscid fluid as

$$\frac{\partial \omega}{\partial t} + \vec{u} \cdot \nabla \omega = 0 . \tag{2.52}$$

From (2.50) and (2.51),

$$\nabla^2 \psi = -\omega . \tag{2.53}$$

Since the vorticity moves with the fluid, vortex points, resulting from a discretisation of the vorticity,

$$\omega = \sum_{n=1}^{N_v} \omega_n \, \delta(x-x_n) \, \delta(y-y_n) \qquad (2.54)$$

follow the paths

$$\frac{dx_n}{dt} = \left.\frac{\partial \psi}{\partial y}\right|_n \quad , \quad \frac{dy_n}{dt} = -\left.\frac{\partial \psi}{\partial x}\right|_n \qquad (2.55)$$

To solve (2.53), a rectangular grid is introduced which covers the region of interest. If h_x , h_y are the dimensions of one cell of the grid, then a finite difference approximation to (2.53) is

$$\frac{\psi(i,j+1) - 2\psi(i,j) + \psi(i,j-1)}{h_y^2} + \frac{\psi(i+1,j) - 2\psi(i,j) + \psi(i-1,j)}{h_x^2}$$

$$= -\omega(i,j) \qquad (2.56)$$

where $i=1,2,\ldots,N+1$, $j=1,2,\ldots M+1$, $Nh_x = L_x, Mh_y = L_y$ (L_x, L_y are the dimensions of the rectangular grid). Doing one step of cyclic reduction on the system (2.56), one finds the coefficients of $\psi(i,j)$, $i=1,2,\ldots N+1$, are symmetrical and a **fast** sine transform enables the Fourier coefficients of the solution to be found (see Hockney (1970) for details). After returning to physical space, one reverse iteration of the cyclic reduction gives the full solution. In order for this scheme to work, Dirichlet conditions must be given at the boundary.

Since the error of the method will be related to the grid spacing and the larger the grid the more expensive the computation, it is important to optimise the size of the rectangular grid around the flow of interest. To find the value of ψ on the boundary, local vorticity centroids are found as follows.

$$\bar{x}_i = \sum_{j=(i-1)k+1}^{ik} (x_j w_j)/\bar{w}_i \qquad (2.57)$$

$$\bar{y}_i = \sum_{j=(i-1)k+1}^{ik} (y_j w_j)/\bar{w}_i \qquad (2.58)$$

$$\bar{w}_i = \sum_{j=(i-1)k+1}^{ik} (w_j) \qquad (2.59)$$

where $i = 1, 2, \ldots L$, $Lk = N_v$. Using the flow field of these L point vortices, the velocity can be approximated at the boundary of the rectangular grid. To be sure this approximation is accurate enough, the boundary is chosen to be at least a distance H away from any centroid vortex, where $H = \max_{i,j} |\bar{r}_i - \bar{r}_j|$ (see Maskew (to be published)). To obtain the Dirichlet condition, the appropriate velocity component can be integrated to give the streamfunction along the boundary. Since the streamfunction is single-valued, it must approach the same value after one complete integration around the boundary and this provides a useful check on accuracy. In practice, it may prove too expensive to determine the velocity at each grid point on the boundary in this

manner. One way to avoid this difficulty is to determine the velocity at fewer boundary points and use an interpolation formula for the rest of the points.

Once the streamfunction is known, the velocity components at the grid points can be easily obtained.

$$u_x(i,j) = \frac{\psi(i,j+1) - \psi(i,j-1)}{2h_y} \tag{2.60}$$

$$u_y(i,j) = -\frac{\psi(i+1,j) - \psi(i-1,j)}{2h_x} \tag{2.61}$$

Since the velocity components are known at the boundary, the velocity is known everywhere on the grid.

However, the vorticity is not known at the grid points and the velocity is needed at the points (x_n, y_n), (see (2.55)). Following the usual CIC method (see Christiansen (1973)), the vorticity at each point (x_n, y_n) is shared by the four corner grid points of the cell in which it is located by the following weighted scheme (known sometimes as an area-weighting technique), illustrated in Figure 2.15.

$$w(i,j) = A_2 w_n / h_x h_y \qquad w(i+1,j) = A_1 w_n / h_x h_y$$

$$w(i,j+1) = A_4 w_n / h_x h_y \qquad w(i+1,j+1) = A_3 w_n / h_x h_y \tag{2.62}$$

where A_i is an area as shown. This particular weighting ensures the conservation of circulation and linear momentum.

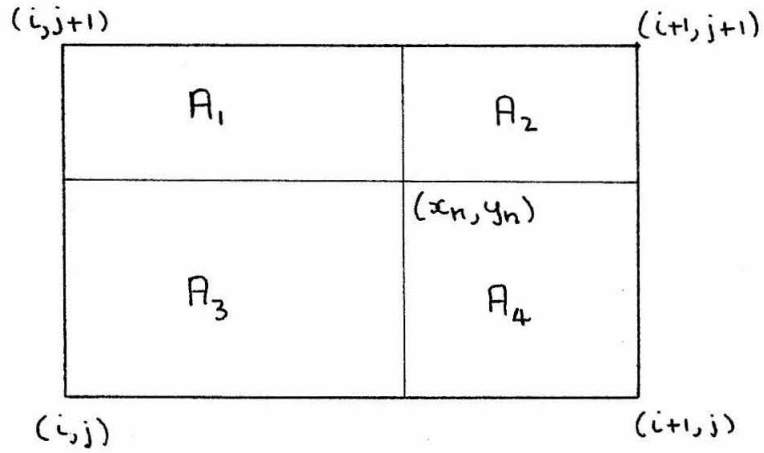

The areas in a typical cell.

Figure 2.15

To find the velocity at the vortex points, a bilinear interpolation is used.

$$\vec{u}(x_n, y_n) = \Big[A_2 \vec{u}(i,j) + A_1 \vec{u}(i+1,j) + A_4 \vec{u}(i,j+1) + A_3 \vec{u}(i+1, j+1) \Big] / h_x h_y \qquad (2.63)$$

Finally, the time integration of (2.55) is achieved by using a simple Euler difference approximation. A check on this approximation by using a leap-frog scheme showed no qualitative change in the results. The criterion used to choose the time step is that no vortex point moves more than a grid spacing in one step.

The method for calculating the velocity (i.e. (2.56), (2.60), (2.61) and (2.63)) has its largest error associated with the bilinear interpolation used in (2.63). This is seen in the test case of a single vortex. The flow calculated deviates from the exact flow in the neighbourhood of the vortex (about a grid spacing) but this is not the region of interest. The object of the method is not to calculate the flow field of a collection of point vortices but of a vortex sheet (or perhaps better, of a narrow region of concentrated vorticity). The vortex points used are assigned the role of markers to follow the evolution of the vorticity. Christiansen (1973) also reports the bilinear interpolation to be the most important factor in producing numerical errors.

Improved interpolation schemes can be found but it is hoped that since the grid is changed at every time step that this error will be randomised and lead to cancellation at successive time steps which will improve the accuracy.

With these thoughts in mind, the results of the method, when applied to the ring wing, prove interesting. Making use of the results obtained by Fink and Soh's method, a profile of the vortex sheet at a time $t = 1.1627\,T_0$, just before the onset of the numerical instability as seen in the previous section, is used as an initial condition. The CIC method then produces the most detailed roll-up the author has seen to date. This is shown in Figure 2.16 for a grid size 65 X 65 and with four-hundred vortex points. Figure 2.17 shows the calculation repeated with a time step half that used in Figure 2.16 and both figures show the result at $t = 1.9127\,T_0$. Outside of the spiral, there appear smaller structures. At first, this was considered another example of numerical instability and smoothing was introduced to see if the "instability" could be contained without destroying the details of the roll-up. The smoothing used was a (1 4 6 4 1) weighting in averaging the positions of the point vortices and the result is shown in Figure 2.18. Although the time is not the same, it is close enough to show that the smoothing works as required.

A survey of the literature fails to find any report of small scale structure of the form shown in Figures 2.16

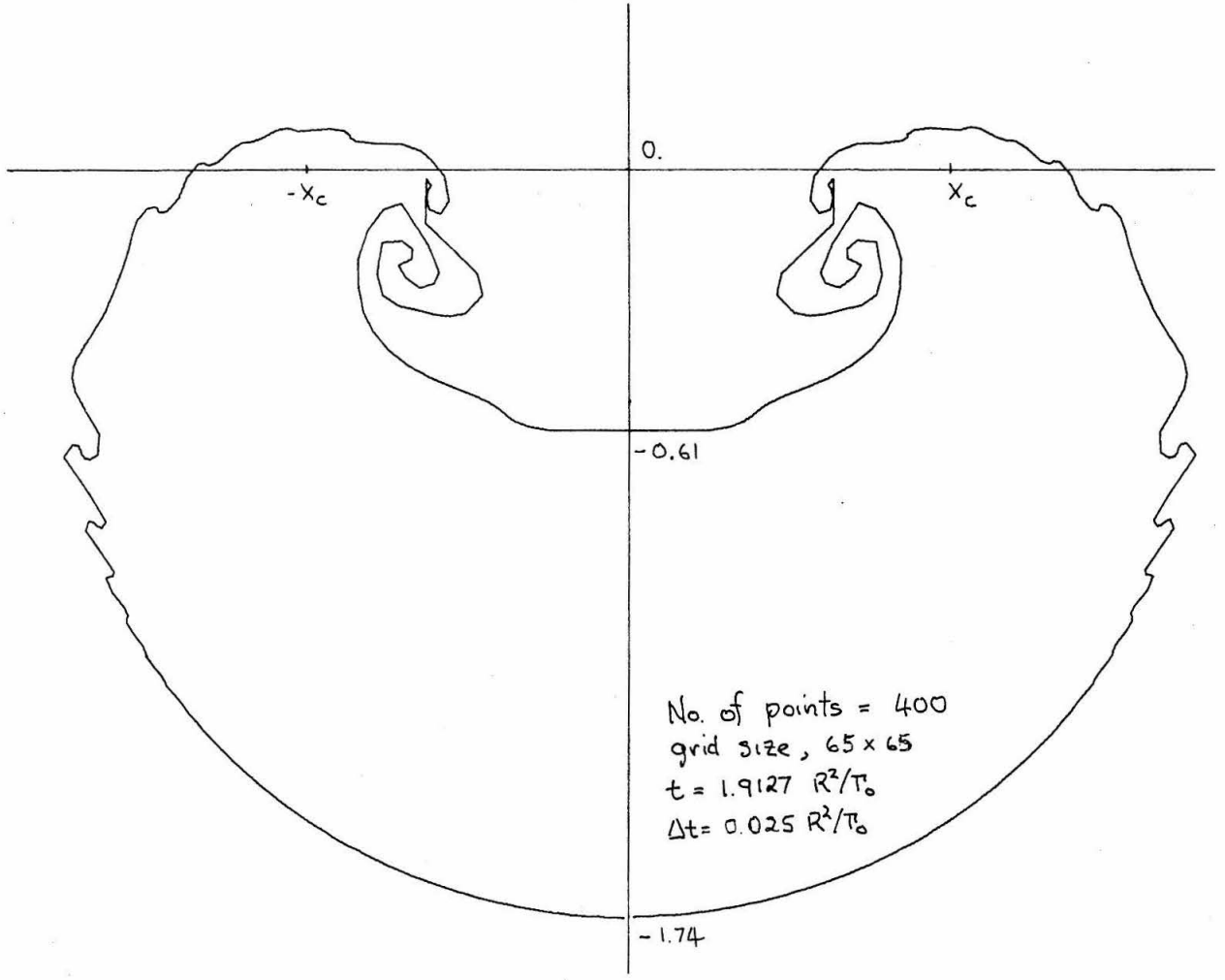

The roll-up of a vortex sheet behind a ring wing.

Figure 2.16

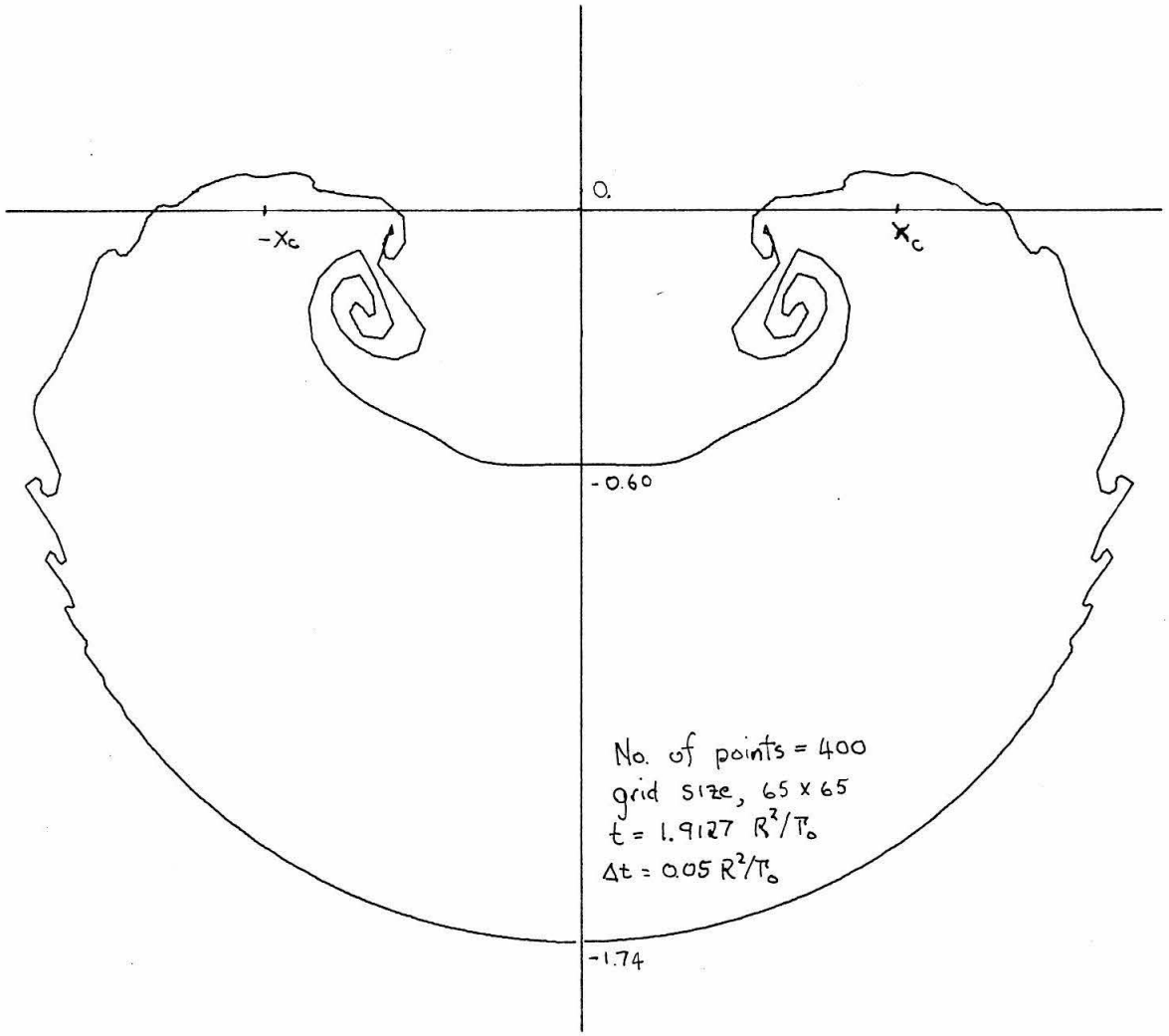

The roll-up of the vortex sheet behind a ring wing.

Figure 2.17

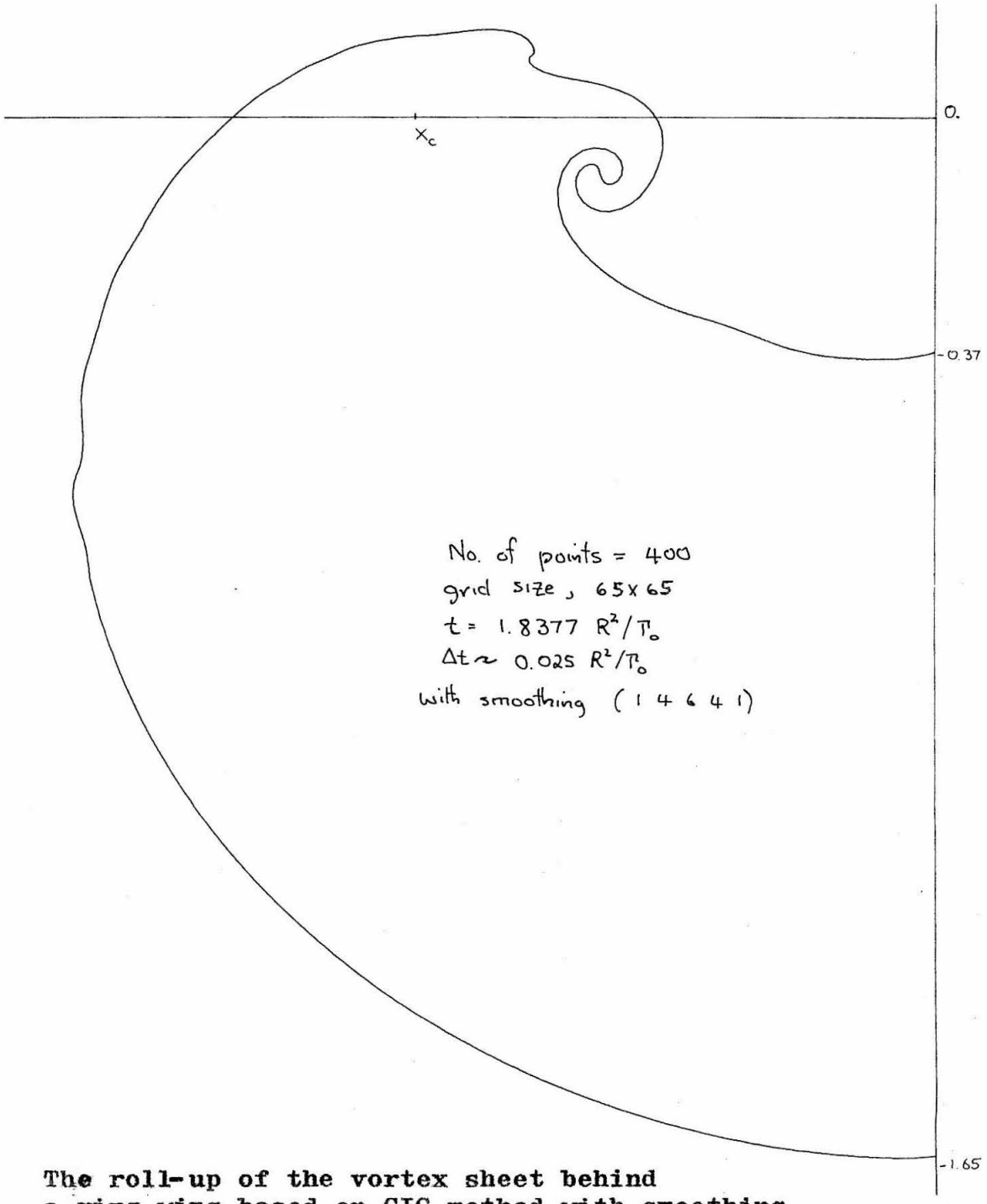

The roll-up of the vortex sheet behind a ring wing based on CIC method with smoothing.

Figure 2.18

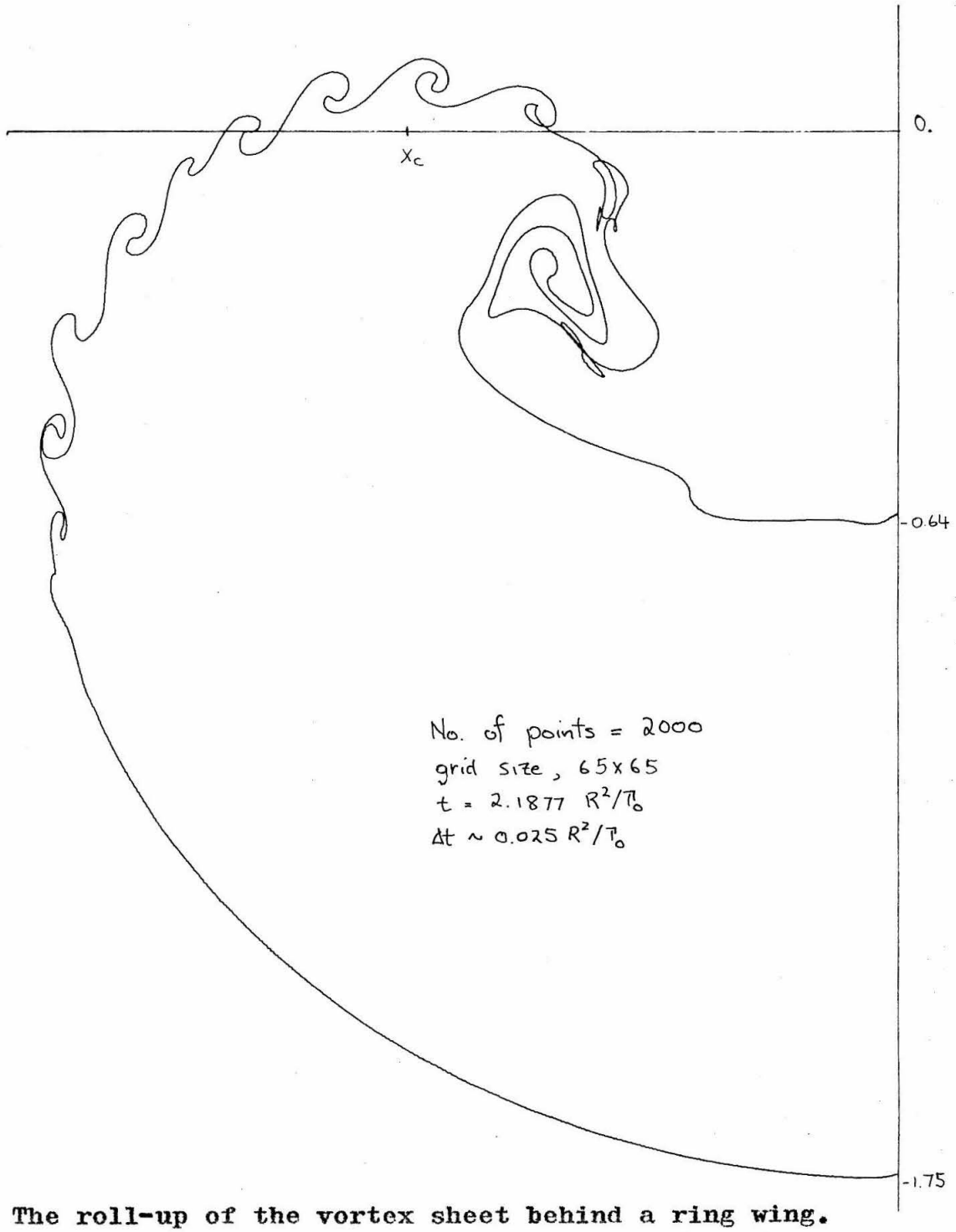

The roll-up of the vortex sheet behind a ring wing.

Figure 2.19

and 2.17 for the case of a ring wing. Pierce (1961) has taken photographs of the flow generated by the acceleration of a flat place through still air. There is evidence of smaller structures outside the main vortex core resulting from the roll-up of shed vorticity. These structures are convected into the vortex core. This behaviour is reproduced in Figure 2.19 when the number of vortex points is increased to two-thousand. Clearly the grid is too large to resolve the details of the smaller structures and so the vortex sheet loses definition in those regions. This is a definite indication that smaller structures may play a role in the development of vortex cores which result from roll-up processes.

It is instructive to examine the method when applied to a flow in which there is some known information about the growth of small scales. Moore (1974) considers the stability of an expanding circular sheet. If the position of the sheet is given by

$$r = R_0 e^{bt} + \varepsilon(t) e^{is\theta}, \qquad (2.64)$$

linear stability analysis gives

$$|\varepsilon(t)| = \frac{C I_0(\gamma e^{-2bt}) + D K_0(\gamma e^{-2bt})}{R_0 e^{bt}} \qquad (2.65)$$

where C, D are constants, R_0 is the initial radius and

$$\gamma = \frac{\Gamma (s^2 - 2s)^{1/2}}{8\pi b R_o^2} \qquad (2.66)$$

The functions I_o and K_o are of modified Bessel type. The vortex sheet has constant initial strength and Γ is the total circulation. For small times, i.e. $bt \ll 1$, the K_o term gives the growth of $|\varepsilon(t)|$.

$$|\varepsilon(t)| = |\varepsilon_o| e^{2\gamma bt} \qquad (2.67)$$

As a measure of $|\varepsilon(t)|^2$, the variance of the vortex points around a mean radius is determined and Figure 2.20 shows the logarithm of this variance as a function of time for $b = 0.1\ \Gamma/2\pi R_o^2$. Curve (b) is the result when the grid spacing is double the spacing of curve (a) and curve (c) is for the same spacing as (b) but using a time step twice as large. The curves all show the same basic trend. After the first few time steps there appears an almost linear regime before the growth begins to slow down. This slowdown in growth corresponds to the emergence of larger structures from the small scale perturbations. The behaviour of the slope of the logarithm of the variance is consistent with (2.67) when the limiting wave number, S, is based on the grid spacing. If the bilinear interpolation in (2.63) is the major source of error, then this explains why the dominant S is the one based on grid spacing. The curves in Figure

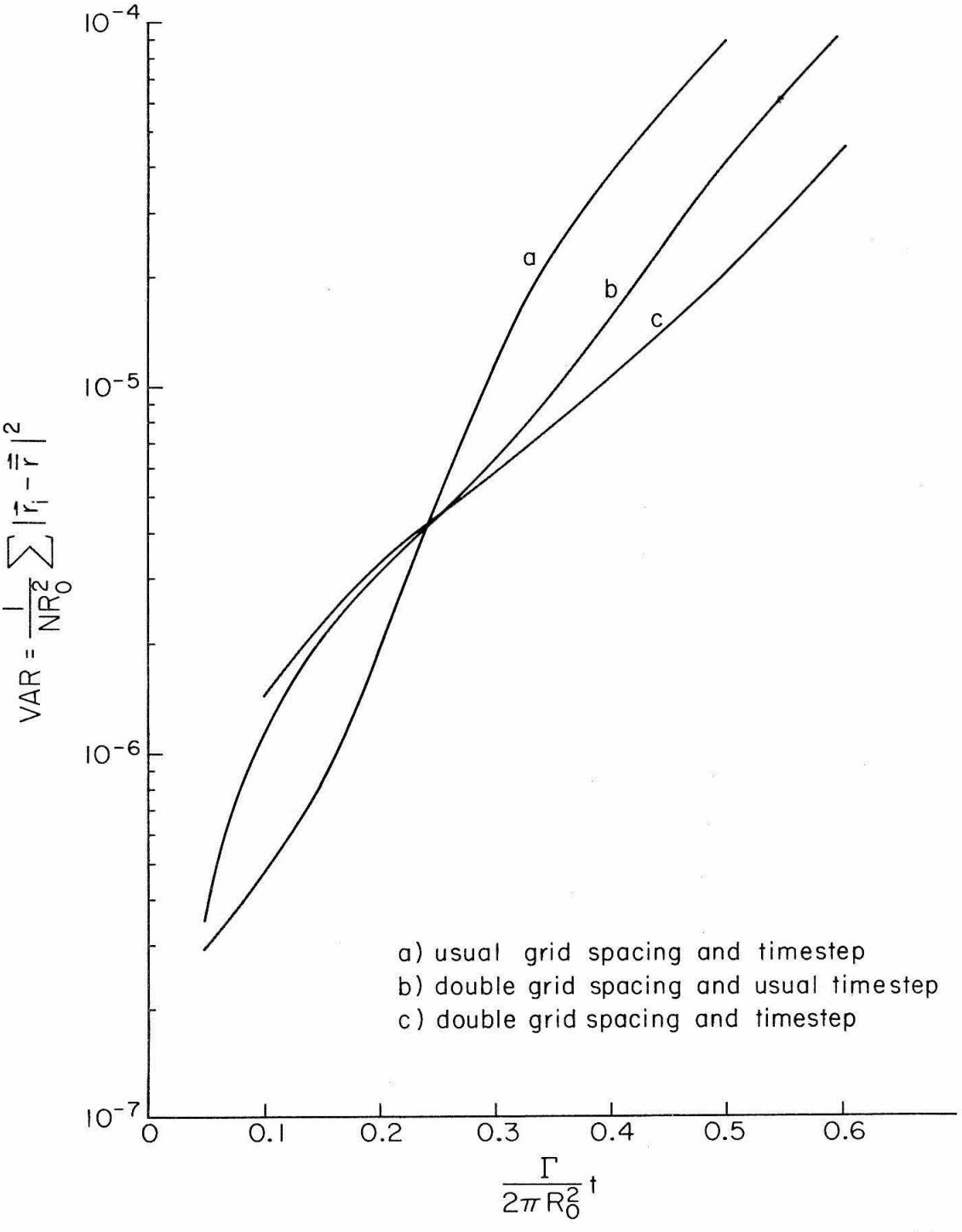

The variance of vortex points around a mean radius as a function of time.

Figure 2.20

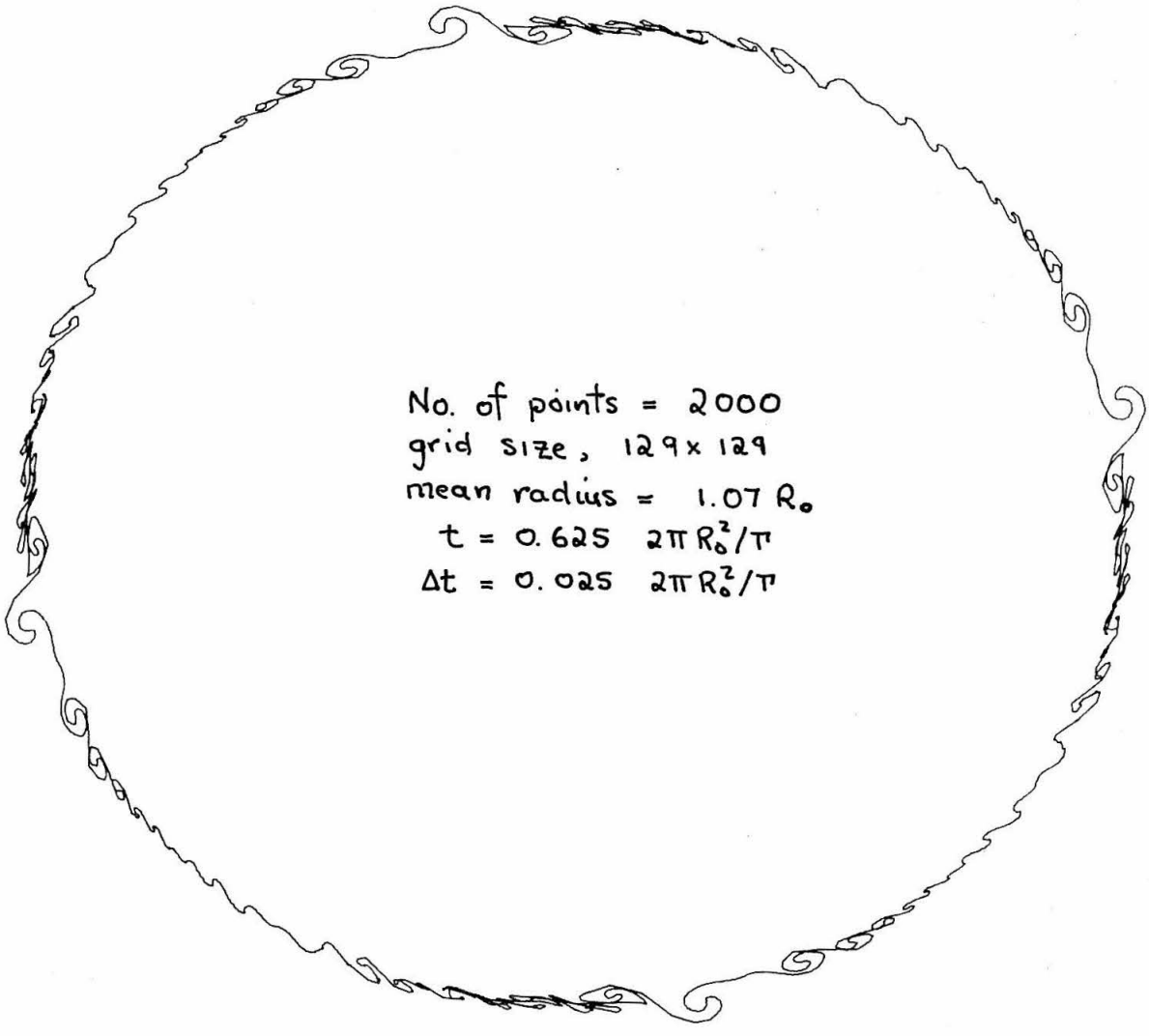

The expanding circular vortex sheet.

Figure 2.21

2.20 are obtained with two-thousand vortex points and a grid, 129 X 129. There is no difference when one-thousand vortex points are used, so the spacing between vortex points is less important than the grid spacing. In passing, it should be noted that the viscous spreading of the sheet was calculated but the resulting variance does not have the behaviour found.

Figure 2.21 gives the vortex sheet at $t = 0.625\, 2\pi R_o^2/\Gamma$. It shows that some small structures are interacting and bigger structures are forming. The details of the small structures are not always clear due to lack of resolution by the method. The largest spirals appear to form where the length of the sheet per cell is typically smallest over a number of cells. There is a common symmetry to both the circular sheet and rectangular grid, viz angular modes with frequency $4m$, m an integer, and this is clearly visible in the results for $m=1$ at least. This was reported by Christiansen (1973) as an **anomalous** instability.

The most important aspect of the result, however, is that the emerging larger structures seem to be independent of the method. Although grid size, number of vortex points, and time step were all varied, the size of the structures remains the same and take the same form. Decreasing the grid size and increasing the number of vortex points only increases the details of the structure. This is a great positive aspect of the method and suggests that provided

small scales are appropriately allowed for in the method, consistent results appear to emerge.

To illustrate further the potential of this approach, Figures **2.22a-n** show the time evolution of the ring wing. Two-thousand vortices are used on a grid, 128 X 128. Once again small structures appear early but now their transition to larger structures is clear. Moreover, amalgamation of vortex structures is seen as well as a structure disintegrating and being absorbed into neighbouring structures. This is very promising in the light of some recent experimental work, viz Freymuth (1966), **Winant** and Brownand (1974) and Brown and Roshko (1974) all report seeing amalgamation and disintegration processes.

One disadvantage is the loss of definition of the sheet and it is not clear at this point whether this can be related to an effective viscosity introduced by the scheme. Since there is great interest in understanding vortex pairing theoretically, (e.g. Christiansen and Zabusky (1973), Patnaik, Sherman and Corcos (1976)), this method holds interesting possibilities especially when it is remembered that increasing the number of vortex points adds relative little cost.

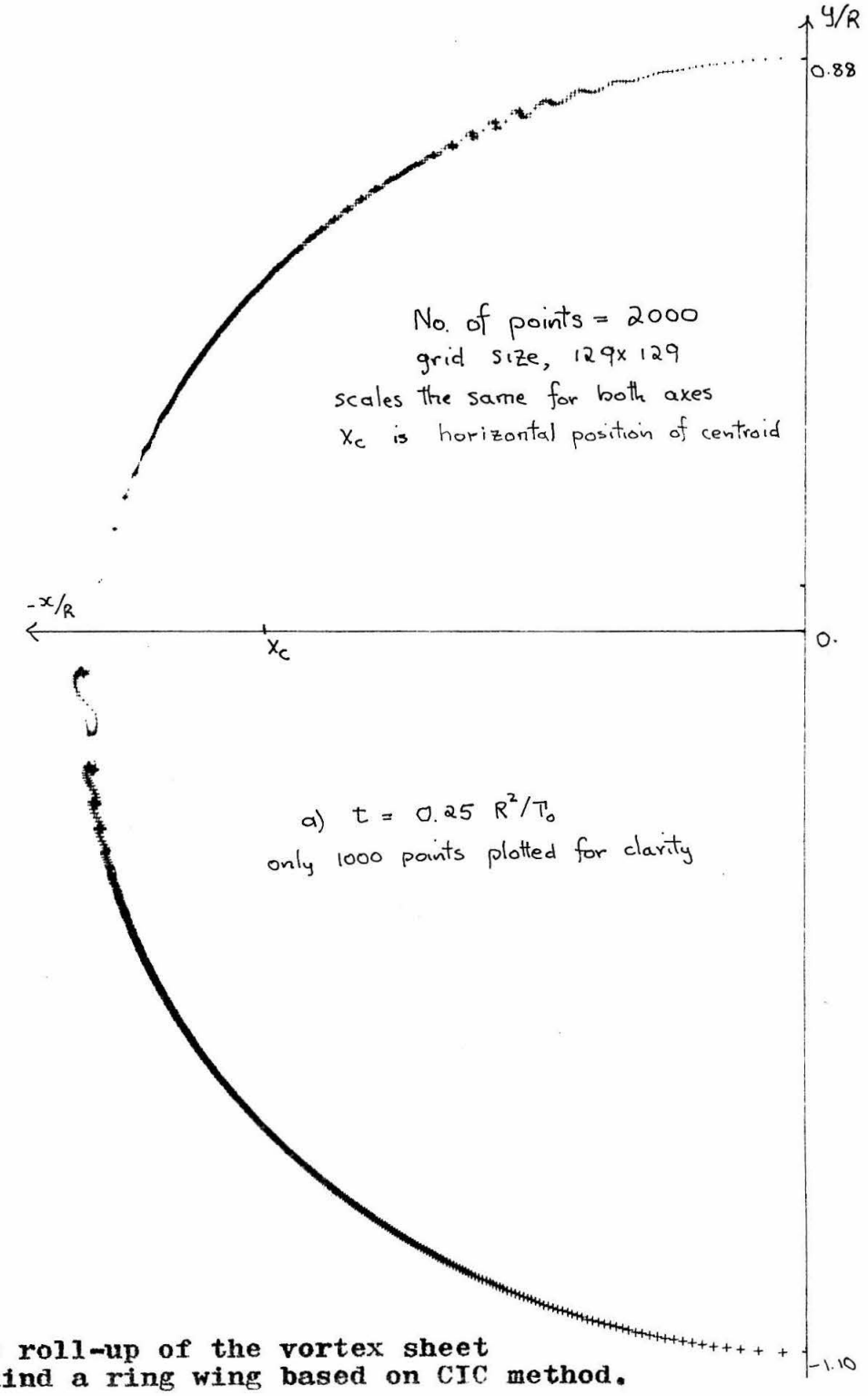

The roll-up of the vortex sheet behind a ring wing based on CIC method.

Figure 2.22

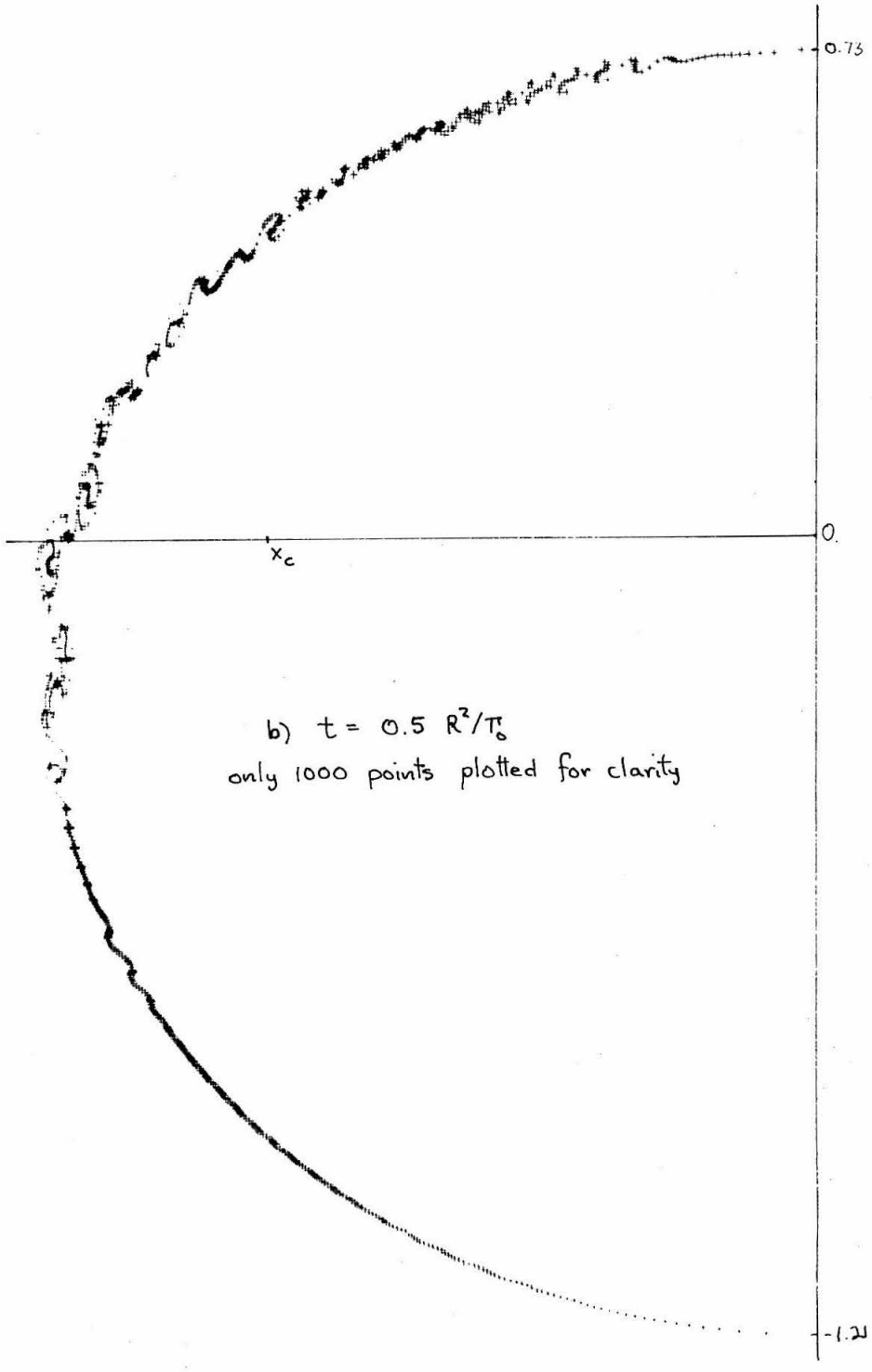

b) $t = 0.5\ R^2/\Gamma_0$
only 1000 points plotted for clarity

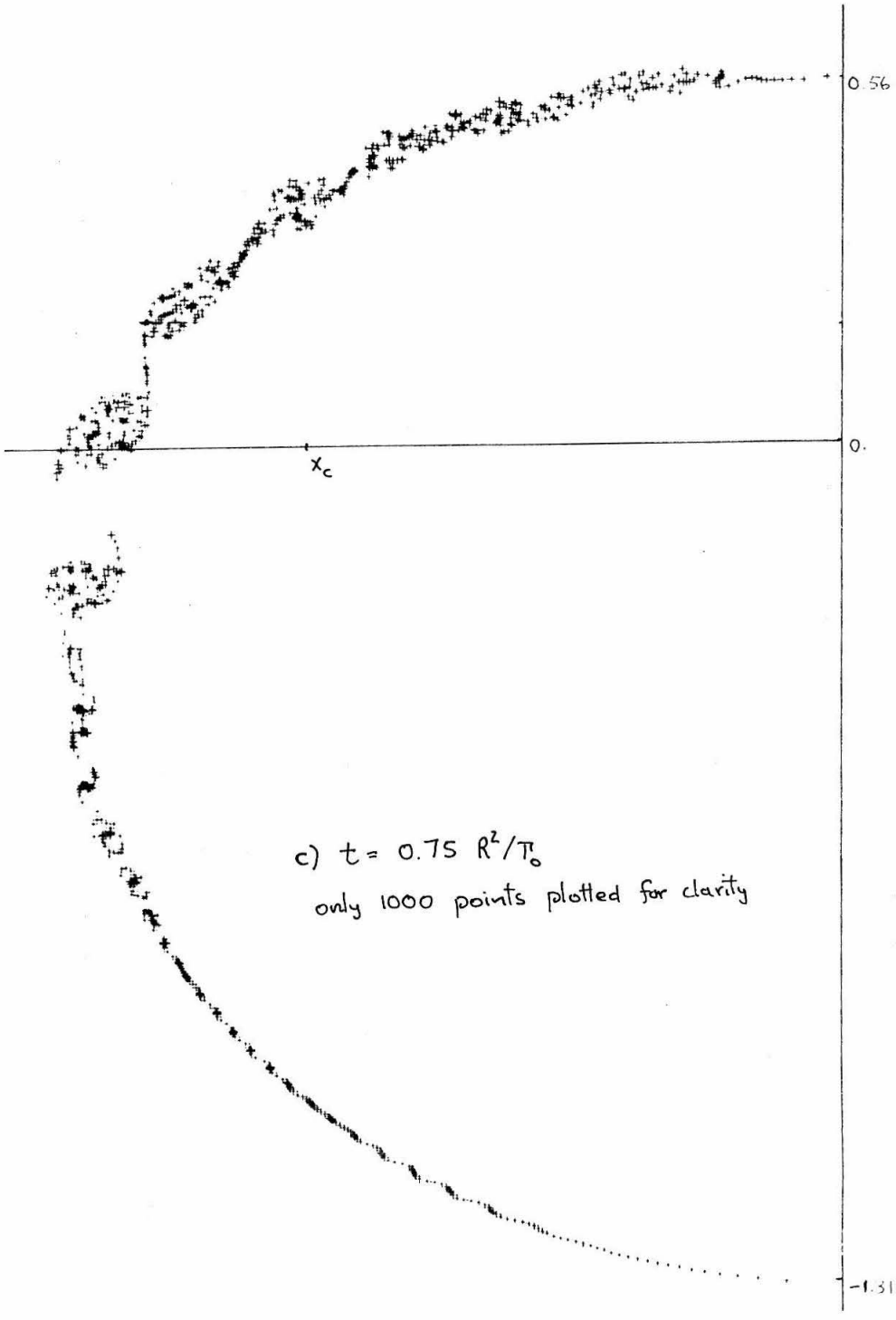

c) $t = 0.75\ R^2/T_0$

only 1000 points plotted for clarity

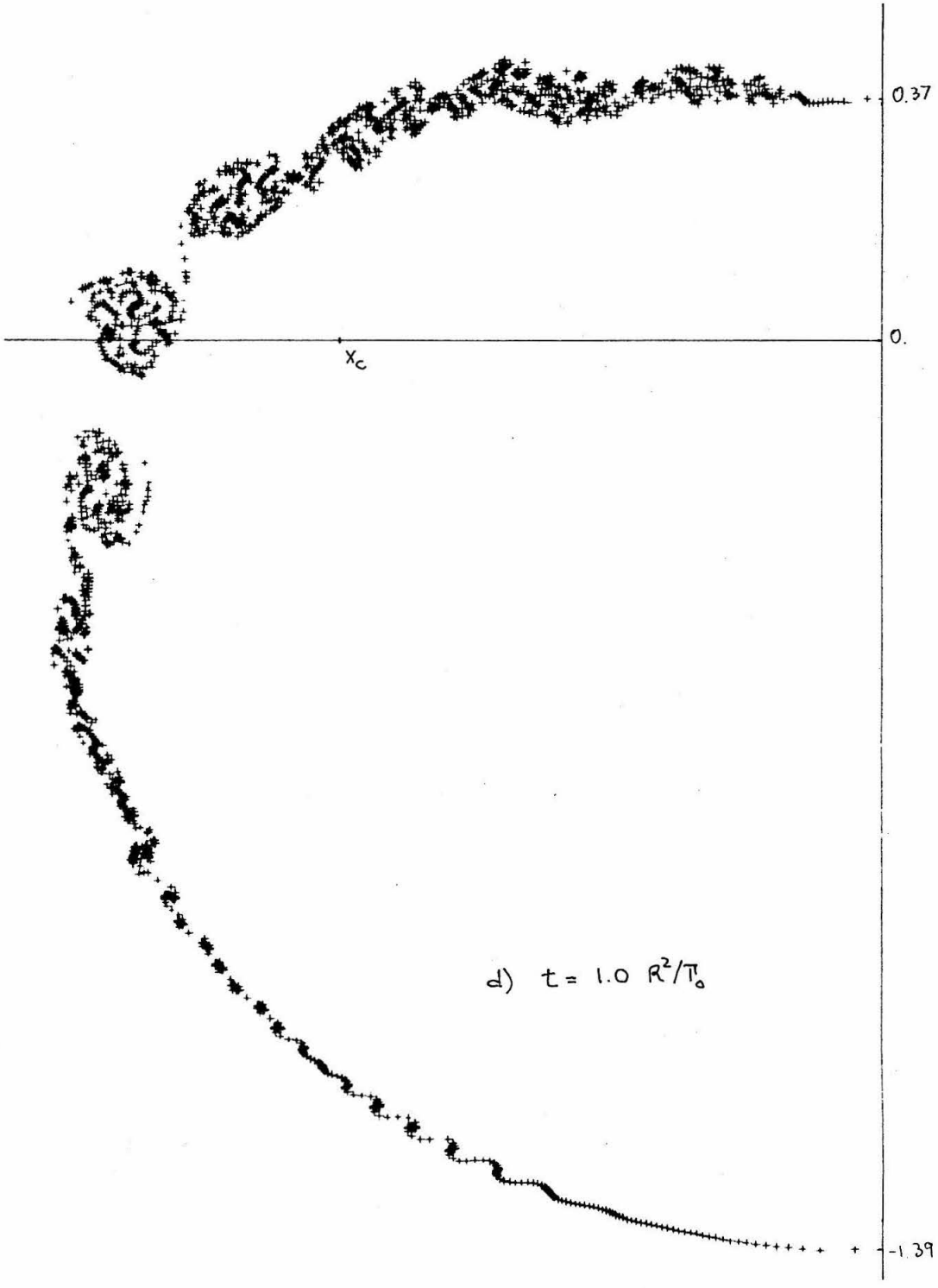
0.37
0.
x_c
-1.39
d) $t = 1.0\ R^2/\Gamma_0$

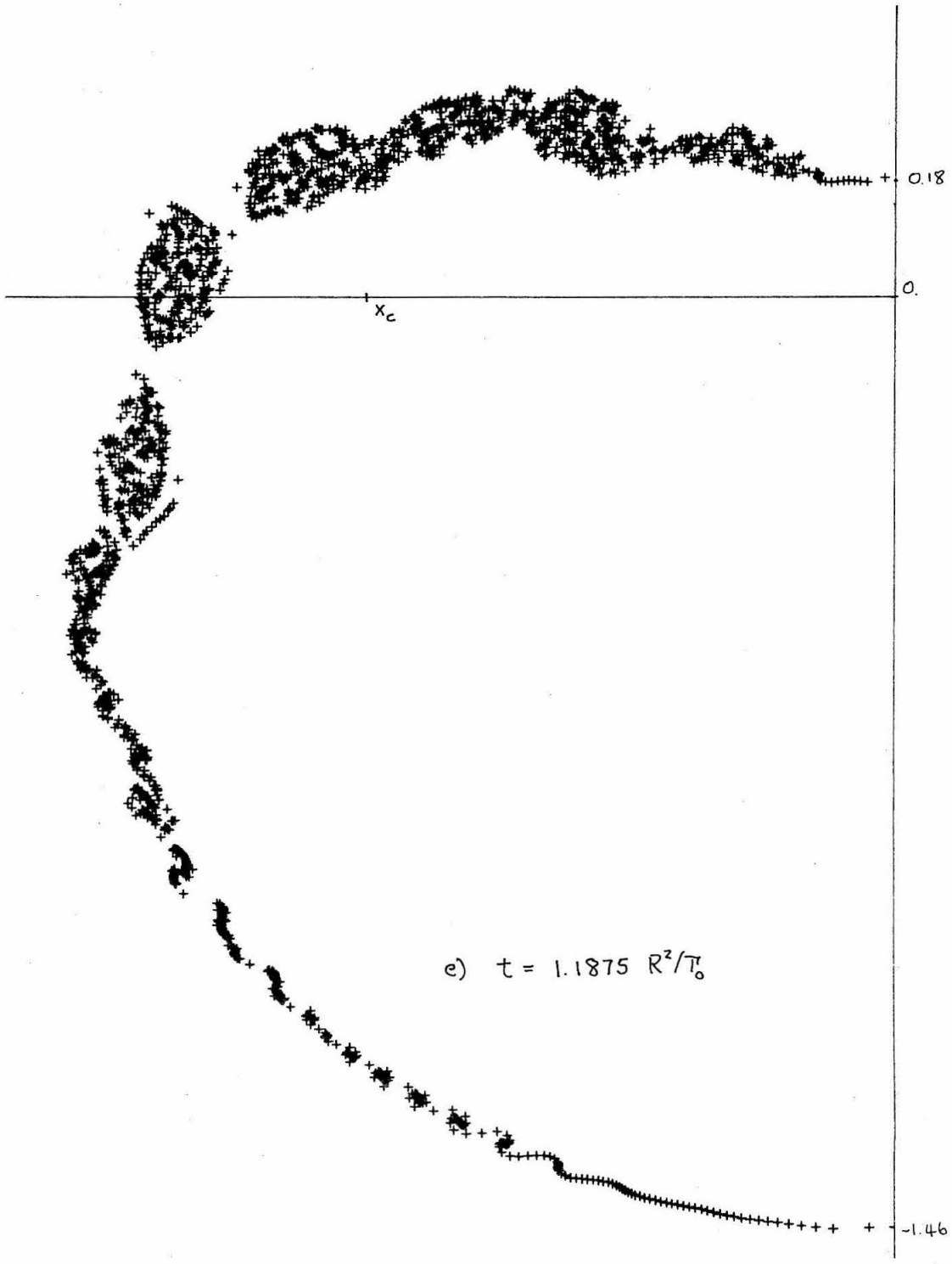

e) $t = 1.1875\ R^2/\Gamma_o$

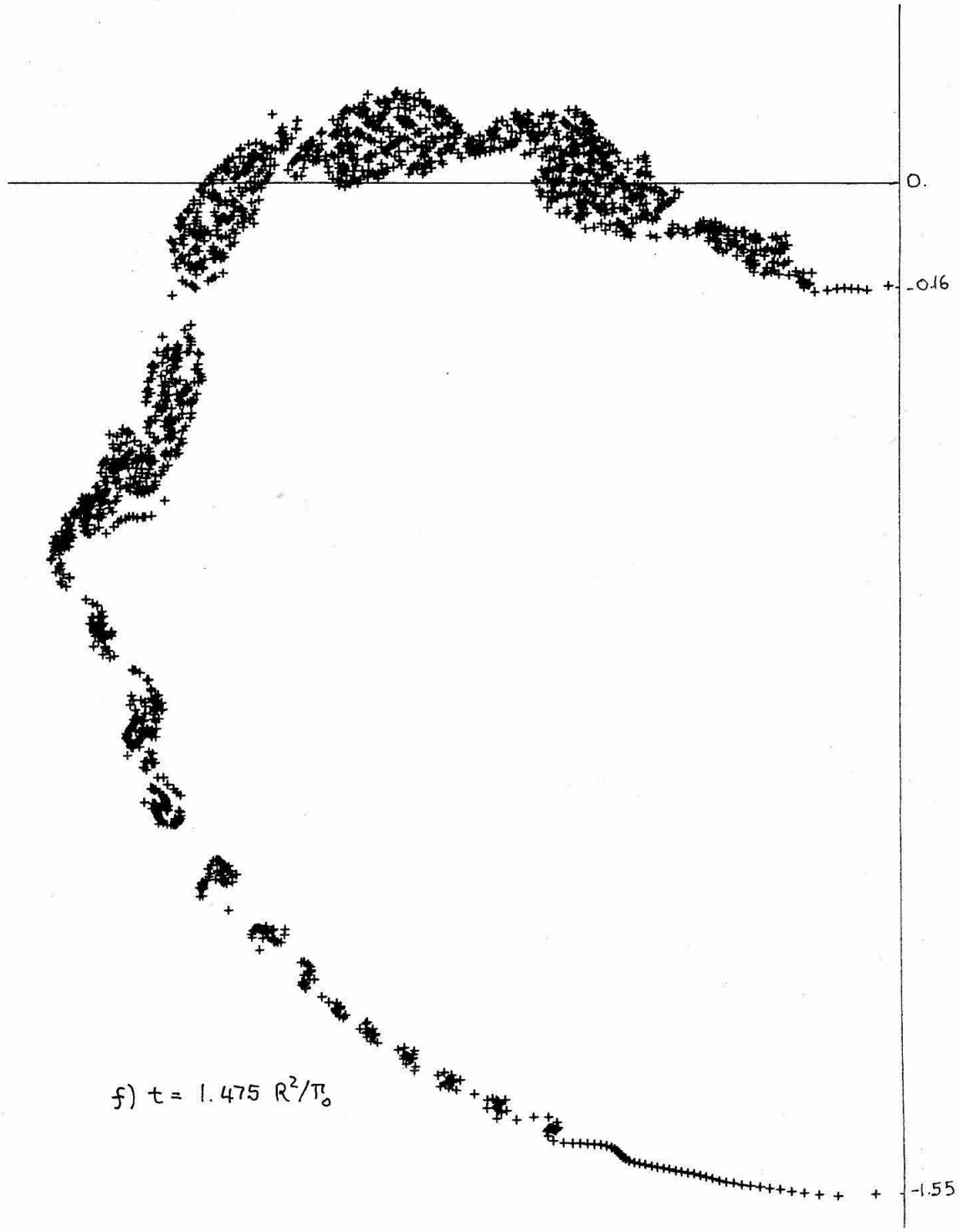
0.
-0.16
-1.55
f) t = 1.475 R²/Γ₀

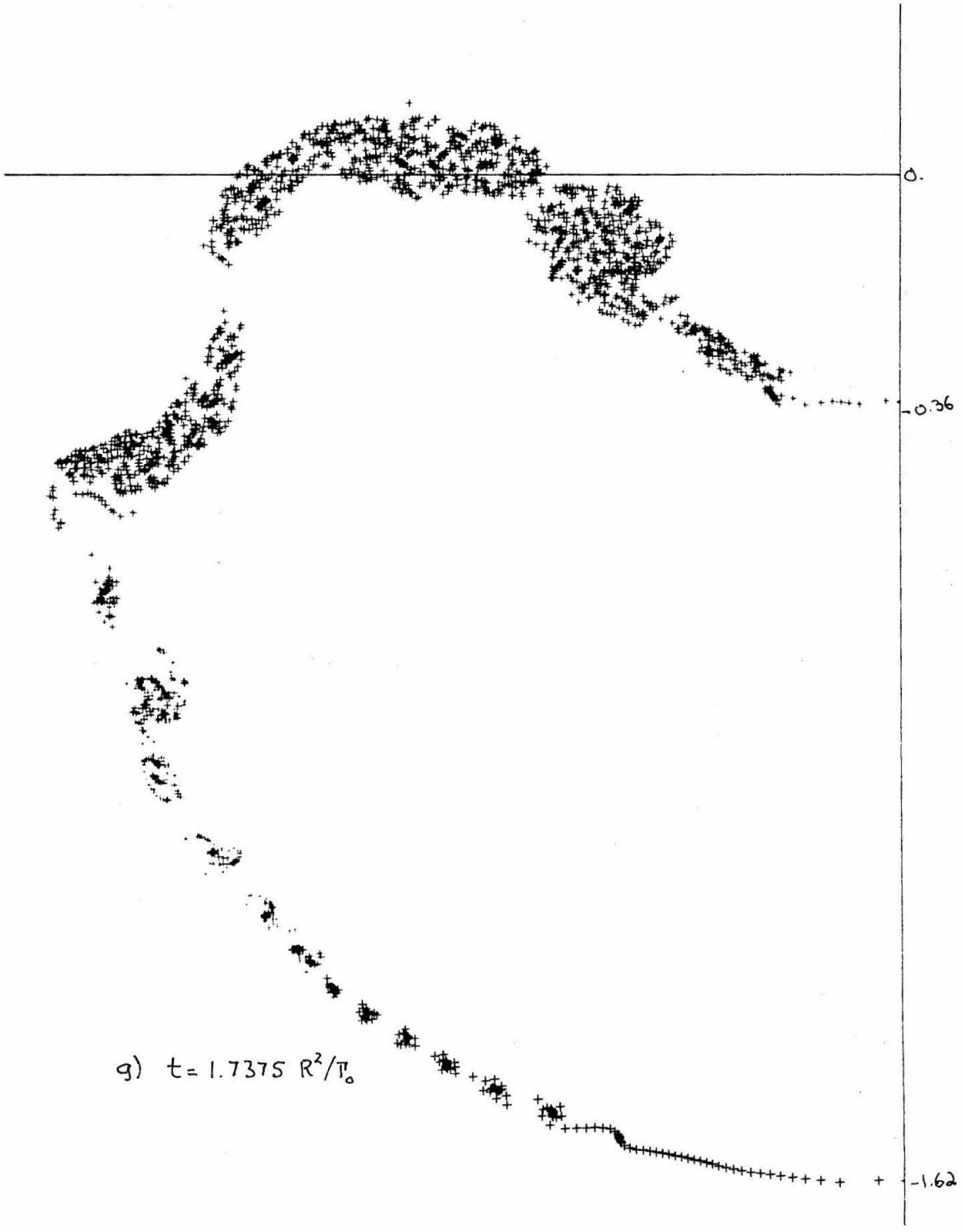

g) $t = 1.7375\ R^2/\Gamma_0$

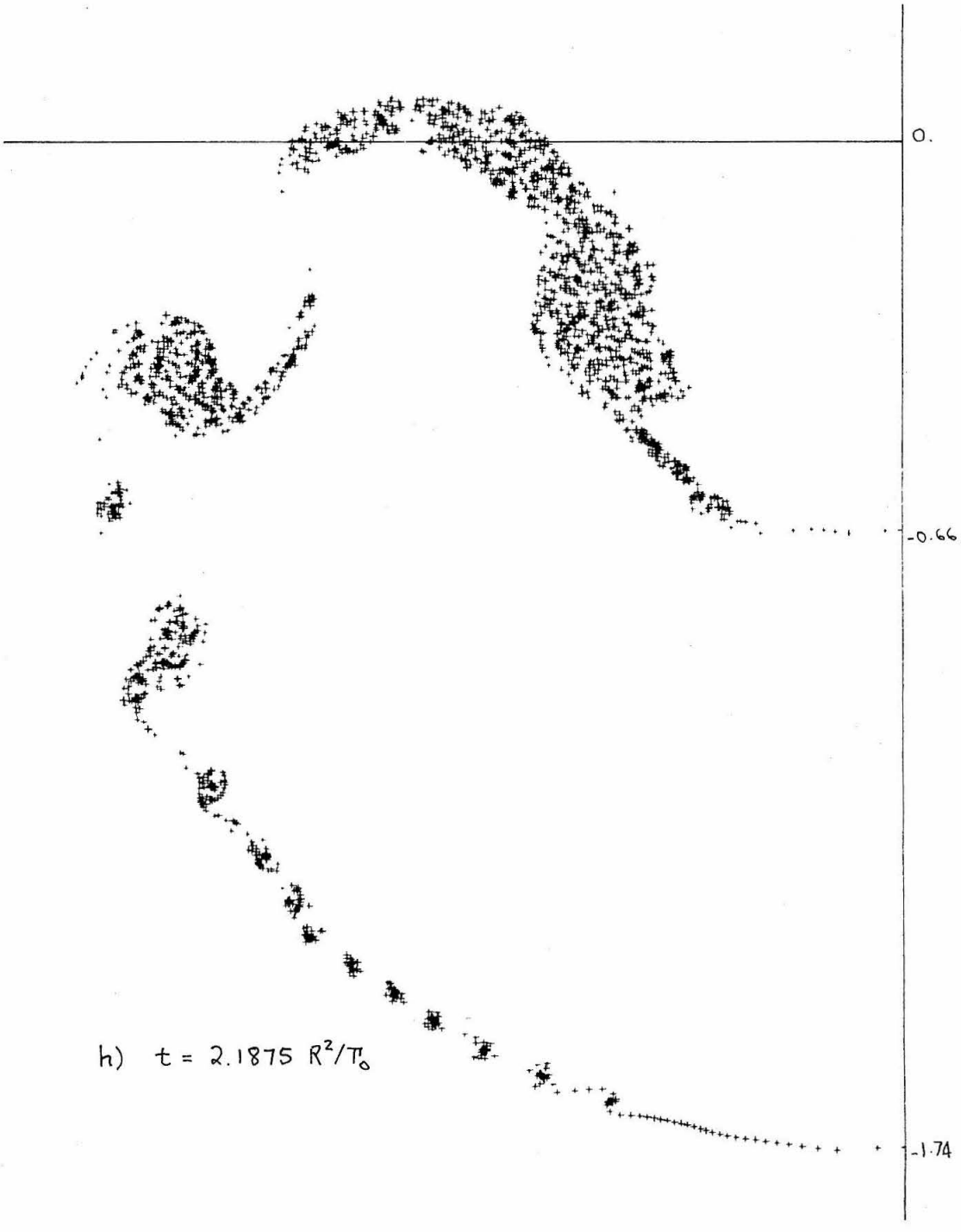
0.
-0.66
-1.74
h) t = 2.1875 R²/π₀

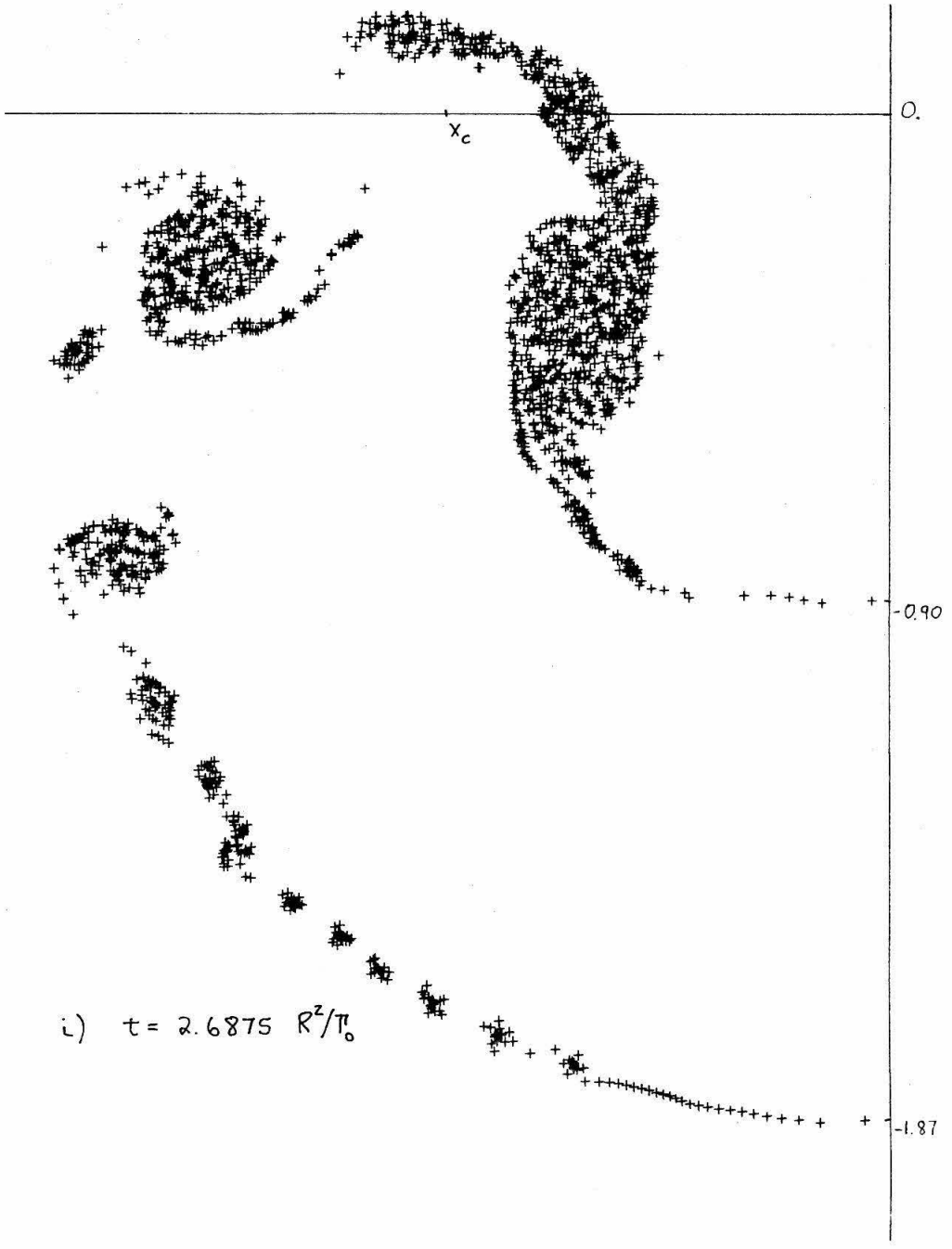
0.
x_c
-0.90
-1.87
i) t = 2.6875 R^2/π_0

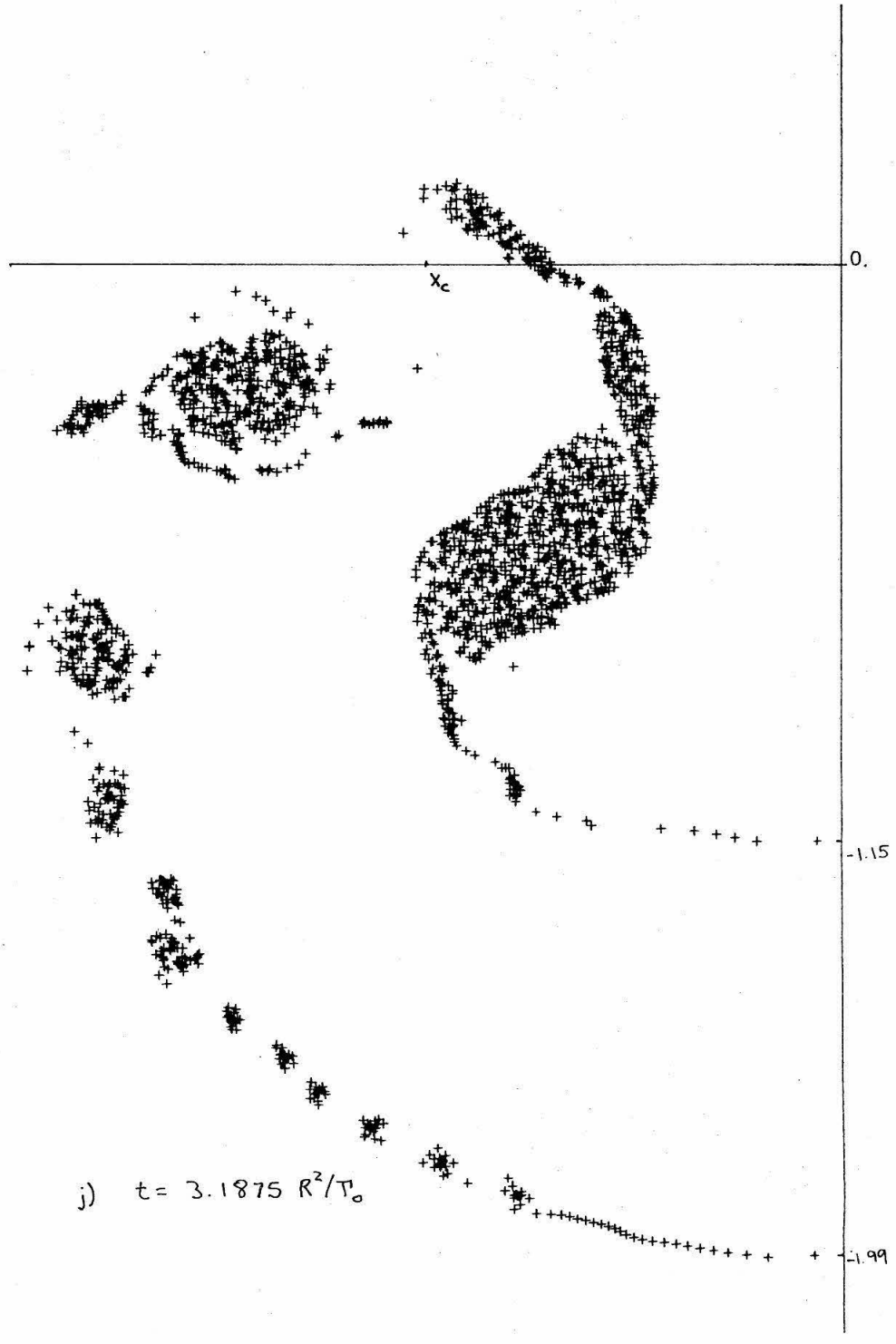

j) $t = 3.1875\ R^2/\Gamma_0$

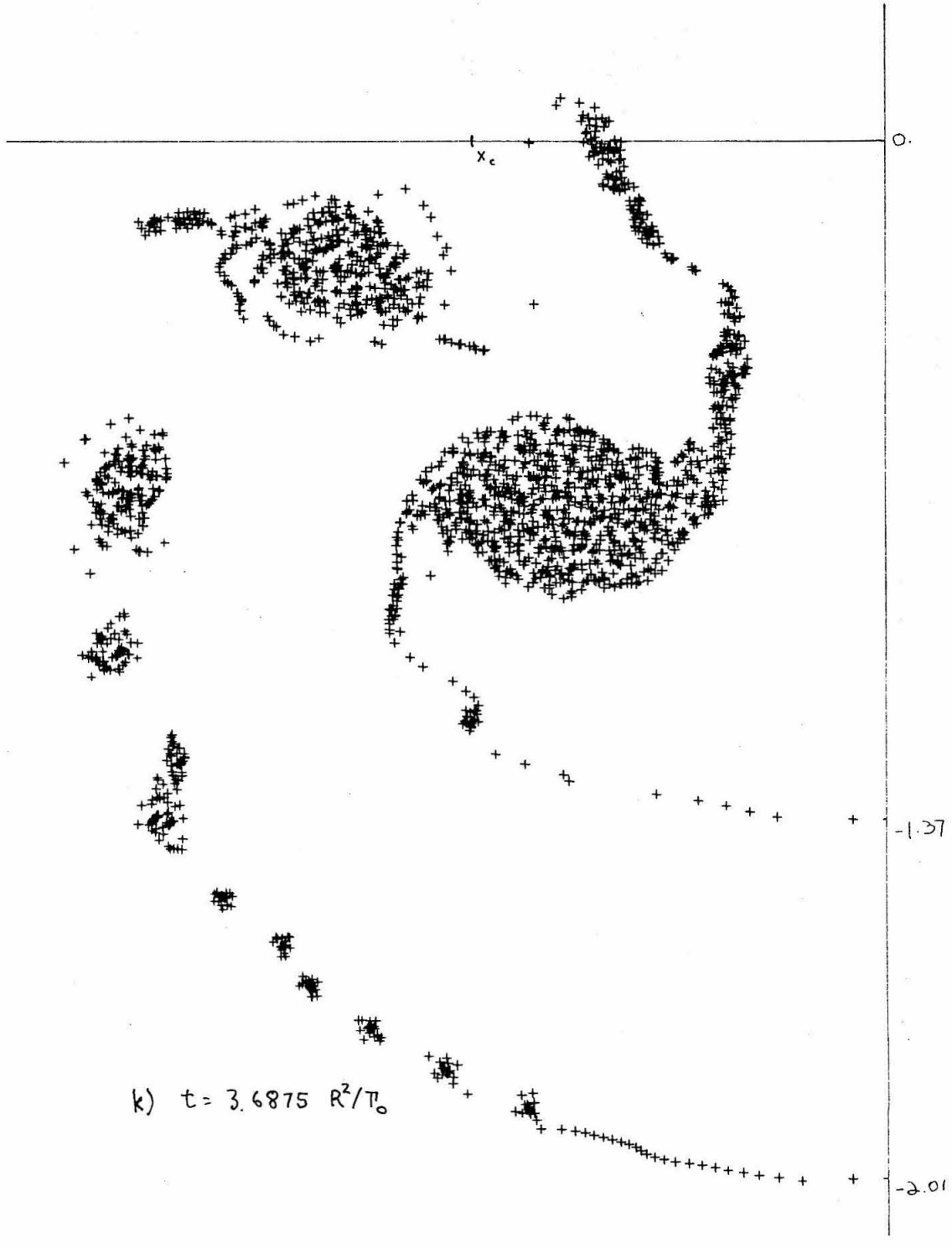

k) $t = 3.6875\ R^2/\Gamma_0$

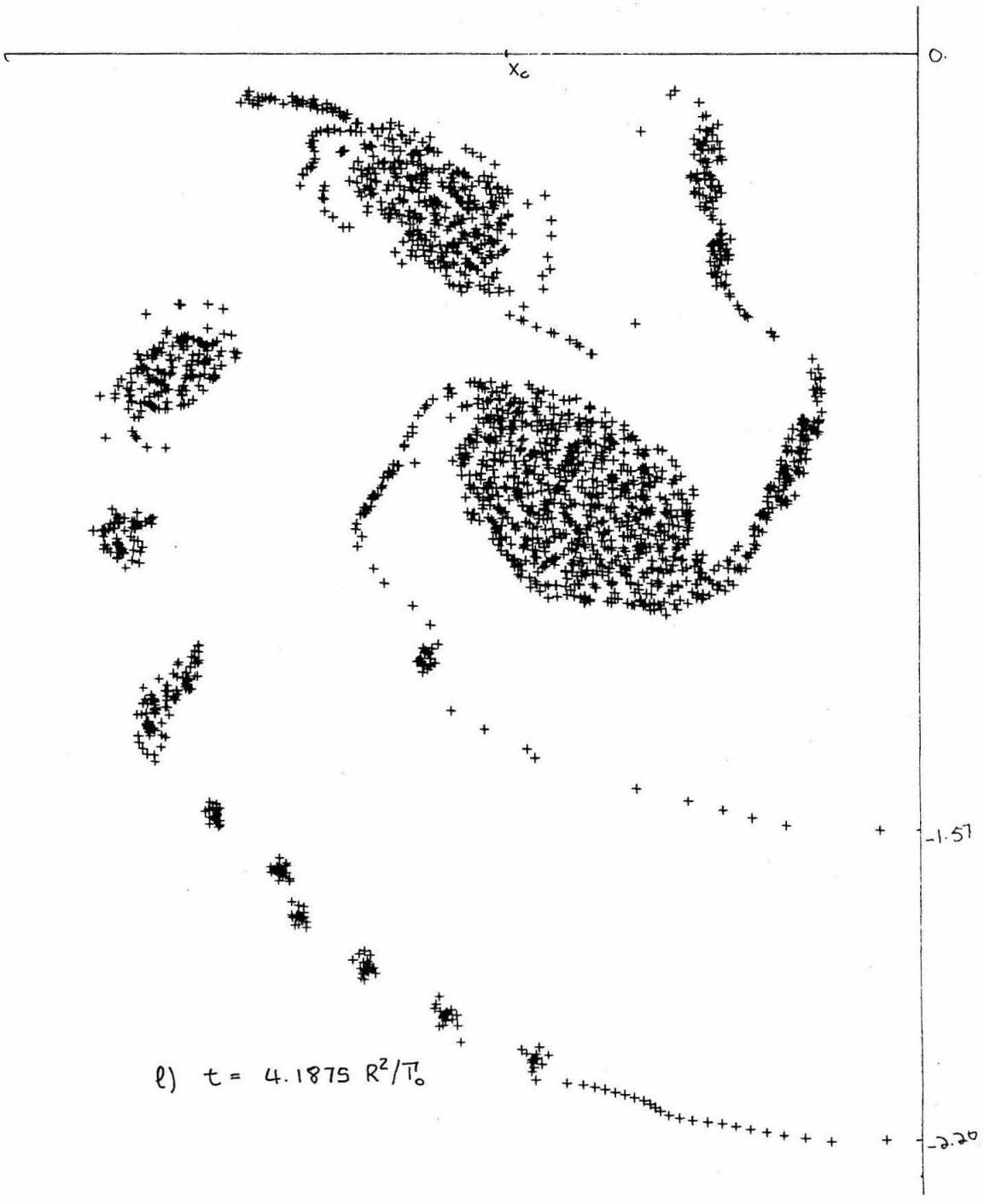
x_c
0.
-1.57
-2.20
l) $t = 4.1875\ R^2/T_o$

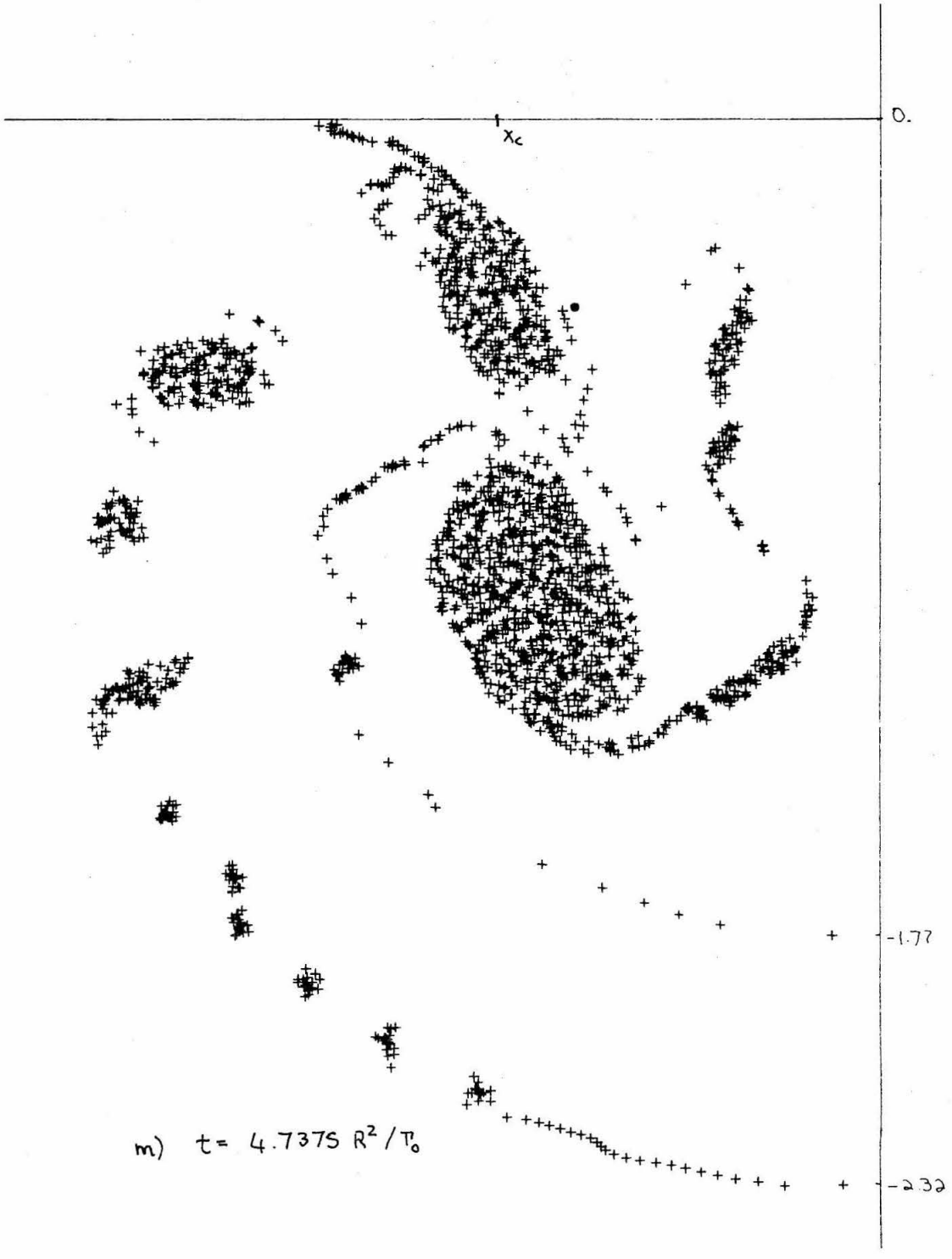

m) $t = 4.7375\ R^2/\Gamma_0$

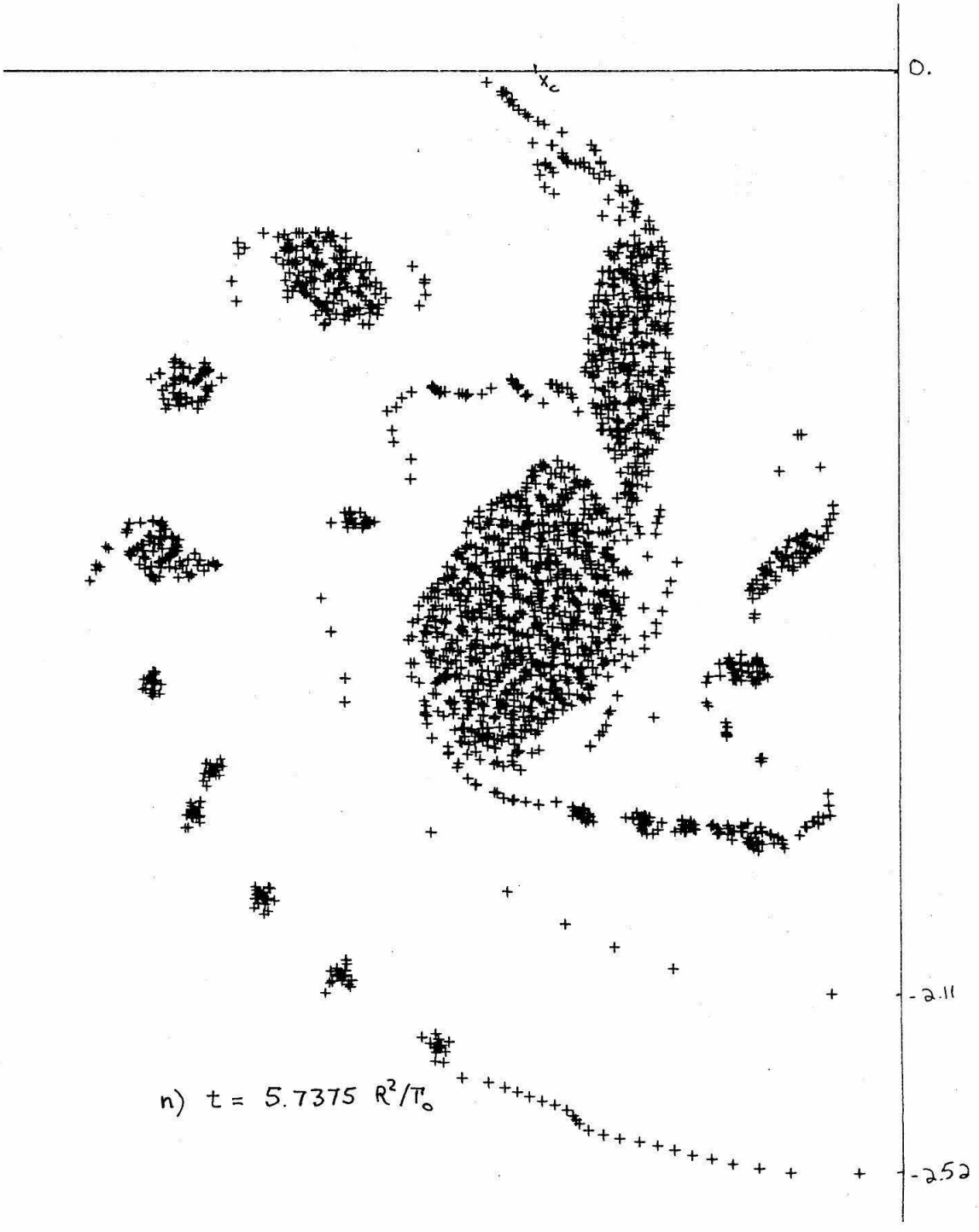
0.
x_c
-2.11
-2.52
n) $t = 5.7375\ R^2/\Gamma_o$

Chapter 3

A Study of the Motion of a Buoyant Pair of Line Vortices

I. INTRODUCTION

In the previous chapter, the motion of a vortex sheet in a homogeneous two-dimensional fluid is studied. In particular, numerical means are examined to find accurate solutions to the governing equations. In this chapter the condition that the fluid is homogeneous is relaxed by allowing density variations in the fluid. The flow will be considered laminar and inviscid in an attempt to separately study the influence of buoyancy. The general problem is hard and so a particular situation will be considered.

For some time now there has been great interest in determining the motion of a vortex pair through a stably stratified medium. The most notable example of this situation is the behaviour of the wake behind an aircraft. As discussed in the previous chapter, the vortex sheet shed from the trailing edge of the wing rolls up into two contra-rotating vortex cores. The problem of interest then is to determine how the vortex pair moves through the atmosphere once the roll-up is completed. Taking the idealisation that the vortex pair consists of two line vortices whose circulation is $\pm\Gamma$ situated $2R_o$ apart, then there is a known solution for uniformly constant density (Lamb (1932), § 155)

in which both vortices move downwards at constant speed

$$V_0 = \frac{\Gamma}{4\pi R_0} \tag{3.1}$$

Figure 3.1 shows the streamlines for this solution in coordinates fixed with the vortex pair. There is a streamline given by

$$\frac{x}{2R_0} + \log \frac{r_1}{r_2} = 0 \tag{3.2}$$

$$r_1^2 = (x - R_0)^2 + y^2 \quad , \quad r_2^2 = (x + R_0)^2 + y^2 \tag{3.3}$$

which forms an oval, C , around the vortices. Fluid bounded by this oval moves with the vortices.

When the atmosphere is stably stratified (as y decreases, i.e. in the direction of the gravity force, the density increases), the vortex pair convects downwards carrying lighter fluid into regions of more dense fluid. Since the fluid inside the initial oval rotates around the line vortices, mixing will remove any density variations. Without the effects of viscosity or turbulence, there will be a sharp interface separating the uniform density associated with the fluid carried by the line vortices and the stratified fluid outside. As the vortices move downwards, buoyancy will alter the speed of the vortices and change the shape of the interface.

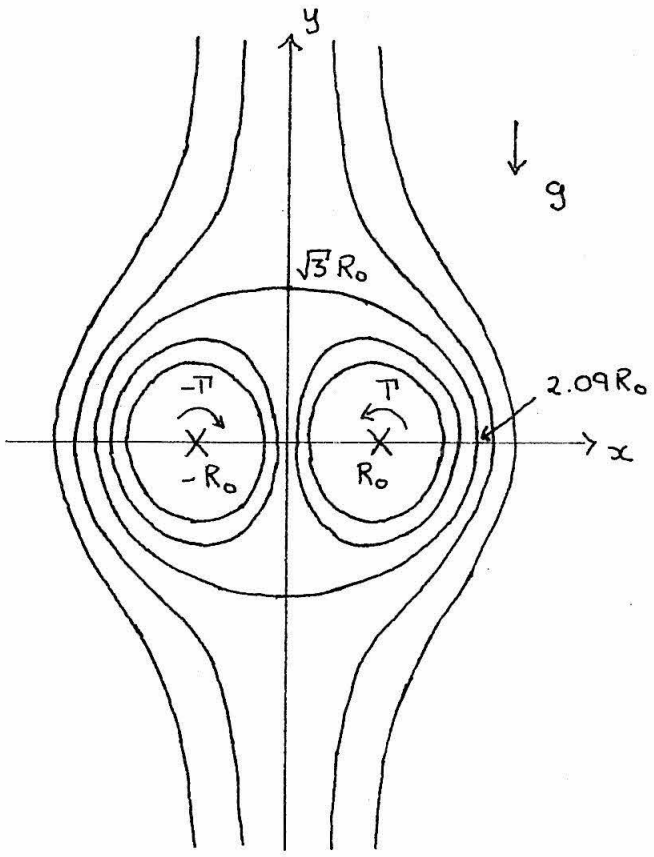

The streamlines for a pair of line vortices in coordinates fixed with the pair.

Figure 3.1

Although a number of authors (Turner (1960), Scorer and Davenport (1970) and Tombach (1971)) have used the equation describing the rate of change of the classical hydrodynamic impulse to model the motion of the vortex wake, Saffman (1972) has shown the concept of the impulse loses its classical meaning when the density is not uniform. With the impulse given by

$$\vec{I} = \int \rho \, \vec{r} \times \vec{\omega} \, dA \tag{3.4}$$

Saffman (1972) obtains the result that, in general,

$$\frac{d\vec{I}}{dt} - \int \rho \, \vec{g} \, dA \neq 0 \tag{3.5}$$

However, he does establish that, with the Boussinesq approximation (i.e. density differences are small), and letting $\rho_0(y)$ be the undisturbed density,

$$\frac{d\vec{I}}{dt} = \int (\rho - \rho_0) \, \vec{g} \, dA \tag{3.6}$$

where the impulse is now given by

$$\vec{I} = \bar{\rho} \int \vec{r} \times \vec{\omega} \, dA \tag{3.7}$$

and $\bar{\rho}$ is some average density. For this to be correct, (3.7) must include all the vorticity in the flow. In

particular, vorticity is generated at the interface as well as in the flow surrounding the convection cell, as established by the equation

$$\frac{D\vec{\omega}}{Dt} = \frac{1}{\rho}\nabla\rho \times \vec{g} \qquad (3.8)$$

$\frac{D}{Dt}$ is the usual convectional derivative.

Since Scorer and Davenport (1970) and Tombach (1971) take the impulse to be

$$I = -2\rho\Gamma R \qquad (3.9)$$

where R is the changing separation distance of the line vortices, they have neglected the contribution from the vorticity at the interface and in the outside fluid, and their results are suspect.

Saffman (1972) makes use of (3.6) and (3.7) to model the motion of the cell in the following way. He considers the shape and size of the cell boundary to remain unchanged, i.e. no detrainment of the inside fluid nor entrainment of outside fluid. Since the boundary is regarded as steady, the kinematics of the flow can easily be accounted for by appropriate choice of velocity potentials, allowing vorticity to be generated at the interface. Since the Boussinesq approximation is being used, the vorticity generated as a result of displacement in the fluid outside the cell can be

neglected to a good approximation. The dynamic condition at the boundary is satisfied in an approximate way by using (3.6) and (3.7) appropriately. This leads to the result for the downward velocity,

$$V = V_0 - \frac{\Delta\rho g}{\rho_I + C\rho_0} t \qquad (3.10)$$

where $\Delta\rho = \rho_0 - \rho_I$, ρ_0 , ρ_I being constant uniform densities for the outside, inside fluid respectively, and C is a shape factor estimated at 1.2. Although Saffman (1972) also obtains the result for the case $\rho_0 = \rho_I(1-\beta y)$, i.e. stratification of the outside fluid is taken into account, the result (3.10) is of more interest since it relates to the approximations made in this work. These approximations will be clarified later.

Saffman (1972) also explores the relative importance of viscous diffusion at the boundary as a means of entraining fluid into the region moving with the vortices, and the wave drag due to the vertical motion. His estimates suggest that neither of these effects will be important. Far more uncertain is the effect of turbulent mixing across the boundary. The Kelvin-Helmholtz instability of the interface may lead to turbulent mixing and the resulting entrainment may eventually bring the fluid to rest. Saffman (1972) attempts to take this into account by allowing the dimension of the shape (the shape is considered similar at all times)

to change and by using dimensional considerations to obtain an appropriate equation. Narain and Uberoi (1974) follow the modelling adapted by Saffman (1972) but include an energy equation which takes into account dissipation due to turbulent drag on the oval by the wake fluid and dissipation due to the form drag on the oval by the ambient fluid. These effects will not be considered in this work. The flow will be considered laminar as a first step in understanding the processes involved in the motion.

Crow (1974) attempts to elaborate on the effect of a possible drainage filament first proposed by Scorer and Davenport (1970). He neglects the time derivatives in the problem and obtains the steady vorticity distribution along the boundary of the cell. This generated vorticity then convects the line vortices closer together, which has the effect of speeding up their downward velocity. Even with some account taken of the vorticity generated by the displacement in the ambient fluid, the upwash is not strong enough to prevent a net downward acceleration.

The work in this chapter follows the lines adopted by Crow (1974) and Saffman (1972), i.e. regarding the flow as inviscid and laminar and neglecting the wave drag due to the gravity waves generated by the vortex wake. Although entrainment will be neglected, detrainment can be shown to occur supporting the reasoning of Scorer and Davenport (1970) and Crow (1974), and contradicting Saffman's (1972) picture

of the flow. However, numerical results obtained by Hill (1975b) suggest that Saffman's (1972) modelling is nevertheless accurate for small times and Crow's (1974) neglect of the time dependency in the generation of vorticity is unreasonable. All the authors mentioned make use of an assumption of similarity of shape and thus neglect any possibility of wake collapse due to the stratification of the ambient fluid. This work too will neglect this aspect by considering the density outside the wake to be uniform and constant, ρ_0 , and slightly larger than the density, ρ_I , in the convection cell. The Boussinesq approximation can then be applied. In this way the emphasis is on the effect of buoyancy on the wake trajectory.

In Section II, a Taylor's expansion in time is calculated confirming the accuracy of Saffman's (1972) model for small times.

This provides too a good check on the macroscopic model introduced in Section III to describe the wake trajectory for finite times. This model allows a tail to develop and includes its effect on the motion. For large times, the wake fluid detrains away and the line vortices begin to accelerate downwards again after their initial slowdown. Finally, this model is checked against numerical calculations involving the method developed by Fink and Soh (1974) which is discussed in detail in Chapter 3. There is good agreement suggesting the model is accurate enough to describe the

gross features of the wake motion.

II. THE TAYLOR SERIES IN TIME

This section describes the calculation of the first few terms of a Taylor series expansion in time of the flow variables describing the motion of the line vortices and the change of shape of the interface. At $t = 0^-$, the density is considered uniform and constant, ρ_I, throughout the flow and the flow field is known (see (3.1-3), or Lamb (1932), § 155). At $t = 0$, the density outside the convection cell is increased slightly to ρ_o. This corresponds to adding an impulse to the flow and the deformation of the interface must be calculated to $O(t^2)$ in order to see the effect of buoyancy.

The coordinate system is shown in Figure 3.2. Let the density difference be denoted by $\Delta\rho$

$$\Delta\rho = \rho_o - \rho_I \tag{3.11}$$

When $\Delta\rho = 0$, the velocity potential for a pair of line vortices is given by

$$\Phi = \frac{\Gamma}{2\pi}\left\{\arctan\left(\frac{\sigma\sin\phi}{\sigma\cos\phi - R}\right) - \arctan\left(\frac{\sigma\sin\phi}{\sigma\cos\phi + R}\right)\right\} \tag{3.12}$$

in coordinates fixed with the vortices whose strengths are $\pm\Gamma$. If $Y(t)$ measures the downward position of the line vortices, then the following geometrical identities are obvious.

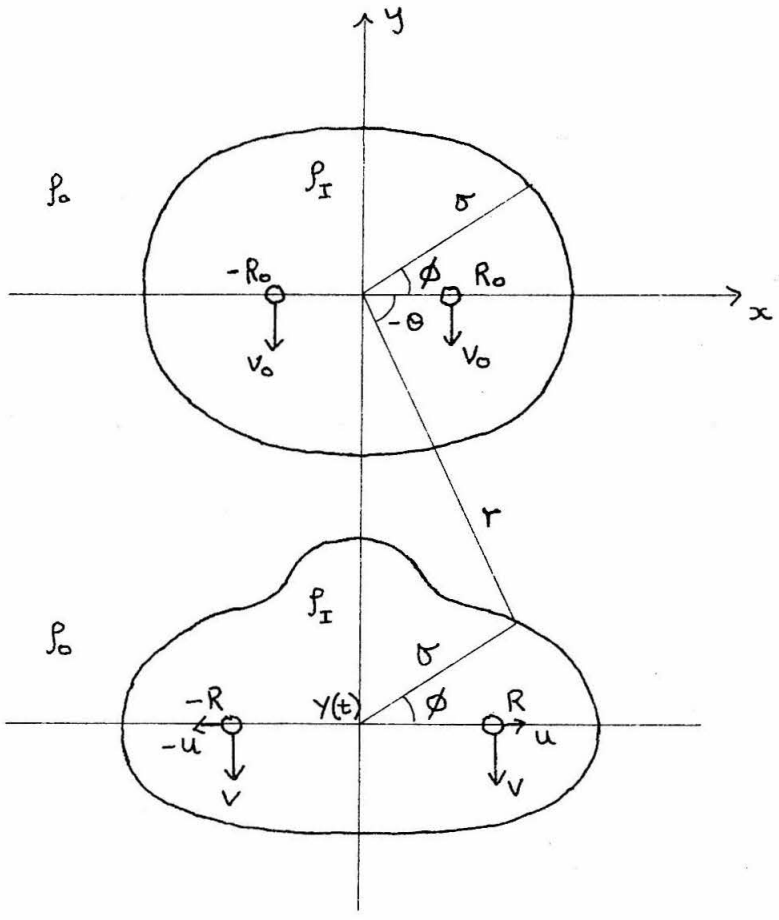

The coordinate systems and parameters used.

Figure 3.2

$$r\cos\theta = \sigma\cos\phi \tag{3.13}$$

$$\sigma\sin\phi - r\sin\theta = Y(t) = \int_0^t v(t)dt \tag{3.14}$$

In coordinates fixed with the fluid at rest at ∞, the potential due to the vortex pair is

$$\Phi = \frac{\Gamma}{2\pi}\left\{\arctan\left(\frac{r\sin\theta + Y(t)}{r\cos\theta - R(t)}\right) - \arctan\left(\frac{r\sin\theta + Y(t)}{r\cos\theta + R(t)}\right)\right\} \tag{3.15}$$

Expanding in a power series in time,

$$V(t) = V_0 + V_1 t + O(t^2)\,, \quad V_0 = \frac{\Gamma}{4\pi R_0} \tag{3.16}$$

$$u(t) = u_1 t + O(t^2) \tag{3.17}$$

$$R(t) = R_0 + u_1\frac{t^2}{2} + O(t^3) \tag{3.18}$$

$$Y(t) = V_0 t + V_1\frac{t^2}{2} + O(t^3) \tag{3.19}$$

and the potential inside will be

$$\Phi^I = \Phi_0 + \Phi_1 t + \Psi^I t + O(t^2) \tag{3.20}$$

while outside

$$\Phi^{\circ} = \Phi_0 + \Phi_1 t + \Psi^{\circ} t + O(t^2) \tag{3.21}$$

where Φ_0 , Φ_1 , are obtained by expanding (3.15).

$$\Phi_0 = \frac{\Gamma}{2\pi}\left\{\arctan\left(\frac{r\sin\theta}{r\cos\theta - R_0}\right) - \arctan\left(\frac{r\sin\theta}{r\cos\theta + R_0}\right)\right\} \tag{3.22}$$

$$\Phi_1 = \frac{\Gamma}{2\pi} V_0 \left\{\frac{r\cos\theta - R_0}{r^2 + R_0^2 - 2rR_0\cos\theta} - \frac{r\cos\theta + R_0}{r^2 + R_0^2 + 2rR_0\cos\theta}\right\} \tag{3.23}$$

The contributions $\Psi^{I} t$ and $\Psi^{\circ} t$ are due to buoyancy. Since the flow outside is irrotational and $\nabla^2\Phi_0 = \nabla^2\Phi_1 = 0$,

$$\nabla^2 \Psi^{\circ} = 0 \tag{3.24}$$

In the inside region, $\nabla^2\Phi_0$ and $\nabla^2\Phi_1$ will vanish except at the line vortices. However, since the motion of the line vortices is included in the expansion when calculating Φ_0 and Φ_1 , Ψ^{I} will be free of singularity and

$$\nabla^2 \Psi^{I} = 0 \tag{3.25}$$

The interface is given by

$$r = \zeta(\theta, t) = \zeta_0(\theta) + \zeta_1(\theta) t + \zeta_2(\theta)\frac{t^2}{2} + O(t^3) \tag{3.26}$$

The kinematic condition is

$$\frac{\partial \eta}{\partial t} - \frac{\partial \Phi}{\partial r} + \frac{1}{\eta^2}\frac{\partial \Phi}{\partial \theta}\frac{\partial \eta}{\partial \theta} = 0 \qquad \text{at } r = \eta(\theta,t) \tag{3.27}$$

where Φ has the value Φ^o , Φ^I for outside, inside flow respectively. The implicit behaviour in time in the derivatives of the potential is removed by expanding them in a Taylor series about $r = \eta_o$. Thus

$$\eta_1 + \eta_2 t - \frac{\partial \Phi_o}{\partial r} - \frac{\partial^2 \Phi_o}{\partial r^2}\eta_1 t - \frac{\partial \Phi_1}{\partial r} t - \frac{\partial \Psi}{\partial \theta} t + \frac{1}{\eta_o^2}\left(1 - 2\frac{\eta_1}{\eta_o} t\right)\cdot\left[\frac{\partial \Phi_o}{\partial \theta}\right.$$

$$\left. + \frac{\partial^2 \Phi_o}{\partial r \partial \theta}\eta_1 t + \frac{\partial \Phi_1}{\partial \theta} t + \frac{\partial \Psi}{\partial \theta} t\right]\left[\frac{d\eta_o}{d\theta} + \frac{d\eta_1}{d\theta} t\right] + O(t^2) = 0 \tag{3.28}$$

Ψ refers to either inside or outside, i.e. Ψ^I or Ψ^o respectively, and so (3.28) represents two equations. The lowest order terms give

$$\eta_1 - \frac{\partial \Phi_o}{\partial r} + \frac{1}{\eta_o^2}\frac{\partial \Phi_o}{\partial \theta}\frac{d\eta_o}{d\theta} = 0 \qquad \text{at } r = \eta_o \tag{3.29}$$

$$\eta_2 - \frac{\partial^2 \Phi_o}{\partial r^2}\eta_1 - \frac{\partial \Phi_1}{\partial r} - \frac{\partial \Psi}{\partial r} + \left(\frac{1}{\eta_o^2}\frac{\partial^2 \Phi_o}{\partial r \partial \theta}\eta_1 + \frac{1}{\eta_o^2}\frac{\partial \Phi_1}{\partial \theta} + \frac{1}{\eta_o^2}\frac{\partial \Psi}{\partial \theta}\right)\frac{d\eta_o}{d\theta}$$

$$- \frac{2\eta_1}{\eta_o}\frac{\partial \Phi_o}{\partial \theta}\frac{d\eta_o}{d\theta} + \frac{1}{\eta_o^2}\frac{\partial \Phi_o}{\partial \theta}\frac{d\eta_1}{d\theta} = 0 \quad \text{at } r = \eta_o \tag{3.30}$$

The interesting part of the deformation of the interface is that due to the buoyancy effects. In order to obtain this component in the expansion of η , the change in the shape due to the downward motion of the line vortices

is calculated and subtracted from η . Figure 3.3 illustrates the situation and defines the coordinates used. Thus

$$\Delta r = r_1 - \eta_0(\theta)$$

$$\theta_1 = \theta + \Delta\theta \tag{3.31}$$

The following geometrical identities prove useful.

$$r_1 \cos\theta = \eta_0(\theta_1)\cos\theta_1 \tag{3.32}$$

which becomes

$$r_1 \cos\theta = \eta_0(\theta)\cos\theta - \left(\eta_0(\theta)\sin\theta - \frac{d\eta_0(\theta)}{d\theta}\cos\theta\right)\Delta\theta$$

$$- \left(\eta_0(\theta)\cos\theta + 2\frac{d\eta_0(\theta)}{d\theta}\sin\theta - \frac{d^2\eta_0(\theta)}{d\theta^2}\cos\theta\right)\frac{\Delta\theta^2}{2} + O(\Delta\theta^3) \tag{3.33}$$

Also

$$V_0 t + V_1\frac{t^2}{2} + O(t^3) + r_1\sin\theta = \eta_0(\theta_1)\sin\theta_1 \tag{3.34}$$

After some algebraic manipulation and using (3.32), (3.34) becomes

$$\left[V_0 t + V_1\frac{t^2}{2} + O(t^3)\right]\cos\theta = \eta_0(\theta)\Delta\theta + \frac{d\eta_0(\theta)}{d\theta}\Delta\theta^2 + O(\Delta\theta^3) \tag{3.35}$$

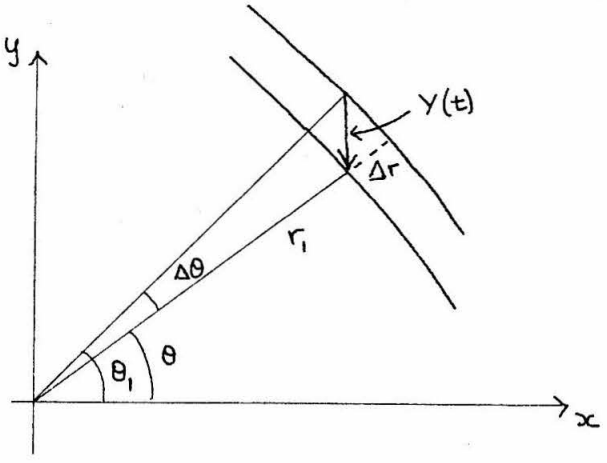

The coordinate system used to calculate the change in ζ due to the downward motion of the initial shape.

Figure 3.3

Expanding $\Delta\theta$ in a Taylor series in time,

$$\Delta\theta = \alpha t + \beta t^2 \tag{3.36}$$

and substituting into (3.35), leads to

$$\alpha = \frac{V_0 \cos\theta}{\eta_0} \quad ; \quad \beta = \frac{V_1 \cos\theta}{2\eta_0} - \frac{1}{\eta_0^3}\frac{d\eta_0}{d\theta} V_0^2 \cos^2\theta \tag{3.37}$$

Now Δr can be calculated directly from (3.33).

$$\Delta r = -\left(V_0 \sin\theta - \frac{1}{\eta_0}\frac{d\eta_0}{d\theta} V_0 \cos\theta\right) t - \left(\eta_0 \sin\theta - \frac{d\eta_0}{d\theta}\cos\theta\right) V_1 \frac{t^2}{2}$$

$$- \frac{1}{\eta_0^2}\left[\eta_0 + \frac{2}{\eta_0}\left(\frac{d\eta_0}{d\theta}\right)^2 - \frac{d^2\eta_0}{d\theta^2}\right] V_0^2 \cos^2\theta \frac{t^2}{2} \tag{3.38}$$

The following identity proves useful.

$$\eta_1 = \frac{\partial \Phi_0}{\partial r} - \frac{1}{\eta_0^2}\frac{d\eta_0}{d\theta}\frac{\partial \Phi_0}{\partial \theta} \equiv -V_0 \sin\theta + \frac{V_0}{\eta_0}\frac{d\eta_0}{d\theta}\cos\theta \quad \text{at } r = \eta_0 \tag{3.39}$$

Thus the $O(t)$ terms of (3.29) and (3.38) are equivalent and so there is no effect of buoyancy on the interface to this order and the next term at least is needed. Differentiating (3.39) gives

$$\frac{d\eta_1}{d\theta} = \frac{\partial^2 \Phi_0}{\partial r\,\partial\theta} + \frac{\partial^2 \Phi_0}{\partial r^2}\frac{d\eta_0}{d\theta} + \frac{2}{\eta_0^3}\left(\frac{d\eta_0}{d\theta}\right)^2 \frac{\partial \Phi_0}{\partial \theta} - \frac{1}{\eta_0^2}\frac{\partial^2 \Phi_0}{\partial r\,\partial\theta}\left(\frac{d\eta_0}{d\theta}\right)^2 - \frac{1}{\eta_0^2}\frac{\partial^2 \Phi_0}{\partial \theta^2}\frac{d\eta_0}{d\theta} - \frac{1}{\eta_0^2}\frac{\partial \Phi_0}{\partial \theta}\frac{d^2\eta_0}{d\theta^2}$$

$$= -V_0\cos\theta - V_0\frac{\sin\theta}{\eta_0}\frac{d\eta_0}{d\theta} - V_0\frac{\cos\theta}{\eta_0^2}\left(\frac{d\eta_0}{d\theta}\right)^2 + V_0\frac{\cos\theta}{\eta_0}\frac{d^2\eta_0}{d\theta^2} \quad \text{at } r = \eta_0 \tag{3.40}$$

Another identity is

$$\Phi_1 \equiv V_0\left(\frac{\partial \Phi_0}{\partial r}\sin\theta + \frac{\partial \Phi_0}{\partial \theta}\frac{\cos\theta}{r}\right) \tag{3.41}$$

Expressions (3.40) and (3.41) reduce (3.30) to

$$\frac{\partial \Psi}{\partial r} - \frac{1}{\eta_0^2}\frac{d\eta_0}{d\theta}\frac{\partial \Psi}{\partial \theta} = \eta_2 + \frac{V_0}{\eta_0}\frac{d\eta_0}{d\theta}\frac{\partial \Phi_0}{\partial r}\cos\theta - \frac{V_0}{\eta_0^4}\left(\frac{d\eta_0}{d\theta}\right)^2\frac{\partial \Phi_0}{\partial \theta}\cos\theta + \frac{V_0^2\cos^2\theta}{\eta_0}$$

$$+ \frac{V_0^2}{\eta_0^3}\left(\frac{d\eta_0}{d\theta}\right)^2\cos^2\theta + \frac{V_0^2}{\eta_0^2}\frac{d\eta_0}{d\theta}\cos\theta\sin\theta - \frac{V_0^2}{\eta_0^2}\frac{d^2\eta_0}{d\theta^2}\cos^2\theta \quad \text{at } r=\eta_0$$

Using (3.39), this leads to

$$\frac{\partial \Psi}{\partial r} - \frac{1}{\eta_0^2}\frac{d\eta_0}{d\theta}\frac{\partial \Psi}{\partial \theta} = \eta_2 + \frac{2V_0^2}{\eta_0^3}\cos^2\theta + \frac{V_0^2}{\eta_0}\cos^2\theta$$

$$- \frac{V_0^2}{\eta_0^3}\cos^2\theta\frac{d^2\eta_0}{d\theta^2} \quad \text{at } r=\eta_0 \tag{3.42}$$

Now, making use of (3.38) to separate out the component of η_2 which refers to the change of shape, Δ_2 say,

$$\frac{\partial \Psi}{\partial r} - \frac{1}{\eta_0^2}\frac{d\eta_0}{d\theta}\frac{\partial \Psi}{\partial \theta} = \Delta_2 - \left(\sin\theta - \frac{\cos\theta}{\eta_0}\frac{d\eta_0}{d\theta}\right)V_1 \quad \text{at } r=\eta_0 \tag{3.43}$$

To solve (3.24), (3.25) and (3.43) is in general quite difficult and so an approximation is made. The interface is closely elliptically in shape. Choosing the ellipse

$$\frac{x^2}{4R_0^2} + \frac{y^2}{3R_0^2} = 1 \tag{3.44}$$

the y intercepts of the ellipse and the interface agree, while the x intercepts are 2 and 2.09 respectively. It turns out that 0.1 is an upper bound on the difference in radius between the ellipse and the interface. The foci of the ellipse correspond to the position of the line vortices. It is important to have the shape very accurately approximated near the stagnation points since any deviations near them lead to changes in the direction of the velocity.

Introducing a conformal mapping which corresponds to introducing elliptic coordinates, leads to

$$z = x + iy = R_0 \cosh w = R_0 \cosh (u + iv)$$

or

$$\frac{x}{R_0} = \cosh u \cos v \quad ; \quad \frac{y}{R_0} = \sinh u \sin v \qquad (3.45)$$

Taking $u = \alpha$, where $\cosh^2 \alpha = 4$ (or $\sinh^2 \alpha = 3$) leads to the elliptic equation (3.44). Figure 3.4 shows the details of the mapping. Since the mapping is conformal, (3.24) and (3.25) must be satisfied in the rectangles in the w plane defined by $\alpha \leq u \leq \infty$, $-\pi \leq v \leq \pi$ and $0 \leq u \leq \alpha$, $-\pi \leq v \leq \pi$ respectively. The kinematic condition (3.43) transforms as follows.

$$\frac{\partial \Psi}{\partial u} = \frac{R_0^2}{\eta_0} 2\sqrt{3} \frac{\partial \Psi}{\partial r} + \frac{\sin\theta \cos\theta}{2\sqrt{3}} \frac{\partial \Psi}{\partial \theta} \quad \text{at } r = \eta_0 \qquad (3.46)$$

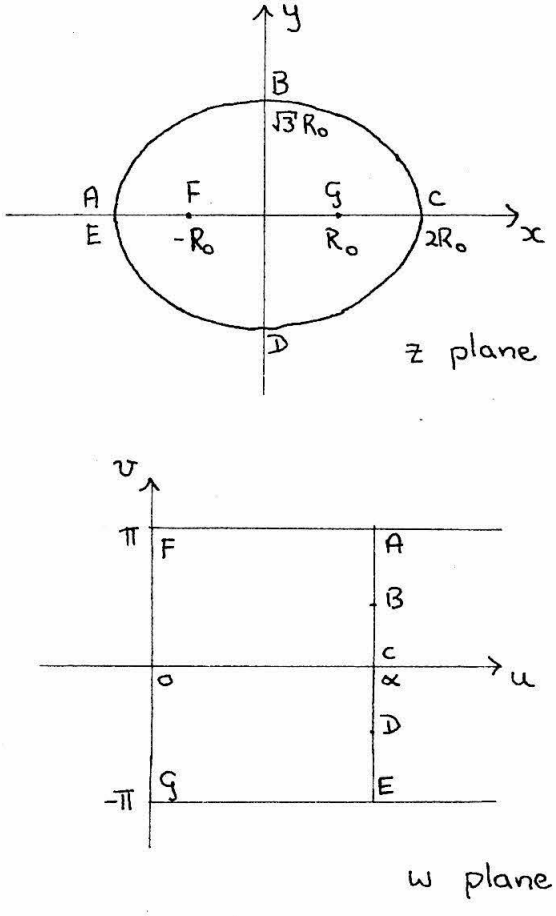

Figure 3.4

where

$$\eta_0^2\left(\frac{\cos^2\theta}{4} + \frac{\sin^2\theta}{3}\right) = R_0^2 \tag{3.47}$$

Now, since

$$\frac{1}{\eta_0}\frac{d\eta_0}{d\theta} = -\frac{\eta_0^2}{R_0^2}\frac{\sin\theta\cos\theta}{12.} \tag{3.48}$$

then

$$\frac{\partial\Psi}{\partial r} - \frac{1}{\eta_0^2}\frac{d\eta_0}{d\theta}\frac{\partial\Psi}{\partial\theta} = \frac{\eta_0}{2\sqrt{3}R_0^2}\frac{\partial\Psi}{\partial u} \qquad \text{at } u=\alpha$$

and the kinematic condition can be written

$$\frac{\partial\Psi}{\partial u} = 2\sqrt{3}\,\frac{R_0^2}{\eta_0}\left[\Delta_2 + \left(\frac{1}{\eta_0}\frac{d\eta_0}{d\theta}\cos\theta - \sin\theta\right)V_1\right] \quad \text{at } u=\alpha \tag{3.49}$$

Using the symmetry,

$$\Psi(u,\pi) = \Psi(u,-\pi) \tag{3.50}$$

the solution to Laplace's equation is easily found.

$$\Psi^\circ = \sum_{n=0}^{\infty} e^{n(\alpha-u)}\left[\alpha_n^\circ \cos n v + \beta_n^\circ \sin n v\right] \tag{3.51}$$

This satisfies the requirement that the velocity vanishes as $u \to \infty$. The inside region needs an additional requirement

at $u=0$ to determine the solution to Laplace's equation. This is supplied by

$$\Psi^I(-u,-v) = \Psi^I(u,v) \tag{3.52}$$

and the solution is

$$\Psi^I = \sum_{n=0}^{\infty} \left(\alpha_n^I \frac{\cosh nu}{\sinh n\alpha} \cos nv + \beta_n^I \frac{\sinh nu}{\cosh n\alpha} \sin nv \right) \tag{3.53}$$

Since $\frac{\partial \Psi^o}{\partial u} = \frac{\partial \Psi^I}{\partial u}$ at $u=\alpha$, by (3.49),

$$\alpha_n^I = -\alpha_n^o \quad , \quad \beta_n^I = -\beta_n^o \tag{3.54}$$

Finally, to solve for α_n^o, β_n^o the dynamic condition or pressure balance must be considered at the boundary.

$$\frac{P_o}{\rho_o} + \frac{\partial \Phi^o}{\partial t} + \frac{1}{2}\left(\frac{\partial \Phi^o}{\partial x}\right)^2 + \frac{1}{2}\left(\frac{\partial \Phi^o}{\partial y}\right)^2 + gy = 0 \tag{3.55}$$

$$\frac{P_I}{\rho_I} + \frac{\partial \Phi^I}{\partial t} + \frac{1}{2}\left(\frac{\partial \Phi^I}{\partial x}\right)^2 + \frac{1}{2}\left(\frac{\partial \Phi^I}{\partial y}\right)^2 + gy = \frac{C}{\rho_I} \tag{3.56}$$

(3.55) is for the flow outside evaluated at the boundary, while (3.56) is for the flow inside evaluated at the boundary. To consider the lowest order terms in (3.55) and (3.56), $\left(\frac{\partial \Phi_0}{\partial x}\right)^2 + \left(\frac{\partial \Phi_0}{\partial y}\right)^2$ must be expressed in the elliptic coordinates. From (3.22)

$$\frac{\partial \Phi_0}{\partial x} = \frac{\Gamma}{2\pi}\left\{\frac{-y}{(x-R_0)^2+y^2} + \frac{y}{(x+R_0)^2+y^2}\right\}; \quad \frac{\partial \Phi_0}{\partial y} = \frac{\Gamma}{2\pi}\left\{\frac{x-R_0}{(x-R_0)^2+y^2} - \frac{x+R_0}{(x+R_0)^2+y^2}\right\}$$

$$\left(\frac{\partial \Phi_0}{\partial x}\right)^2 + \left(\frac{\partial \Phi_0}{\partial y}\right)^2 = \frac{\Gamma^2}{16\pi^2 R_0^2} \frac{e^{x/R_0} - 2 + e^{-x/R_0}}{x^2/R_0^2} \tag{3.57}$$

where use is made of

$$y^2 = -x^2 - R_0^2 + 2xR_0\left(\frac{1+e^{-x/R_0}}{1-e^{-x/R_0}}\right) \tag{3.58}$$

Similarly, from (3.23)

$$\Phi_1 = \frac{\Gamma^2}{16\pi^2 R_0^2}\left[\frac{e^{x/R_0} + e^{-x/R_0}}{2} - \frac{e^{x/R_0} - e^{-x/R_0}}{2x/R_0} - 1\right] \tag{3.59}$$

Now,

$$e^{x/R_0} + e^{-x/R_0} - 2 = 2\sum_{p=1}^{\infty} \frac{1}{(2p)!}\left(\frac{x}{R_0}\right)^{2p} \tag{3.60}$$

$$\frac{e^{x/R_0} - e^{-x/R_0}}{x/R_0} = 2\sum_{p=0}^{\infty} \frac{1}{(2p+1)!}\left(\frac{x}{R_0}\right)^{2p} \tag{3.61}$$

Evaluating (3.60) and (3.61) in elliptic coordinates (see (3.45)) at $u=\alpha$ and noting

$$\cos^{2p} v = \frac{1}{2^{2p-1}} \sum_{K=0}^{p} \frac{(2p)!}{(2p-k)!\,k!} \cos 2(p-k)v \left[1 - \frac{\delta_{kp}}{2}\right]$$

gives (collecting together (3.57), (3.59) and (3.60), (3.61))

$$S \equiv \Phi_1 + \frac{1}{2}\left(\frac{\partial \Phi_0}{\partial x}\right)^2 + \frac{1}{2}\left(\frac{\partial \Phi_0}{\partial y}\right)^2$$

$$= \frac{T^2}{16\pi^2 R_0^2}\left[4\sum_{p=1}^{\infty} p \sum_{m=1}^{p} \frac{\cos 2m\upsilon}{(p-m)!\,(p+m)!} + \sum_{p=1}^{\infty} \frac{1}{p}\frac{1}{(2p-1)}\right.$$

$$\left.\sum_{m=1}^{\infty} \frac{\cos 2m\upsilon}{(p+m-1)!\,(p-m-1)!}\right] \qquad (3.62)$$

The lowest order terms of (3.55) and (3.56) give

$$\frac{P_0}{\rho_0} + \Phi_1 + \Psi^0 + \frac{1}{2}\left(\frac{\partial \Phi_0}{\partial x}\right)^2 + \frac{1}{2}\left(\frac{\partial \Phi_0}{\partial y}\right)^2$$

$$+ \sqrt{3}\, g R_0 \sin\upsilon = 0 \qquad (3.63)$$

$$\frac{P_I}{\rho_I} + \Phi_1 + \Psi^I + \frac{1}{2}\left(\frac{\partial \Phi_0}{\partial x}\right)^2 + \frac{1}{2}\left(\frac{\partial \Phi_0}{\partial y}\right)^2$$

$$+ \sqrt{3}\, g R_0 \sin\upsilon = \frac{C}{\rho_I} \qquad (3.64)$$

The pressure balance at the interface gives $P_0 = P_I$ or

$$\rho_0 \Psi^0 - \rho_I \Psi^I + C + \sqrt{3}\,\Delta\rho\, g R_0 \sin\upsilon + \Delta\rho\, S = 0 \qquad (3.65)$$

The expressions for Ψ^0, Ψ^I ((3.51), (3.53)) can be substituted into (3.65) and the coefficients of $\sin n\upsilon$, $\cos n\upsilon$ set to zero. Thus

$$\beta_1^0 = -\frac{\sqrt{3}\,\Delta\rho}{\rho_0 + \frac{\sqrt{3}}{2}\rho_I}\, g R_0 \tag{3.66}$$

and all other $\beta_n^0 = 0$.

$$\alpha_{2n}^0\left(\rho_0 + \rho_I \frac{\cosh 2n\alpha}{\sinh 2n\alpha}\right) = -\frac{\Delta\rho\,\Gamma^2}{16\pi^2 R_0^2}\left[\sum_{p=n}^{\infty} \frac{4p}{(p-n)!\,(p+n)!}\right.$$
$$\left. + \sum_{p=n+1}^{\infty} \frac{1}{p}\frac{1}{(2p-1)}\frac{1}{(p+n-1)!}\frac{1}{(p-n-1)!}\right] \tag{3.67}$$

and all odd α_n^0 vanish. The constant term is determined by mass conservation and is not important in calculating the velocity or the shape of the interface.

The conformal mapping is singular at the position of the line vortices. The velocity obtained from the solution must be finite at these positions. The derivatives of $\overline{\Psi}^I$ evaluated at $u = \xi << \alpha$, $v = -\pi$, (from (3.53)) are

$$\frac{\partial \overline{\Psi}^I}{\partial u} = \sum_{n=1}^{\infty} 2n\,\alpha_{2n}^I \frac{\sinh 2n\xi}{\sinh 2n\alpha} \tag{3.68}$$

$$\frac{\partial \overline{\Psi}^I}{\partial v} = -\beta_1^I \frac{\sinh \xi}{\cosh \alpha} \tag{3.69}$$

The velocity components in physical space are determined by (see Figure 3.2)

$$\frac{d\overline{\Psi}^I}{dz} = u_I + i v_I = \frac{dw}{dz}\left(\frac{\partial \overline{\Psi}^I}{\partial u} - i\frac{\partial \overline{\Psi}^I}{\partial v}\right) \tag{3.70}$$

From (3.45), $\frac{dw}{dz} = -\frac{1}{R_0}\frac{1}{\sinh\varepsilon}$ and so using (3.68) and (3.69) in the limit $\varepsilon \to 0$

$$u_1 = -\frac{1}{R_0}\sum_{n=1}^{\infty} 4n^2 \alpha_{2n}^{I} / \sinh 2n\alpha \qquad (3.71)$$

$$V_1 = -\frac{1}{R_0}\beta_1^{I}/2. = -\frac{\sqrt{3}}{2}\frac{\Delta\rho}{\rho_0 + \frac{\sqrt{3}}{2}\rho_I} g \qquad (3.72)$$

β_1^{I} is known from (3.54) and (3.66).

It is now possible to calculate the change in the shape of the interface, i.e. Δ_2. From (3.49),

$$\Delta_2 = \frac{\eta_0}{2\sqrt{3}R_0^2}\frac{\partial \Psi^0}{\partial u} + V_1\left(\sin\theta + \frac{\eta_0^2}{R_0^2}\frac{\sin\theta\cos^2\theta}{12}\right)$$

$$\text{at} \quad u = \alpha \qquad (3.73)$$

Using (3.51) and (3.47), this becomes

$$\Delta_2 = -\frac{1}{(3\cos^2\theta + 4\sin^2\theta)^{1/2}}\left[\frac{1}{R_0}\sum_{n=1}^{\infty} 2n\alpha_{2n}^{0}\cos 2nv + \frac{1}{R_0}\beta_1^{0}\sin v\right]$$

$$+ V_1\sin\theta\left[1 + \frac{\cos^2\theta}{3\cos^2\theta + 4\sin^2\theta}\right] \qquad (3.74)$$

The mapping gives $\sin v = 2\sin\theta/(3\cos^2\theta + 4\sin^2\theta)^{1/2}$ and (3.72) and (3.66) leads to

$$\Delta_2 = -\frac{2}{(3\cos^2\theta + 4\sin^2\theta)^{1/2}}\frac{1}{R_0}\sum_{n=1}^{\infty} n\,\alpha_{2n}^{0}\cos 2nv \qquad (3.75)$$

The change in shape, Δ_2, is shown as a function of θ in Figure 3.5. From this it is easy to see that the oval flattens out. For the Boussinesq approximation this effect will be negligible (since Δ_2 does not depend on g) and the shape will remain essentially unchanged for small enough times. The downward velocity is changed by

$$V = V_0 - \frac{\sqrt{3}}{2} \frac{\Delta\rho}{\rho_0 + \frac{\sqrt{3}}{2}\rho_I} gt \qquad (3.76)$$

and the agreement with (3.10) is good. Saffman's model is therefore accurate for small times (the corresponding C is in this case 1.155).

In the next section, a macroscopic model is developed which continues the behaviour established here for small times and it is soon obvious that a detrainment filament forms at the rear stagnation point. The model is extended to include the effects of the tail.

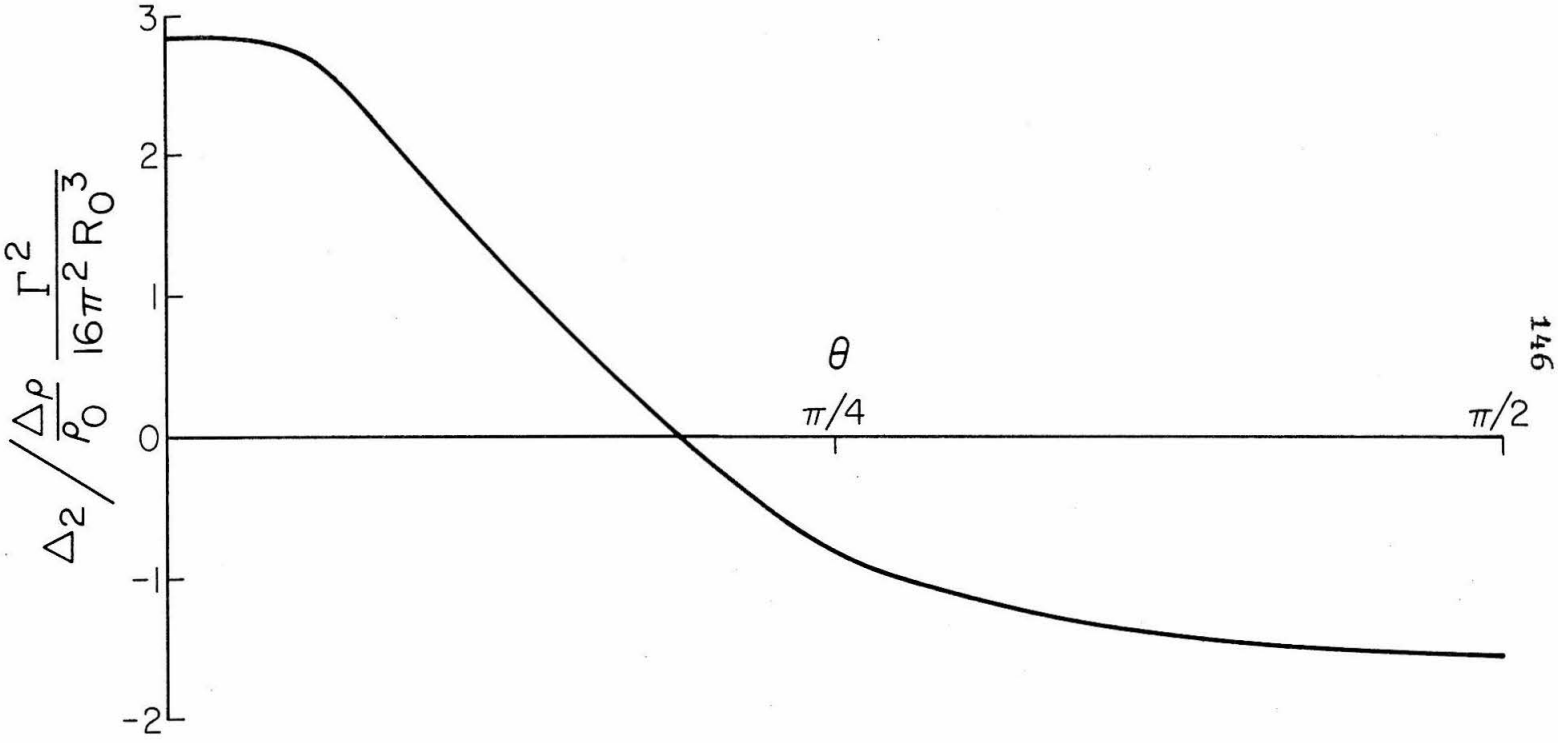

The initial radial acceleration of the interface as a function of angle, θ

Figure 3.5

III. A MACROSCOPIC MODEL

The basic approach in this section is to determine the vorticity generated by the constant density difference at the interface making a simple assumption about the interface shape. The equation governing this vorticity creation in the Boussinesq approximation is

$$\frac{\partial \omega}{\partial t} + \nabla \cdot (\vec{u}\omega) = -\frac{\nabla \rho}{\rho_0} g \sin\phi \qquad (3.77)$$

The problem is considered two dimensional and so $\vec{u} = (u_x, u_y, 0)$, $\vec{\omega} = (0,0,\omega)$ where y is a coordinate in the vertical direction and ϕ is the angle between the normal to the interface and the y-axis. Following Crow (1974), (3.77) is integrated in a direction normal to the interface.

$$\frac{\partial \gamma}{\partial t} + \frac{\partial}{\partial \ell}(q\gamma) = -\frac{\Delta \rho}{\rho_0} g \sin\phi(\ell) \qquad (3.78)$$

where γ is the strength of the vortex sheet at the interface and ℓ is a coordinate along the sheet. The tangential velocity to the sheet is given by q. Crow (1974) considers this equation but neglects the time derivative. By considering the full equation, the initial time behaviour can be found which agrees with the results obtained in the previous section.

The simplest model is to consider the interface as circular with radius, $\sqrt{3}\,R_0$, where $2R_0$ is the initial

separation distance between the line vortices. Choosing a coordinate system fixed with the circle and with the origin at the center of the circle, the downward velocity is determined by the requirement that the front stagnation point has no vertical motion. Thus the vertical velocity component at the front stagnation point is added as a translational velocity to keep the coordinate system fixed with the circular interface. The trailing line vortices may move relative to the circle.

In more detail, the flow field is considered as comprising of two parts, that due to the trailing vortices, $\vec{u}_T$, and that due to the vortex sheet, $\vec{u}_\gamma$. Figure 3.6 shows the coordinates and variables used. If the vortex sheet is discretised into equal angular segments, then the velocity $\vec{u}_\gamma$ can be calculated by the trapezoidal rule (see Chapter 2, section III for details). Thus

$$\gamma_i = \gamma(i\Delta\theta) \qquad i = 0, 1, \ldots N-1 \,, \; N\Delta\theta = 2\pi$$

and

$$u_{\gamma x} = -\frac{1}{2\pi} \sum_{\substack{j=0 \\ j\neq i}}^{N-1} \frac{\gamma_j h \,(y_i - y_j)}{(x_i - x_j)^2 + (y_i - y_j)^2} \tag{3.79}$$

$$u_{\gamma y} = \frac{1}{2\pi} \sum_{\substack{j=0 \\ j\neq i}}^{N-1} \frac{\gamma_j h \,(x_i - x_j)}{(x_i - x_j)^2 + (y_i - y_j)^2} \tag{3.80}$$

where $h = a\Delta\theta$ and a is the radius of the circle ($a = \sqrt{3}R_o$).

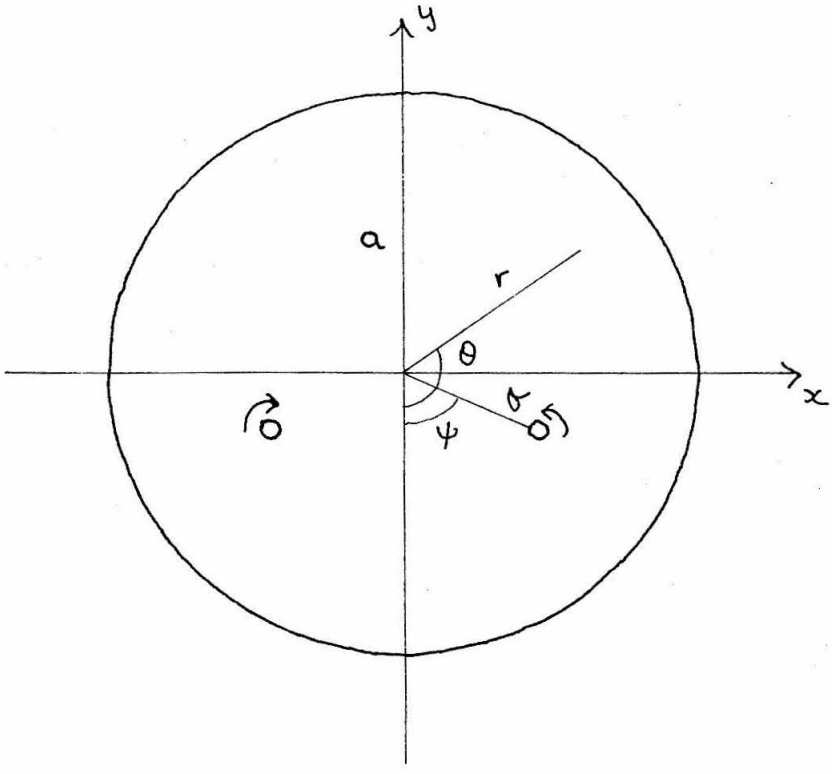

Coordinate system for macroscopic model without tail.

Figure 3.6

The downward velocity component at the front stagnation point is

$$V = -u_{\gamma_y}(o) + \frac{\Gamma}{\pi}\frac{\sigma \sin\psi}{\sigma^2+a^2-2\sigma a\cos\psi} \tag{3.81}$$

The circulation of the line vortices is $\pm\Gamma$. V is the translationary velocity needed to be added to the vertical velocity to make the interface stationary. After noting that $u_{\gamma\theta}$ vanishes at the interface, the asimuthal velocity of the sheet is

$$q(\theta) = V\sin\theta + \frac{\Gamma}{\pi}\frac{\sigma\sin\psi.\sin\theta.(a^2-\sigma^2)}{[\sigma^2+a^2-2a\sigma\cos(\psi-\theta)][\sigma^2+a^2-2\sigma a\cos(\psi+\theta)]} \tag{3.82}$$

The γ_i are obtained by using the leap-frog scheme on (3.78), i.e.

$$\gamma_i\big((k+1)\Delta t\big) = \gamma_i\big((k-1)\Delta t\big) + \frac{\Delta t}{h}\Big[q\big((i+1)\Delta\theta\big)\gamma_{i+1}(k\Delta t) - q\big((i-1)\Delta\theta\big)\gamma_{i-1}(k\Delta t)\Big] - \frac{\Delta\rho}{\rho_o}g\sin(i\Delta\theta) \tag{3.83}$$

Due to symmetry $\gamma_o = \gamma_N = o$. In fact, symmetry implies only half of γ_i need to be calculated, i.e. $\gamma(x,y) = -\gamma(-x,y)$. The velocity components of the line vortices are

$$u_\theta = u_{\gamma\theta}(\sigma,\psi) + \left(V - \frac{\Gamma}{4\pi\sigma\sin\psi}\right)\sin\psi \tag{3.84}$$

$$u_r = u_{\gamma r}(\sigma,\psi) + \left(V - \frac{\Gamma}{4\pi\sigma\sin\psi}\right)\cos\psi \qquad (3.85)$$

The motion of the line vortices relative to the circle can be easily followed.

The procedure then is as follows. Knowing the values of all the quantities at a certain time, an update is obtained by first using (3.83) to get the new γ_i , then V is determined by (3.81) and (3.84), (3.85) means the new position of the trailing vortices can be calculated. Finally, (3.82) gives $q(\theta)$ and the cycle is repeated.

There is an important dimensionless quantity,

$$\beta = \frac{\Delta\rho}{\rho_0}\left(\frac{4\pi}{\Gamma}\right)^2 g R_0^3 \qquad (3.86)$$

which measures the rate of growth of the vorticity at the interface compared to the circulation of the trailing vortices. For $\beta = 0.5$, the downward velocity is shown in Figure 3.7. As a check on the similarity of the shape, the velocity at the back stagnation point is shown. It is clear from the results that fluid will detrain from the circular shape at the back stagnation point, and so the need for a tail is obvious. The straight line represents the result (3.76), showing the model is good for small times at least.

The model is simply modified to allow drainage at the back stagnation by superimposing a triangular tail region

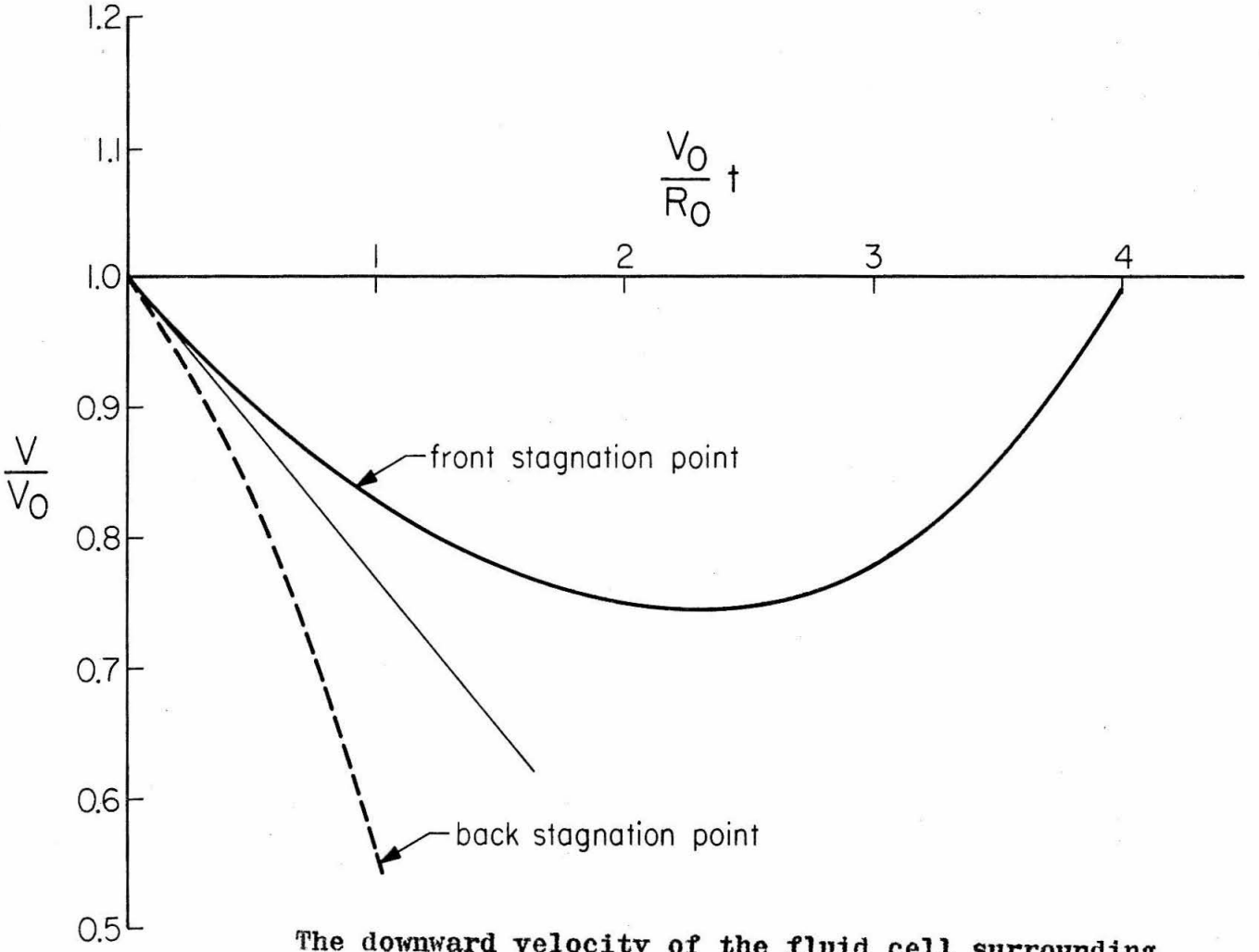

The downward velocity of the fluid cell surrounding the line vortices as a function of time for $\beta = 0.5$ The straight line indicates

Figure 3.7

onto the circular interface. Figure 3.8 gives the details. Since the flow is incompressible, mass conservation requires the circular part of the cell to contract as the tail develops. The vorticity equation (3.78) and its approximation (3.83) will still be used for the circular region and as the radius decreases, γ_i will be kept constant for constant angle, $i\Delta\theta$. The procedure of keeping the value fixed with the mesh point when adjustments to the shape are made, is adopted also for the tail. The width of the tail, which is always calculated to the nearest mesh point, determines the number of mesh points on the sides of the tail, since the total number of mesh points is kept fixed. The same approximation (3.83) is used for the sides of the tail except $\sin(i\Delta\theta)$ is replaced by $\sin\alpha$.

However, there is a complication concerning the vorticity near the vertex of the tail. The vorticity must vanish at the vertex but the tangential velocity q does not. Thus vorticity is convected onto the vertex which contradicts the fact that it is a stagnation point. The leap-frog scheme is not used at the mesh point adjacent to the vertex but rather a simple first order difference in both space and time. Thus vorticity accumulates at this mesh point and not at the vertex. Since an equal but opposite amount of vorticity accumulates on the other side of the tail by symmetry, this accumulation will not have an appreciable effect on the motion of the line vortices.

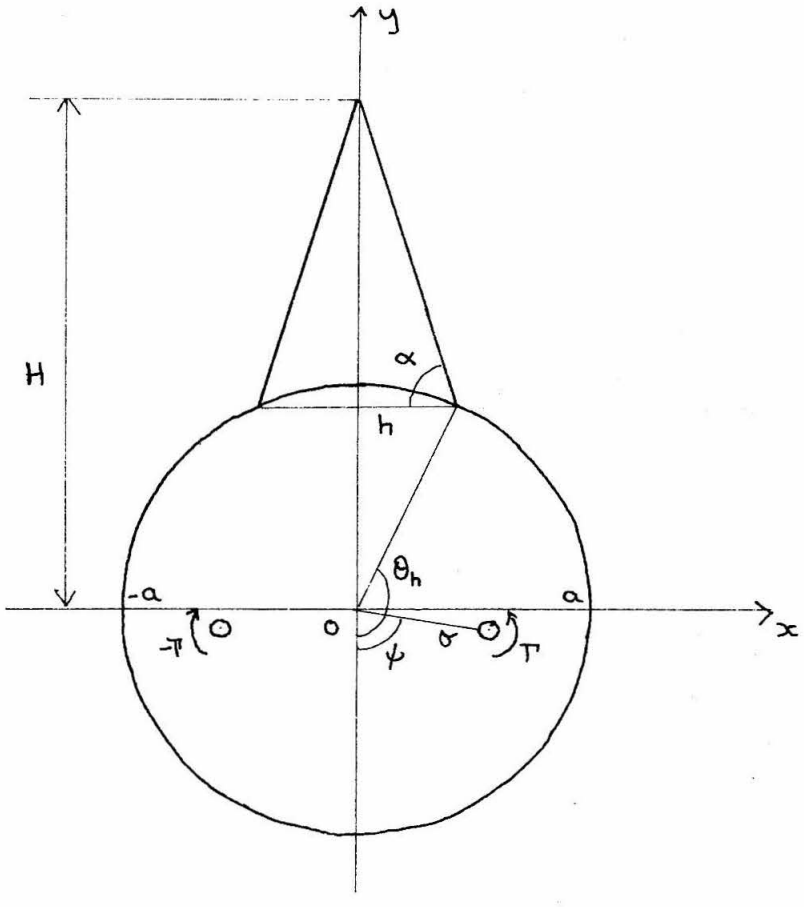

Coordinate System used for macroscopic model including tail region.

Figure 3.8

Solving the vorticity equation is equivalent to satisfying the dynamics of the flow field. The kinematics is satisfied as follows. The front stagnation point is no longer stationary relative to the coordinate system fixed at the center of the circle. The condition there is now

$$V + \frac{da}{dt} = - u_{Ty}(0,-a) - u_{\gamma y}(0,-a) \tag{3.87}$$

The change in radius is determined by

$$\frac{da}{dt} = u_{Tx}(a,0) + u_{\gamma x}(a,0) \tag{3.88}$$

Modifications to the shape are determined by the balance of mass fluxes. The flux into the tail is estimated by

$$2hU \tag{3.89}$$

where

$$U = u_{Ty}(0,a) + u_{\gamma y}(0,a) + V \tag{3.90}$$

The mass lost from the circular region per unit time is

$$- 2a\frac{da}{dt} \sin^{-1}\frac{h}{a} \tag{3.91}$$

Mass conservation implies the approximate equality of (3.89) and (3.91).

$$\frac{h}{a} = \sin\left[-\frac{h}{a} u \left(\frac{da}{dt}\right)^{-1}\right] \qquad (3.92)$$

This equation is solved by Newton's scheme for $\frac{h}{a}$ and thus the width of the tail is known. The height is obtained directly from mass conservation.

$$a^2 \theta_h + aH \sin\theta_h = 3\pi \qquad (3.93)$$

Assuming all values are known at some time level, the values at the next time level are determined as follows. The vorticity is calculated by (3.83) for the circular region of the interface and the appropriate modification is used for the tail region. The change in radius follows from (3.88) and the downward velocity from (3.87). (3.90) and (3.92) determine the width and (3.93) the height of the tail. The trailing vortices are moved forward in time by (3.84) and (3.85), and so the procedure continues.

The only time this procedure is not clear is before the tail has developed. For small times both u and $\frac{da}{dt}$ are small, making the determination of the tail width difficult. An initial expansion in time using the procedure outlined, but without the tail, gives the following.

$$\gamma(\theta)\sqrt{\frac{\Delta\rho}{\rho_0}\,g\frac{R_0}{V_0}} = -\sin\theta\,\tilde{t} + \frac{\sqrt{3}}{2}\sum_{n=1}^{\infty} c_n \sin n\theta\,\tilde{t} + O(\tilde{t}^3) \qquad (3.94)$$

where $\tilde{t} = \frac{V_0}{R_0}t$ and

$$\sum_{n=1}^{\infty} c_n \sin n\theta = \frac{\sin 2\theta}{(4-3\sin^2\theta)^{1/2}}\left[8 - 8\sin^2\theta + 3\sin^4\theta\right]$$

The other variables have the expansions,

$$\frac{a}{R_0} = \sqrt{3} + O(\tilde{t}^3) \qquad (3.95)$$

$$\frac{1}{V_0}\frac{da}{dt} = \frac{\sqrt{3}}{4}\beta\sum_{n=1}^{\infty} c_n \cos\frac{n\pi}{2}\,\tilde{t}^2 + O(\tilde{t}^3) \qquad (3.96)$$

$$\frac{V}{V_0} = 1 - \frac{\beta}{2}\tilde{t} + \frac{\sqrt{3}}{4}\beta\left[\sum_{n=1}^{\infty} c_n - \sum_{n=1}^{\infty} c_n \cos\frac{n\pi}{2}\right]\tilde{t}^2 + O(\tilde{t}^3) \qquad (3.97)$$

$$\frac{u}{V_0} = \frac{\sqrt{3}}{4}\beta\left[\sum_{n=1}^{\infty} c_n - \sum_{n=1}^{\infty} c_n \cos\frac{n\pi}{2} + \sum_{n=1}^{\infty} c_n \cos n\pi\right]\tilde{t}^2 + O(\tilde{t}^3) \qquad (3.98)$$

$$\frac{\sigma}{R_0} = 1 + O(\tilde{t}^3) \qquad (3.99)$$

$$\psi = \frac{\pi}{2} + O(\tilde{t}^3) \qquad (3.100)$$

It is clear that a second order difference scheme must be used to calculate γ_i in order that the correct coefficients in (3.96) and (3.98) will be calculated and hence that (3.92) will have meaning when solved the first time. The $O(\tilde{t})$ term in (3.97) has a numerical coefficient

of 0.5 compared to 0.46 from (3.76) and so the model appears reasonable.

The results are obtained for two values of β , $\beta = 0.5$ $\beta = 1$. The downward velocity as a function of time is shown in Figure 3.9, while the position coordinates of the trailing line vortices are shown in Figure 3.10. The behaviour seems to be that, initially, vorticity is generated at the interface which slows down the trailing vortices descent, but then, as fluid and vorticity are detrained upwards, the trailing vortices are forced together and begin to accelerate downwards.

There is one unpleasant feature of the model. The tail width oscillates rapidly initially but decays to a steady behaviour at about $\frac{tV_0}{R_0} = 1.0$ for $\beta = 0.5$. This oscillation does not appear to affect the downward motion of the cell or the trailing vortices. There is a weak oscillation in the tail height and this confirms the picture that the side of the triangular tail does not deviate very far from the circular arc. The mesh points are thus not being moved very far and so the influence is weak especially since the vorticity has not yet grown significantly in value.

As a final check on the model, a numerical calculation is done based on the method employed by Fink and Soh (1974) and detailed in Chapter 2, Section III. Since there is a creation term in the vorticity equation, circulation is no longer constant along fluid flow and the procedure to

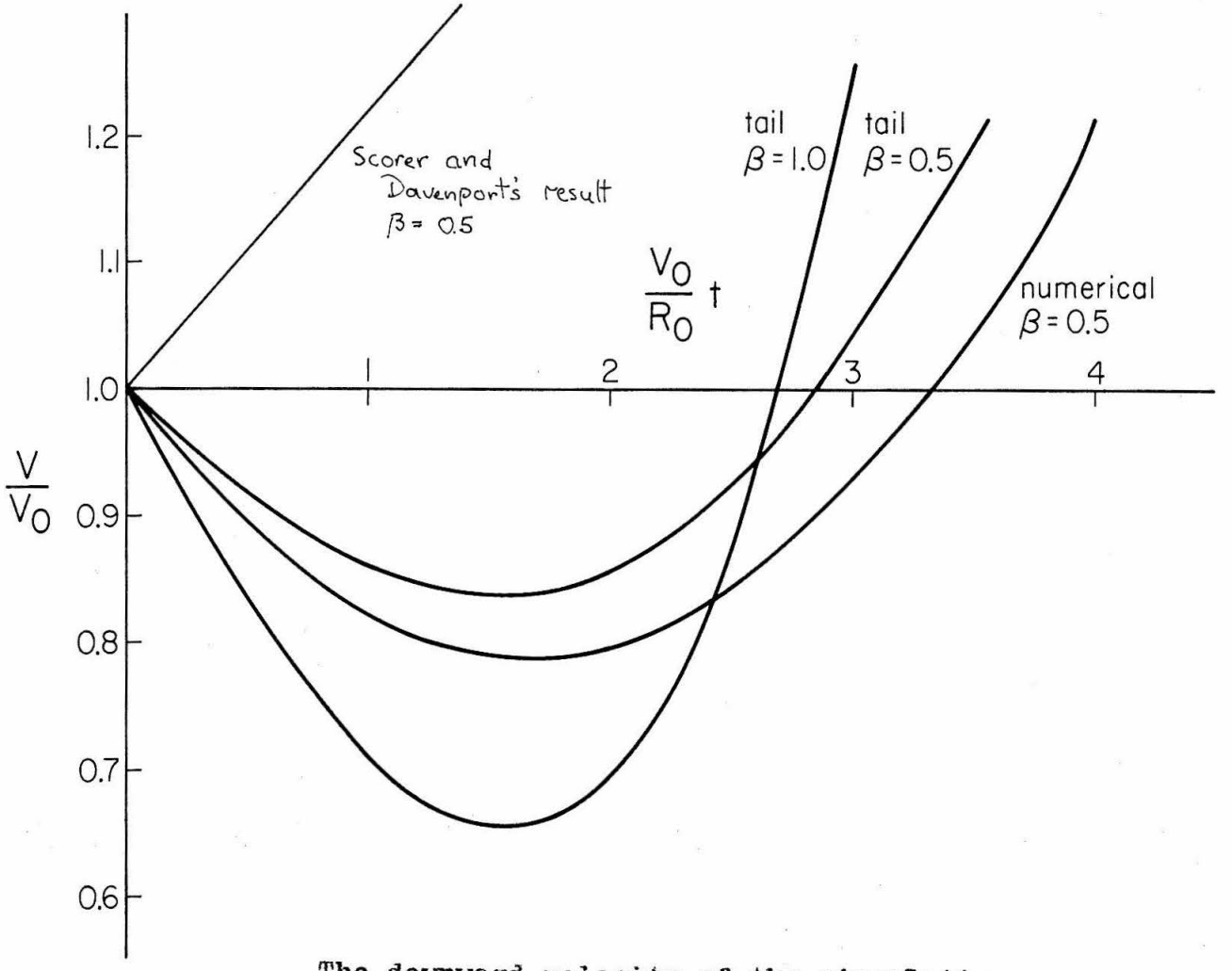

The downward velocity of the circulation cell as a function of time.

Figure 3.9

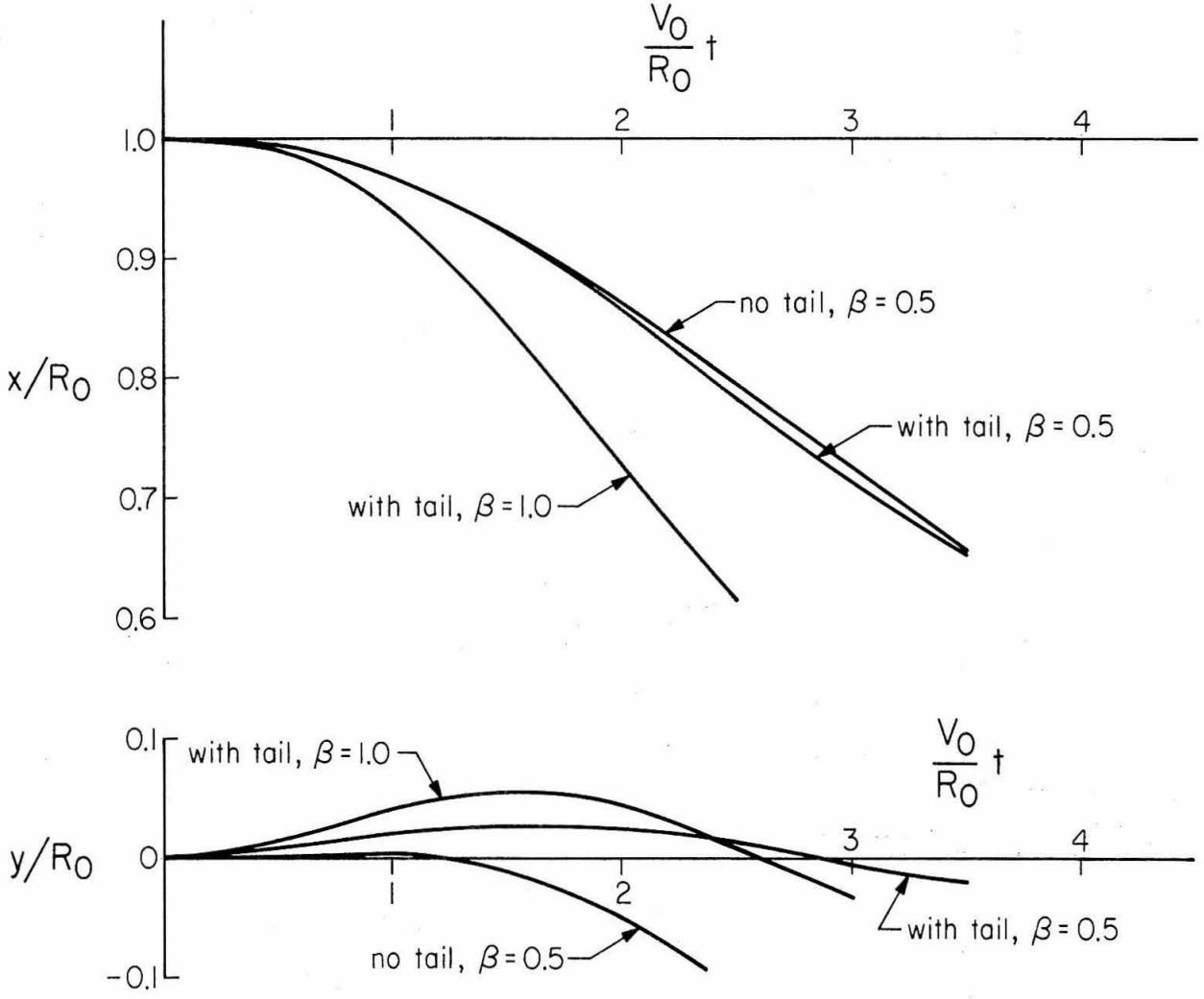

The components of position of the line vortices as functions of time.

Figure 3.10

incorporate this change in circulation, adopted by Hill (1975b), is followed here. From Bjerknes' theorem, the creation of circulation at the interface is described by

$$\frac{D\Gamma}{Dt} = -g\iint_A \frac{1}{\rho}\frac{d\rho}{dx}\,dx\,dy$$

$$= -g\iint_A \frac{1}{\rho}\frac{d\rho}{dn}\sin\theta(\ell)\,dn\,d\ell \qquad (3.101)$$

where $\theta(\ell)$ is the angle between the normal to the interface and the y-axis. This integral can be approximated by

$$\Delta\Gamma_j = -\Delta t\, g\,\frac{\Delta\rho}{\rho}\,\frac{h}{2}\left[\sin\theta_{j+1} + \sin\theta_j\right] \qquad (3.102)$$

where h is the arclength spacing and θ_j is the angle evaluated at the midpoint in arclength of the $j-1^{th}$ and j^{th} mesh point. The method followed is the same as Chapter 2, Section III except that after the redistribution of mesh points, the created vorticity (3.102) is added to the convected circulation at the j^{th} mesh point. As Hill (1975b) found, the results indicated an instability appearing in the tail region. Using the smoothing technique as discussed in Chapter 2, Section III, the numerical method can be employed for longer times but with probable loss in accuracy. However, the results confirm the macroscopic model as being fairly accurate. This is illustrated in the first place by comparing the downward velocity as shown in Figure 3.9 for

$\beta = 0.5$, and then by the series of profiles of the interface as it evolves in time, as shown in Figures 3.11 and 3.12. In the results for the numerical scheme shown in Figure 3.12, there appears to be an attempt for the vorticity in the tail to roll up into another vortex pair. The smoothing introduced unfortunately prevents the description of any details. The dimensions of the interface agree well with the macroscopic model. Thus the macroscopic model is reasonable in describing the large scale motions of the wake. The limiting factor on this model appear to be that, when the vorticity reaches the same order of magnitude of the circulation of the trailing vortices, the discretisation begins to fail. For $\beta = 0.5$, this occurs at about $t = 4\frac{R_o}{V_o}$. This is due to the tail width reaching the size of the radius of the circle and is an obvious failure of the assumed shape.

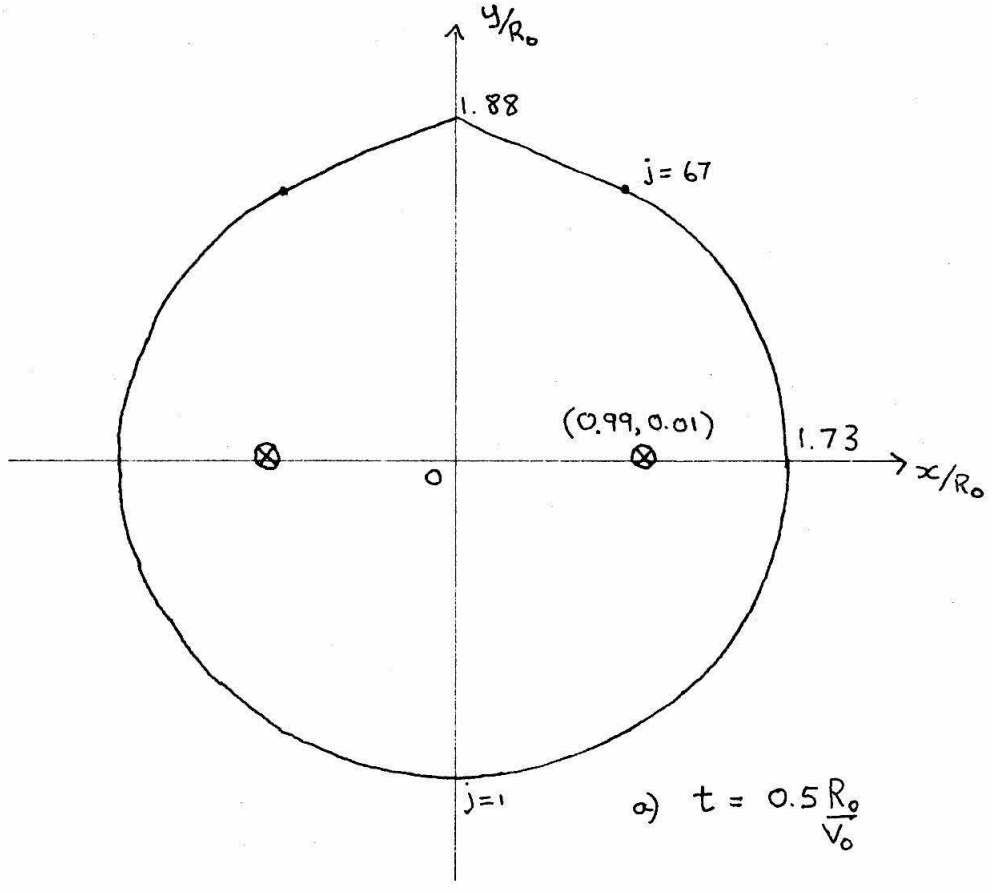

The time evolution of the circulation cell using the macroscopic model with a tail region. There are 81 mesh points on one side.

Figure 3.11

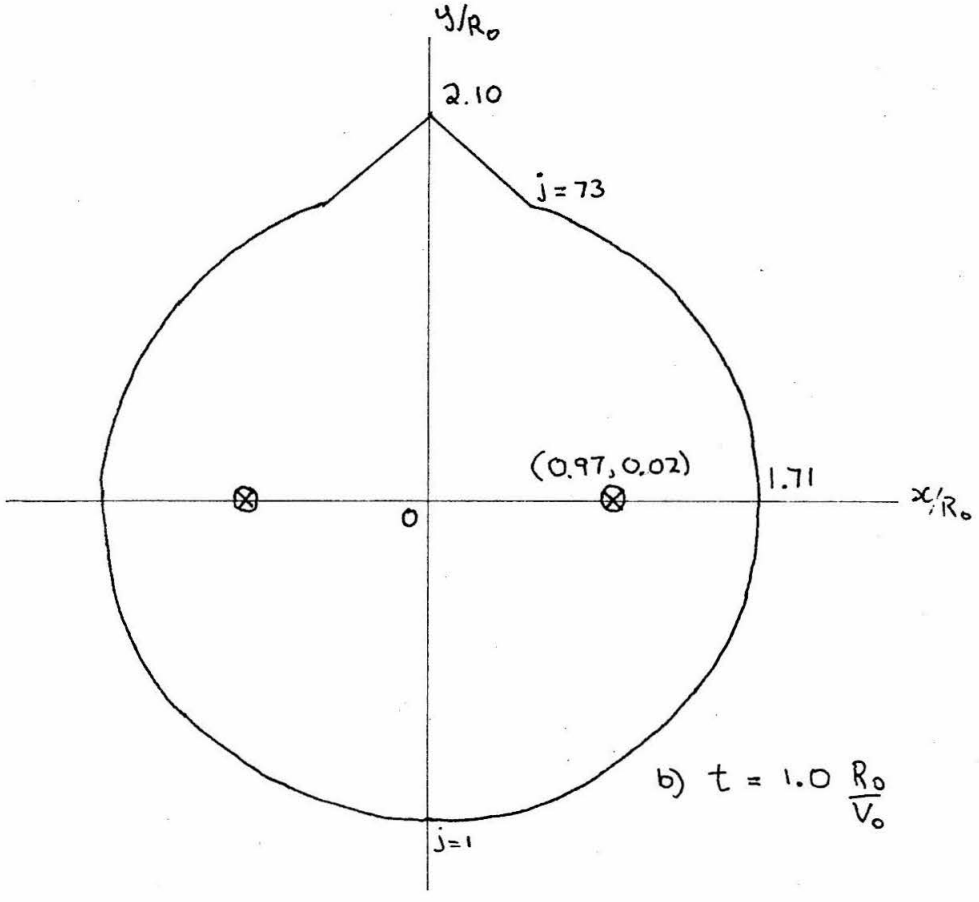

b) $t = 1.0 \frac{R_0}{V_0}$

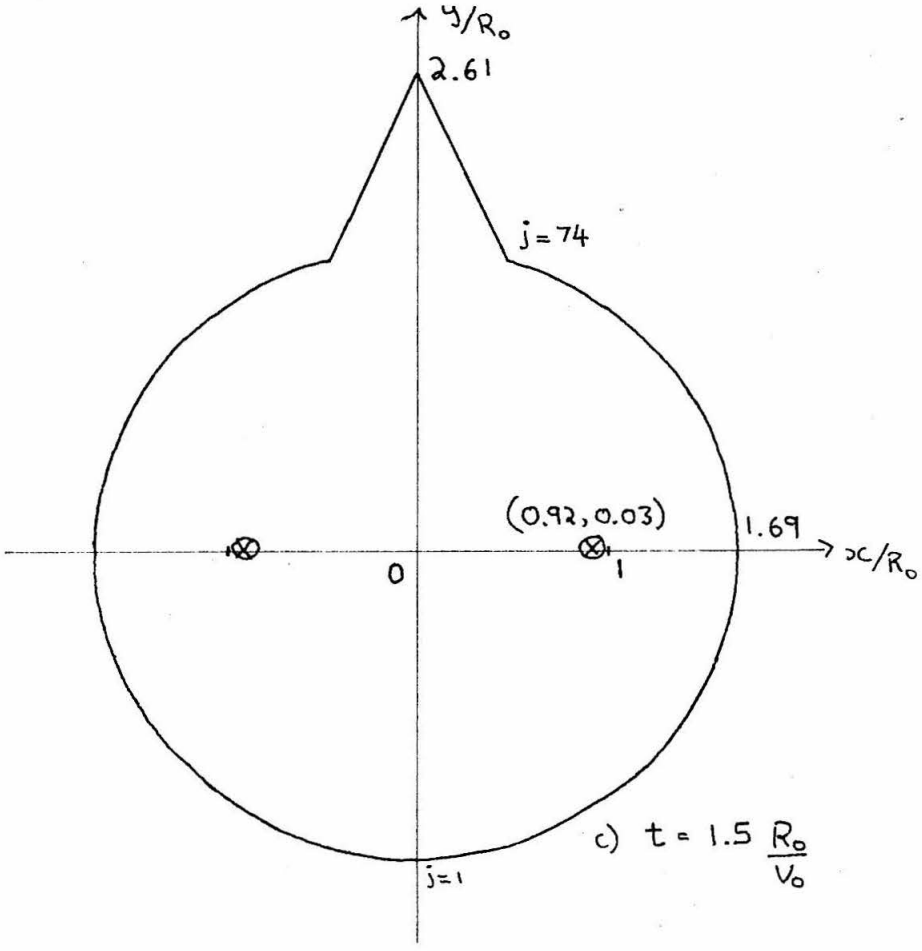

c) $t = 1.5 \frac{R_0}{V_0}$

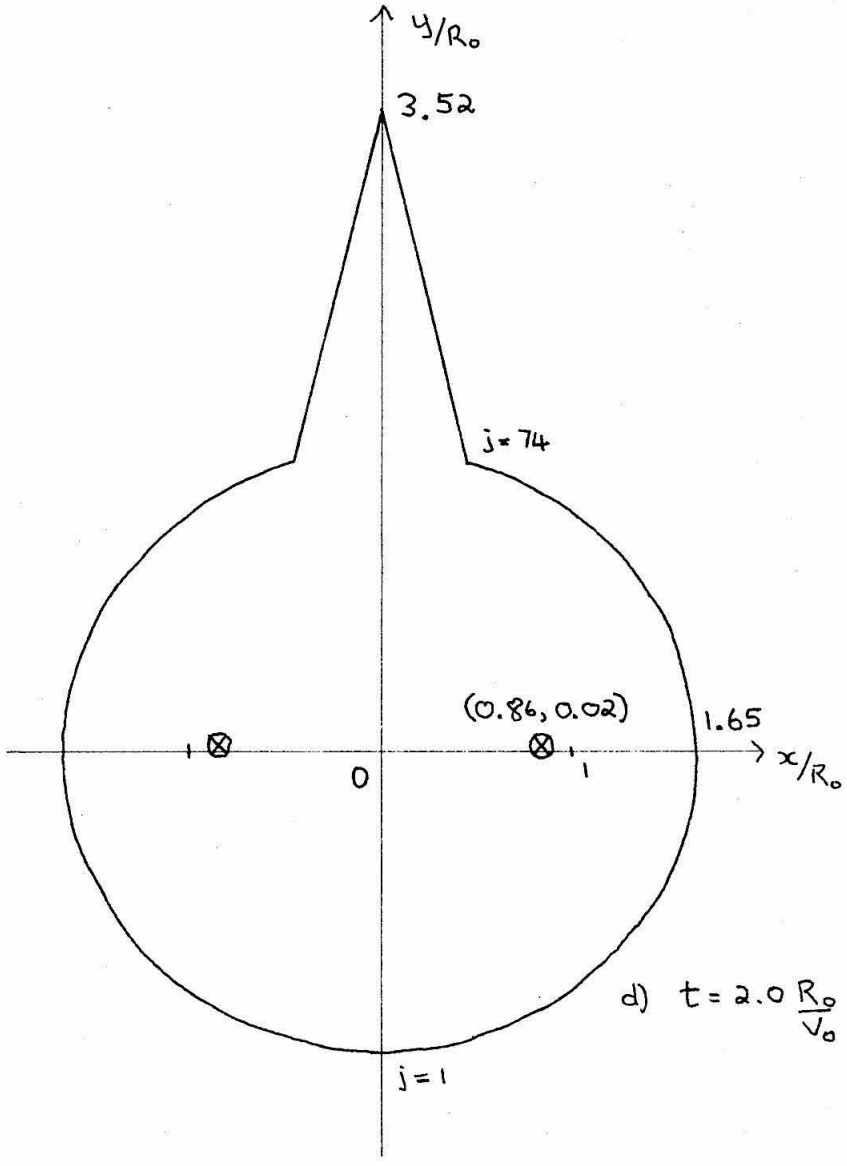
y/R₀
3.52
j = 74
(0.86, 0.02)
1.65
x/R₀
1
0
1
d) t = 2.0 R₀/V₀
j = 1

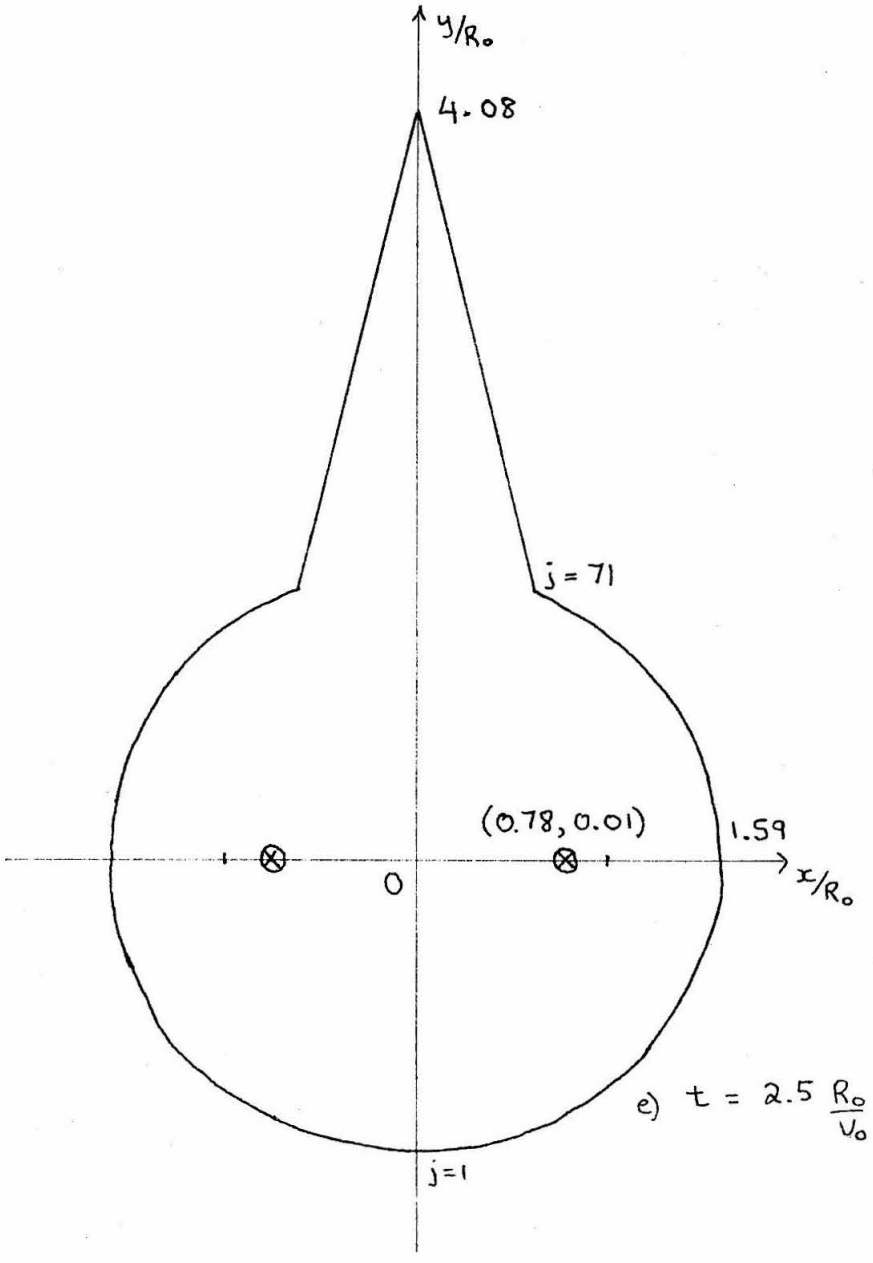

e) $t = 2.5 \frac{R_0}{V_0}$

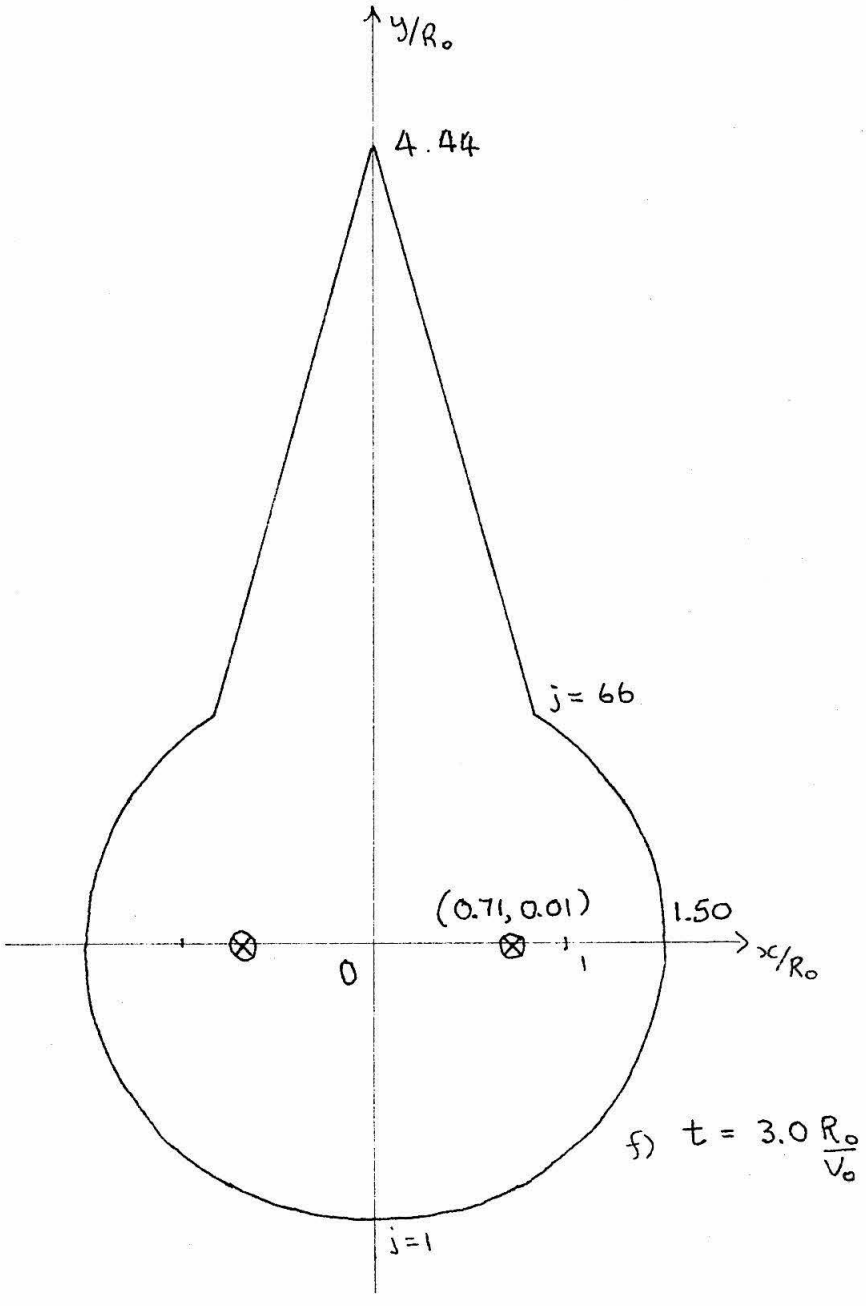

f) $t = 3.0 \frac{R_0}{V_0}$

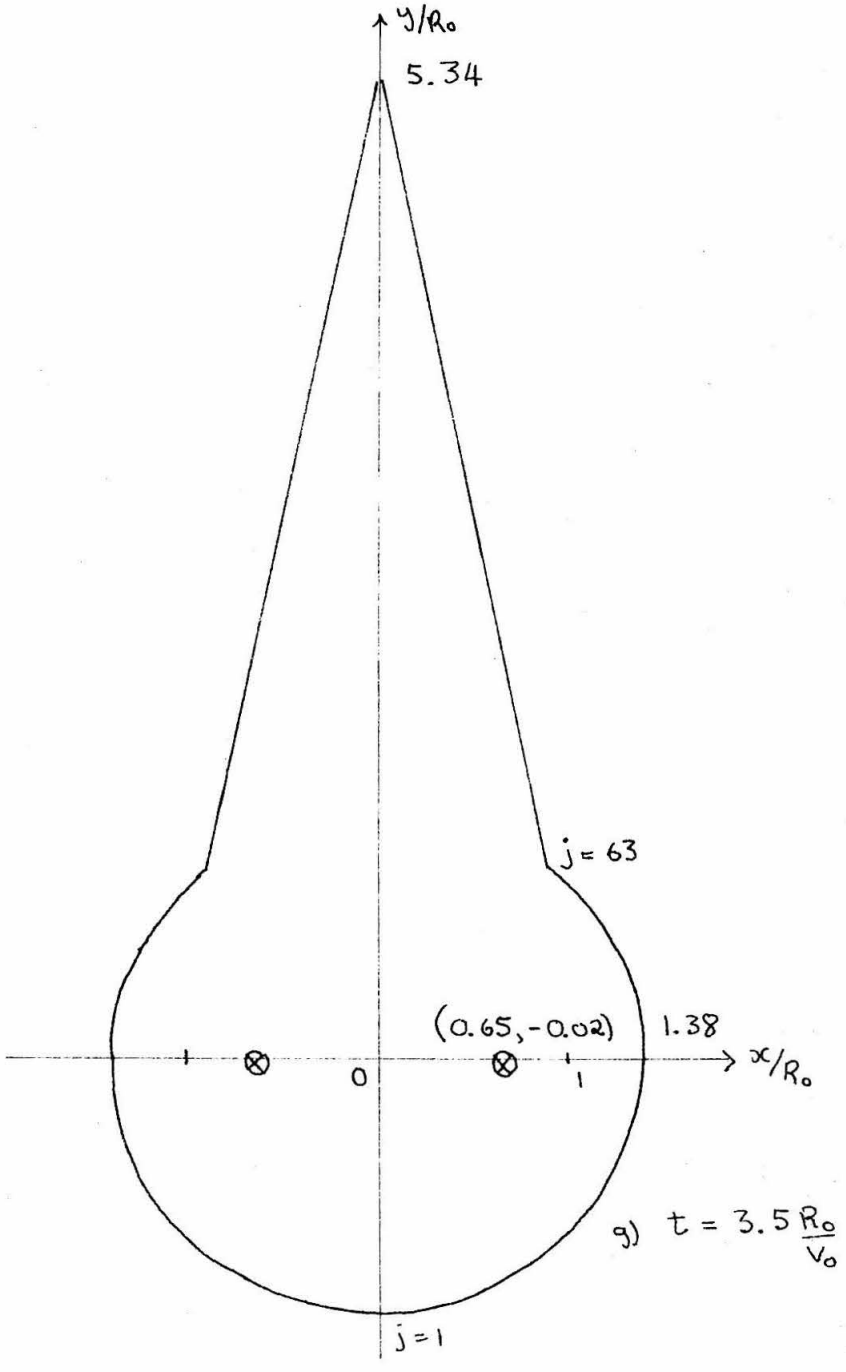

g) $t = 3.5 \frac{R_0}{V_0}$

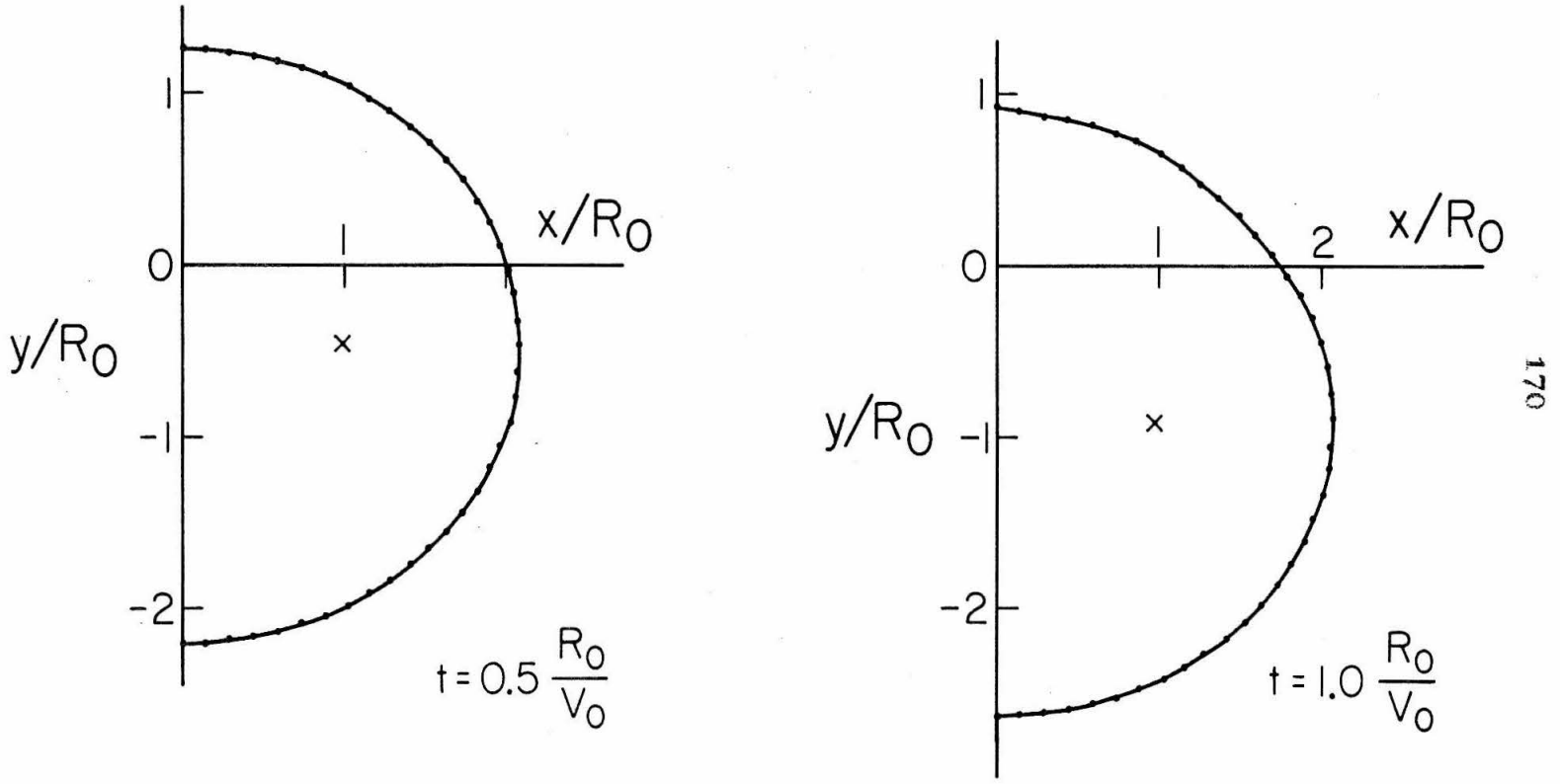

The numerical results for the motion of the circulation cell based on the method of Fink and Soh (1974). There are 41 vortex points along the interface. Time step = 0.01 R_o/V_o

Figure 3.12

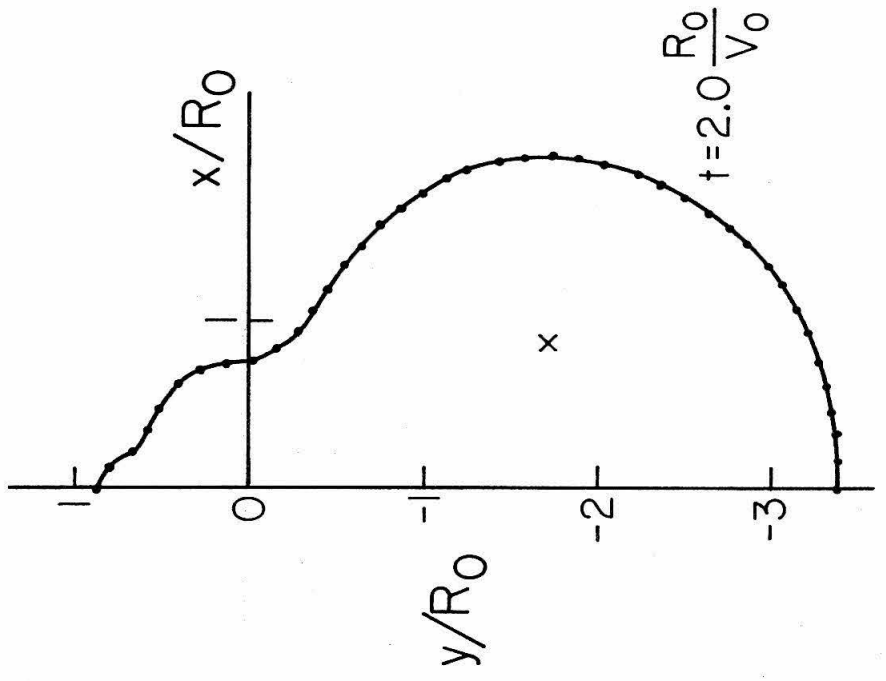
x/R0
1
0
-1
-2
-3
y/R0
t=2.0 R0/V0

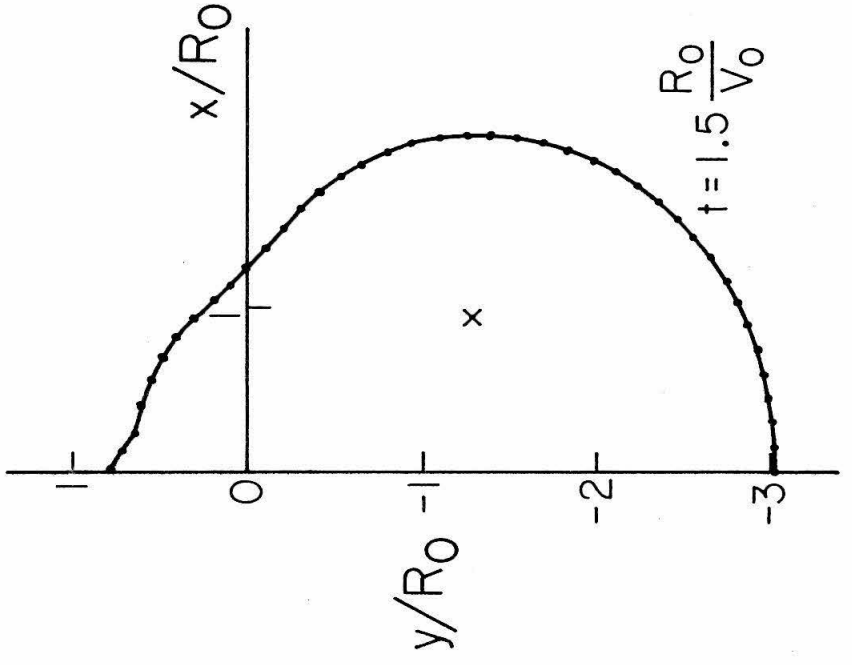
x/R0
1
0
-1
-2
-3
y/R0
t=1.5 R0/V0

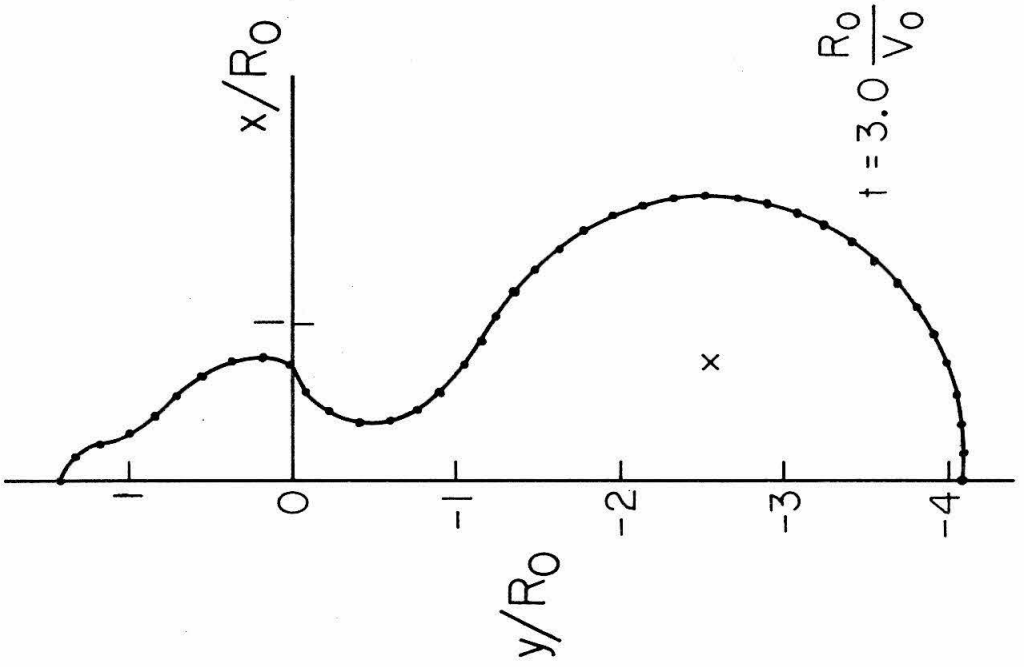
x/R0
1
0
-1
-2
-3
-4
y/R0
t = 3.0 R0/V0

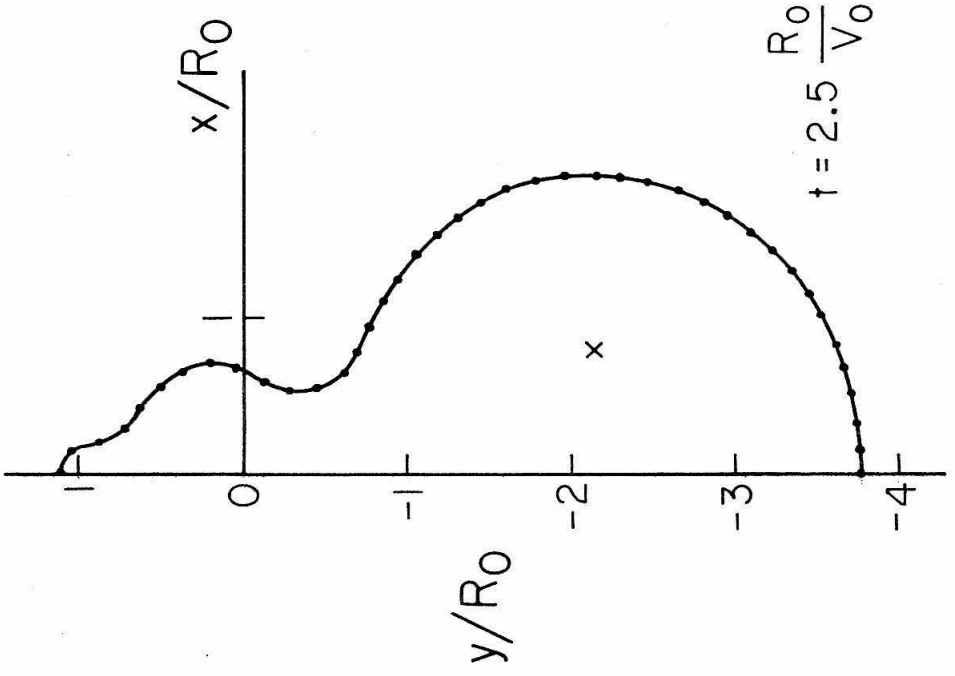
x/R0
1
0
-1
-2
-3
-4
y/R0
t = 2.5 R0/V0

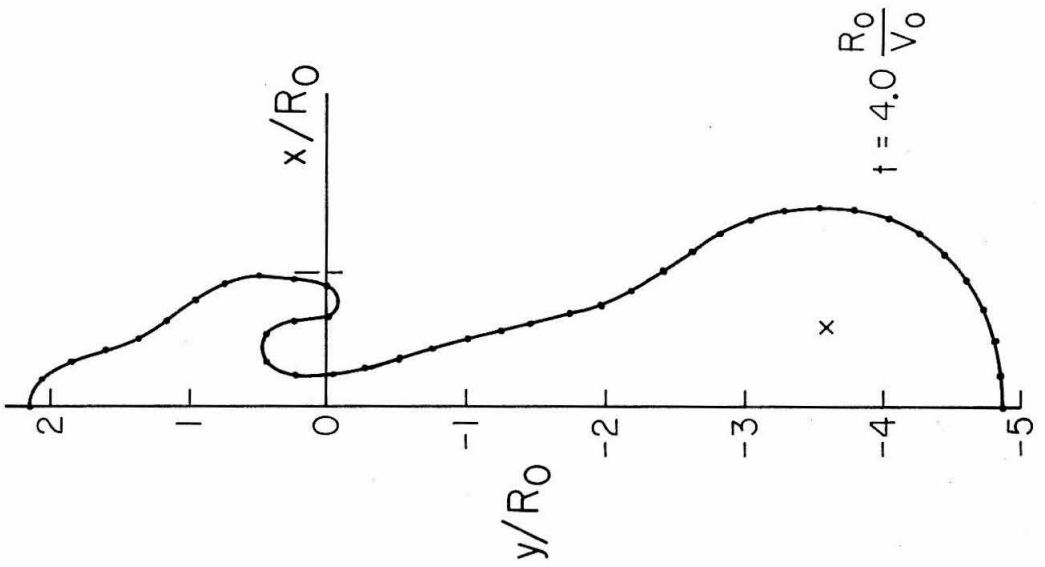
x/R0
y/R0
t = 4.0 R0/V0
2
1
0
-1
-2
-3
-4
-5

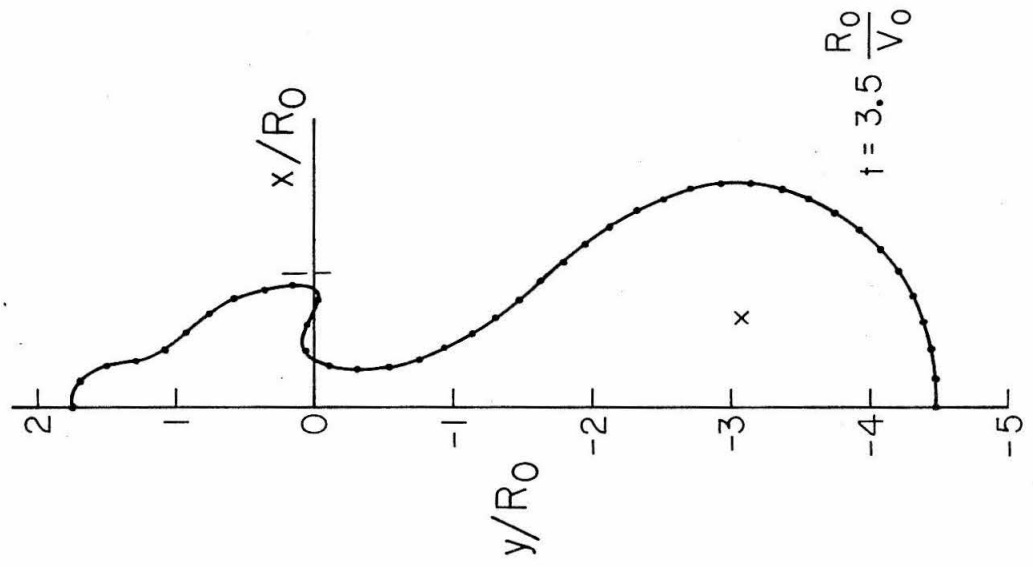
x/R0
y/R0
t = 3.5 R0/V0
2
1
0
-1
-2
-3
-4
-5

Chapter 4

Laser anemometer measurements of trailing vortices in water

By G. R. BAKER, S. J. BARKER, K. K. BOFAH AND P. G. SAFFMAN

Graduate Aeronautical Laboratories, California Institute of Technology, Pasadena

A series of measurements of trailing vortices behind lifting hydrofoils is described. These measurements were made in the Caltech Free-Surface Water Tunnel, using a laser-Doppler velocimeter to measure two components of velocity in the vortex wake. Two different model planforms were tested, and measurements were made at several free-stream velocities and angles of attack for each. Velocity profiles were measured at distances downstream of the model of from five to sixty chord lengths. These measurements are the first results of a continuing experimental programme.

In § 3 of this paper, the theory of trailing vortices is discussed. The effects of 'vortex wandering' upon the measurements are computed, and the corrected results are seen to be in reasonable agreement with the theory.

1. Introduction

There have been numerous recent attempts to measure velocities in trailing vortices, stimulated by interest in the problem of aircraft wake turbulence. Several types of measurements have been made to date. There have been free-flight measurements (Caiger & Gould 1971; Chevalier 1973), in which one aircraft follows another to measure velocities in its wake. These have not yielded accurate results because of the difficulty in locating the vortex cores. There have been wind-tunnel measurements of stagnation pressure (Mason & Marchman 1972), but these are subject to doubt because of probe interference effects. It is questionable whether any material probe can be placed in the core of a small trailing vortex without significantly disturbing the flow. There have also been measurements in tow basins of velocities in the unsteady decaying vortices (Miller & Brown 1971; Lezius 1973). In this case the flow is time dependent, which makes the mean velocity profiles in the vortices difficult to determine.

The only existing measurement technique which can guarantee no disturbance of the flow with high spatial resolution is laser-Doppler anemometry. Recent laser-Doppler velocimeter (LDV) measurements of trailing vortices in a wind tunnel have been reported by Orloff & Grant (1973). In the present experimental programme at Caltech, an LDV is being used to measure axial and tangential velocity profiles in trailing vortices in a water tunnel. The water tunnel has the advantages of high Reynolds numbers at relatively low speeds,

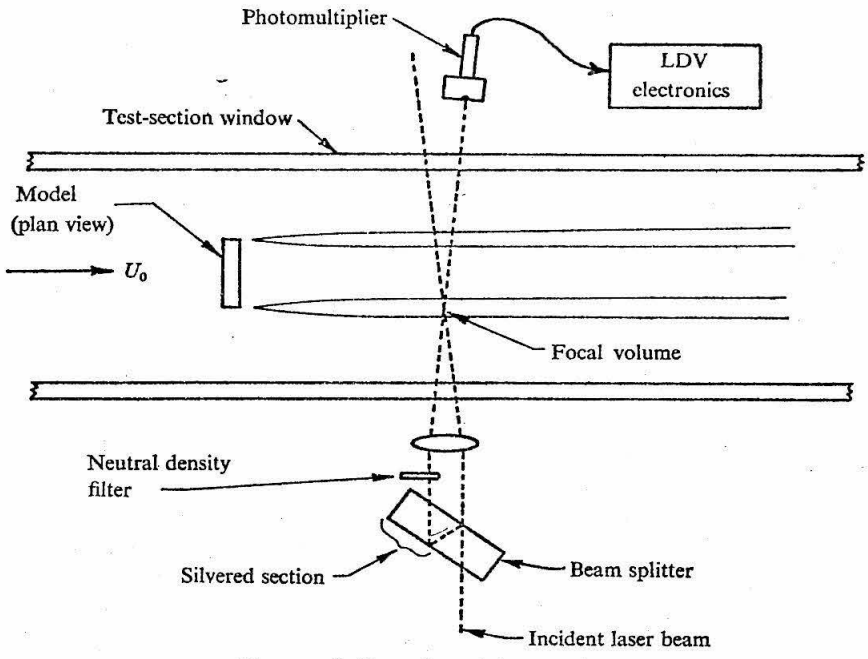

FIGURE 1. Experimental geometry.

and the presence of sufficient light-scattering particles in the water to produce a nearly continuous Doppler signal without 'seeding' the flow with foreign particles. The ease of flow visualization in water makes it possible to measure photographically the position of the vortex and its degree of 'wandering', which will be discussed in § 3.

2. Experimental programme

2.1. *Test facility*

The Caltech Free-Surface Water Tunnel has a test section which is 51 × 51 cm in cross-section and 244 cm long. The maximum flow velocity is 730 cm/s. Velocities between 200 and 300 cm/s correspond to Froude numbers near one and therefore are not usable. The free-stream turbulence level of the tunnel is about 0·5 %. For a complete description of this facility, see Knapp & Levy (1948).

The two hydrofoil models used in this study have a span of 15·2 cm and a chord of 2·46 cm. Both have a symmetric semicircular arc profile, with a maximum thickness of 0·35 cm and a leading-edge radius of 0·08 cm. One of the models has a rectangular planform and the other has a planform with semicircular tips. Both models are mounted horizontally in the tunnel section by means of a thin vertical support strut attached to the centre of the span of the model. Above the water surface, the vertical strut is attached to a mechanism which controls the angle of attack and depth of the model. The model is located near the upstream end of the test section so that measurements can be made at distances of up to sixty chord lengths downstream. (See figure 1.)

2.2. *Laser-Doppler instrumentation*

Use of a laser-Doppler velocimeter (LDV) has several important advantages over conventional techniques in this experiment. Perhaps the most significant is the fact that there is no material probe in the fluid flow, and hence no flow interference. Flow visualization studies suggest that trailing vortices are extremely sensitive to disturbances created by even very small probes. Other advantages of the LDV are its linear response to velocity, its small measuring volume and the ability to measure one velocity component independently of the others.

The LDV used in this experiment is mounted on a traverse which moves the entire optical system with respect to the water tunnel. This LDV operates in the 'local oscillator' mode, whose principle will be described here very briefly. The beam from a 5 mW helium–neon laser is split into two parallel beams by a glass-prism beam splitter which uses partial internal reflexion of the incident beam. One of the beams emerging from the prism is weaker than the other, and this beam is further attenuated by a factor of 100 with a neutral density filter. Both beams then pass through a biconvex lens of focal length 30 cm. The two beams cross at a point within the fluid flow as they pass through the test section. On the other side of the tunnel, the weaker beam passes through an aperture 1 mm in diameter and enters a photomultiplier tube. Here the light from the weak 'reference' beam is mixed with light from the brighter beam which has been scattered from the volume in which the two beams intersect. This scattered light is Doppler shifted by the motion of the scattering particles, which are assumed to move with the local fluid velocity. Thus the scattered light has a slightly different frequency from the reference light and the combination of the two produces a beat frequency in the photomultiplier tube. This beat frequency is directly proportional to one component of the fluid velocity. For a more thorough explanation of the LDV principle, see Goldstein (1967), Adrian (1972) or Wang (1972).

The beat frequency from the photomultiplier is amplified and band-pass filtered to remove noise outside the frequency range of interest. The signal is then further amplified and clipped to eliminate most of the random amplitude modulation of the raw Doppler signal. The clipped signal is fed into a phase-locked loop, which produces a continuous square wave of the same frequency as the Doppler signal. The phase-locked loop reduces the effect of momentary signal dropouts which are caused by fluctuations in the number of scattering particles in the focal volume. The phase-locked loop can be used in the LDV system as long as the turbulence level does not exceed 12 %. At higher turbulence levels, it cannot accurately track the fluctuations of the Doppler frequency.

The square-wave output of the phase-locked loop is fed into a digital counter which averages the Doppler frequency over a 10 s period. The counter frequency is then converted into a velocity averaged over the same period. The square-wave signal also goes to the input of a frequency-to-voltage converter (Anadex model PI-408R). This device produces an analog voltage proportional to the

Doppler frequency and thus to the velocity. The converter averages the frequency over about fifty periods, so that the resulting instantaneous velocity signal has a bandwidth of from 0 to $\frac{1}{50}$ of the Doppler frequency. The velocity signal is fed into an r.m.s. voltmeter to measure the turbulence intensity.

The accuracy of any LDV system is limited by what is known as 'ambiguity noise' (George 1972). This is a broadening of the Doppler signal spectrum, or noise on the demodulated velocity signal, which has three causes: (i) mean velocity gradients across the LDV focal volume, (ii) turbulent fluctuations within the focal volume and (iii) the finite time of transit of scattering particles passing through the focal volume. Ambiguity noise limits the accuracy of measurements of velocity fluctuations, but has no effect upon mean velocity measurements. For the focal volume used in the present experiment, which is approximately $1 \times 0{\cdot}05 \times 0{\cdot}05$ mm, the noise produced by (ii) is negligible. Noise from (i) may be significant in the high shear region in the core of the vortex, but a more important cause of measured velocity fluctuations in this region is the 'vortex wandering', which is discussed below. Noise from (iii) will be the same in laminar as in turbulent flow for a given focal volume, and has been measured in the laboratory. This component of the ambiguity noise is equivalent to a turbulence level of 0·25 %, which is thus the resolution limit of the system for velocity fluctuations.

2.3. *Experimental results*

The present series of measurements included axial and tangential velocity profiles in the vortex wakes behind two different model hydrofoils at distances of from five to sixty chord lengths downstream. The axial velocity component was measured directly by aligning the LDV with the free-stream flow. To obtain the tangential component, the velocity component at a 45° angle to the free stream was measured with the LDV, and this was used together with the axial velocity to compute the tangential velocity.† Velocity traverses at each downstream station were made in the horizontal plane, starting well out in the free stream and proceeding inwards to a point past the centre of the span of the model. Each mean velocity measurement represents a 30 s average, which was found to give extremely repeatable results.

Figure 2 shows typical velocity data for the model with square tips. Shown on this figure are axial and tangential velocity profiles for two values of x/c (distance downstream divided by chord length), and profiles of the axial fluctuations. Flow visualization studies suggest that these measured velocity fluctuations may be caused primarily by the random motion or wandering of the trailing vortex about the measurement point. The velocity gradients near the core of the vortex are high, so that the relatively small motions of the vortex can produce large velocity fluctuations. The degree of vortex wandering and its effect upon the measured velocities will be discussed in § 3.

† The tangential component could not be measured directly by aligning the LDV at 90° to the free-stream flow, because the mean tangential velocity passes through zero at the centre of the vortex. The LDV measures the magnitude but not the sign of the velocity, so that velocities with near zero mean are very difficult to measure unless frequency biasing is used.

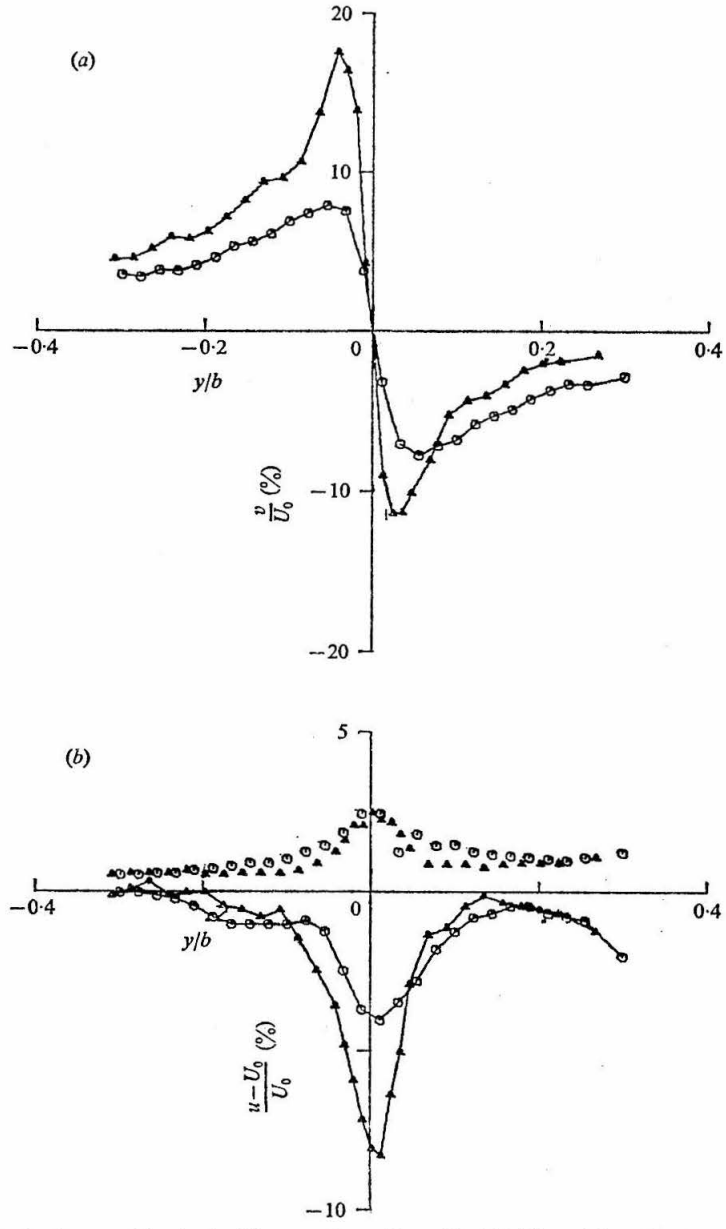

FIGURE 2. Velocity profiles in trailing vortex. $R_c = 22000$, $U_0 = 90$ cm/s, $\alpha = 10°$, aspect ratio = 6·18, wing span $b = 15{\cdot}24$ cm. ▲, $x/c = 10$; ●, $x/c = 20$. (*a*) Tangential velocity. (*b*) Axial velocity defect (lower points) and fluctuations (upper points).

The repeatability and small scatter of the data in this experiment show that the use of the LDV in a water tunnel is a practical means of measuring velocities in trailing vortices. The next step in this experimental programme will be to find to what extent the vortex wandering phenomenon is caused by free-stream

turbulence. This will be done by reducing the turbulence level of the water tunnel below its present value of 0·5% with the use of additional flow straighteners.

3. Theory and analysis

3.1. *Trailing vortex theory*

We now compare the experimental data with the available theory. Moore & Saffman (1973, hereafter referred to as I) have recently given a theory for the structure of laminar trailing vortices. For the case where the wing loading varies like the square root of the distance from the wing tip, the tangential velocity near the centre of the vortex is given by

$$v(r,x) = \beta\Gamma(\tfrac{5}{4})r(4\nu x/U_0)^{-\frac{3}{4}}M(\tfrac{3}{4};\,2;\,-U_0r^2/4\nu x). \tag{1}$$

Here r is the radial distance from the axis of the vortex, x is the distance downstream of the wing, ν is the kinematic viscosity, U_0 is the free-stream velocity or speed of the wing and M is the confluent hypergeometric function (Abramovitz & Stegun 1965, p. 503). The quantity β is related to the wing loading and mechanism of roll-up. We shall use the estimate, which incorporates a correction for finite aspect ratio exact for elliptic loading,

$$\beta = \frac{6^{\frac{1}{2}}}{2}U_0\alpha\frac{c}{b^{\frac{1}{2}}}\left(1+\frac{\pi c}{2b}\right)^{-1} \tag{2}$$

with α measured in radians, where c is the chord length and b the span. This value corresponds to an elliptically loaded thin wing, the root section having a lift coefficient of $2\pi\alpha$, with the 'contraction factor' λ set equal to 1·5. (See I for further details, but note that a larger value of β was used there for comparison with Olsen's (1971) towing-tank data, corresponding to the solution of the lifting line theory equation for a semi-infinite rectangular wing. The present experiments indicate that (2) is a better estimate, as should be the case for an aspect ratio of 6.)

The radius r_1 of the vortex core is defined as the value of r for which v is a maximum:

$$r_1 = 2{\cdot}92(\nu x/U_0)^{\frac{1}{2}}. \tag{3}$$

The maximum tangential velocity v_1 is given by

$$v_1 = 0{\cdot}49\beta(\nu x/U_0)^{-\frac{1}{4}}. \tag{4}$$

The axial vorticity ξ on the axis is $2\partial v/\partial r$ evaluated $r = 0$, and is given by

$$\xi = \frac{\Gamma(\frac{5}{4})}{2^{\frac{1}{2}}}\beta\left(\frac{\nu x}{U_0}\right)^{-\frac{3}{4}}. \tag{5}$$

The axial velocity $u(r,x)$, measured relative to the free stream, is the sum of two terms. The first term u_v is due to the pressure field induced by the roll-up and

decay of each trailing vortex. The second term u_δ is a velocity defect due to retardation in the boundary layer (of thickness δ) on the wing. Thus,

$$u(r,x) = u_v + u_\delta$$
$$= \frac{\beta^2}{U_0}\left(\frac{\nu x}{U_0}\right)^{-\frac{1}{2}} W_{\frac{1}{2}} - 0{\cdot}21 U_0 \delta \left(\frac{\nu x}{U_0}\right)^{-\frac{1}{2}} M\left(\tfrac{1}{2};\, 1;\, \frac{-U_0 r^2}{4\nu x}\right). \tag{6}$$

$W_{\frac{1}{2}}$ is a function of $U_0 r^2/4\nu x$. It can be expressed as an integral of confluent hypergeometric functions; a plot is given in I, figure 3(*a*). Note that $W_{\frac{1}{2}}(0) = -0{\cdot}13$, $W_{\frac{1}{2}}$ is positive for $r > 1{\cdot}4(\nu x/U_0)^{\frac{1}{2}}$ and $W_{\frac{1}{2}} \sim (\nu x/U_0 r^2)^{\frac{1}{2}}$ for large values of the argument. The flux deficit per unit span in the boundary layer is $U_0\delta$. The above expression is for a rectangular wing, for which δ is assumed independent of the spanwise station. In I it was assumed that δ is given by the momentum thickness δ_2 of a Blasius boundary layer, i.e. $\delta_2 = 1{\cdot}33(\nu c/U_0)^{\frac{1}{2}}$. However, arguments were given [see I, paragraph following equation (3.29)] that the displacement thickness might be more appropriate for the axial velocity on the axis of the vortex, i.e. $\delta_1 = 3{\cdot}44(\nu c/U_0)^{\frac{1}{2}}$. The velocity on the axis is written as ΔU, where

$$\Delta U = \Delta U_v + \Delta U_\delta = -0{\cdot}13\frac{\beta^2}{U_0}\left(\frac{U_0}{\nu x}\right)^{\frac{1}{2}} - U_0\chi\left(\frac{c}{x}\right)^{\frac{1}{2}}. \tag{7}$$

Here $\chi = 0{\cdot}28$ or $0{\cdot}72$ depending on whether the momentum or displacement thickness is used in estimating the boundary-layer retardation.

3.2. *Vortex wandering*

These predictions cannot be compared directly with experiment because the vortex is observed to wander in a random manner. The measured profiles are time averages at positions fixed relative to the wing, and are therefore weighted averages of the instantaneous profiles (1) and (6). It is believed that the vortex wandering is due mainly to free-stream turbulence,† so that the predictions can be corrected for the purpose of comparison with the experimental data.

We expect the turbulence to be equivalent to an eddy diffusivity κ. Then the axis of the vortex will fluctuate randomly about its mean position in a transverse plane at given x with a probability density

$$p(\eta,\zeta) = (1/2\pi\sigma^2)\exp\left[-(\eta^2+\zeta^2)/2\sigma^2\right], \tag{8}$$

where

$$\sigma^2 = 2\kappa x/U_0. \tag{9}$$

We have determined κ in an approximate manner by enlarging photographs of a vortex marked with dye and measuring the mean-square displacement of the axis. There is considerable scatter, but this procedure gave values for the ratio ν/κ of about 0·4 for $U_0 = 30$ cm/s and about 0·2 for $U_0 = 90$ cm/s.

We assume that the theoretical profiles (1) and (6) are valid instantaneously relative to the instantaneous position of the axis. Then observed quantities are

† The same degree of wandering was observed for a stream of dye released from the model in a zero-lift configuration. Preliminary measurements with reduced free-stream turbulence showed significantly less vortex wandering. Far downstream, some wandering may be due to the mutual instability of the two trailing vortices, but estimates of this effect suggest that it is negligible for the present values of x/c.

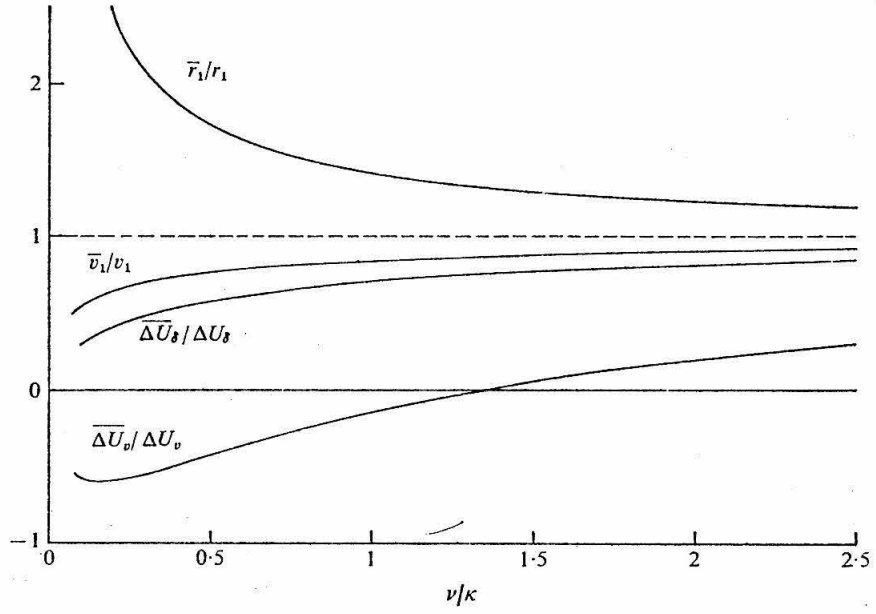

FIGURE 3. Effect of vortex wandering on core radius, maximum tangential velocity, and axial velocity on the mean axis.

averages, denoted by overbars, over the wandering of the vortex axis. Thus for the axial velocity

$$\bar{u}(r,x) = \iint u\{[(r-\eta)^2+\zeta^2]^{\frac{1}{2}},x\}\,p(\eta,\zeta)\,d\eta\,d\zeta \tag{10}$$

and for the tangential velocity

$$\bar{v}(r,x) = \iint \frac{\eta-r}{[(r-\eta)^2+\zeta^2]^{\frac{1}{2}}}\,v\{[(r-\eta)^2+\zeta^2]^{\frac{1}{2}},x\}\,p(\eta,\zeta)\,d\eta\,d\zeta, \tag{11}$$

where r in these expressions is measured from the mean position of the axis. The extra term in (11) arises from the need to incorporate a geometrical factor.

Substituting for $p(\eta,\zeta)$ from (8) and for u and v from (6) and (1), the integrals can be reduced to single integrals involving modified Bessel functions and confluent hypergeometric functions, which can be put into dimensionless form as functions of x/c, $U_0 r^2/\nu x$ and ν/κ. These integrals can be evaluated by standard techniques; details of the calculation are available from the first listed author.

The effect of vortex wandering is to broaden the profiles and reduce the magnitude of the variations. In figure 3 we show values of the ratios $\bar{r}_1/r_1$ and $\bar{v}_1/v_1$ as functions of ν/κ. We define $\bar{r}_1$ as the value of r for which $\bar{v}$ attains its maximum $\bar{v}_1$. We also show the contributions $\overline{\Delta U_v}/\Delta U_v$ and $\overline{\Delta U_\delta}/\Delta U_\delta$ to the axial velocity on the mean centre-line.

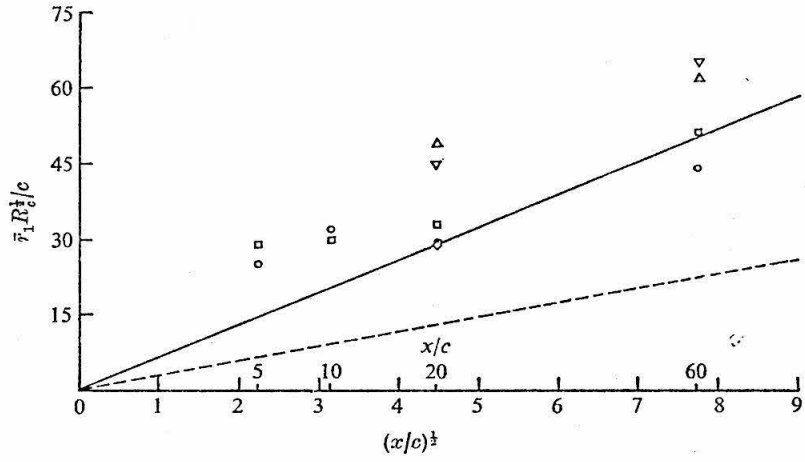

FIGURE 4. Dimensionless core radius as function of downstream distance. ----, instantaneous values [equation (3)]; ———, predictions averaged over vortex wandering for $\nu/\kappa = 0{\cdot}25$. Model 1, square-tip planform; model 2, round-tip planform.

	○	△	▽	□	◇
Model	1	1	1	2	2
$R_c \times 10^{-4}$	2·2	7·0	7·0	2·2	0·75
α (deg)	10	10	5	10	10

3.3. *Comparison with experiment*

We expect κ to be a function of the tunnel Reynolds number, but since the estimate is rough, the refinement of employing different values for different tunnel speeds is uncalled for at the present stage. We have therefore used one typical value of the ratio ν/κ, namely 0·25, in the comparisons between theory and experiment shown in figures 4–7. There does not seem to be any significant difference between the two model hydrofoils.

Figure 4 shows predicted and measured values of $\bar{r}_1 R_c^{\frac{1}{2}}/c$, where $R_c \equiv U_0 c/\nu$, as a function of $(x/c)^{\frac{1}{2}}$. Both the predicted values averaged over the vortex wandering (for $\nu/\kappa = 0{\cdot}25$) and the instantaneous predictions are shown. The experimental values of $\bar{r}_1$ are given by half the distance between the tangential velocity peaks. The agreement is reasonable in view of the experimental uncertainty in measuring $\bar{r}_1$ from data such as those shown in figure 2. In addition, the experiments show a lack of circular symmetry in the vortex structure, which is expected on theoretical grounds from detailed studies of the roll-up process (Saffman 1974), but cannot at present be incorporated in the analysis of the vortex structure given in I. We emphasize that ν/κ was chosen on the basis of an independent measurement of the free-stream turbulence. The effect of vortex wandering upon the data is seen to be very significant.

Figure 5 shows $\bar{v}_1 R_c^{-\frac{1}{4}}/U_0\alpha$ as a function of $(x/c)^{-\frac{1}{4}}$. The estimate of equation (2) for β was employed. Both values averaged over the vortex wandering and instantaneous values are shown. The agreement is again reasonable except that there is a tendency for the theory to overestimate the velocity and axial vorticity, particularly for small values of x/c. In this connexion, it should be kept in mind

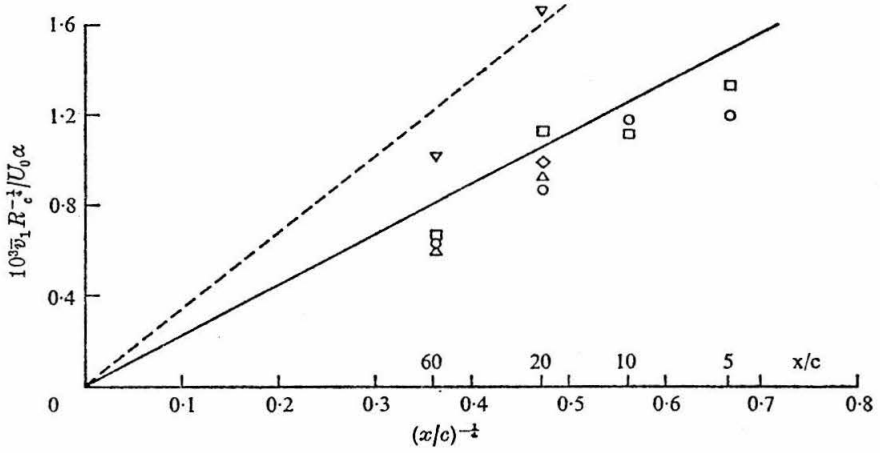

FIGURE 5. Dimensionless maximum tangential velocity velocity *vs.* downstream distance. ----, instantaneous values; ——, predictions averaged over vortex wandering. α measured in degrees. Symbols as in figure 4.

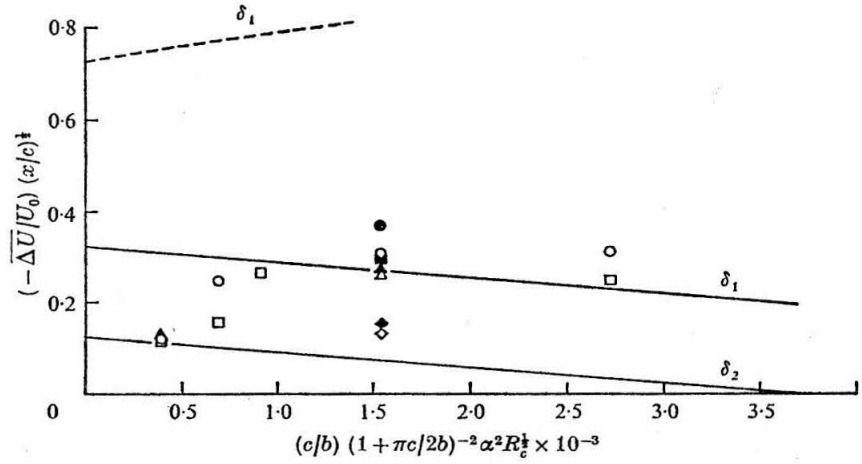

FIGURE 6. Axial velocity defect on mean axis as function of angle of attack, chord Reynolds number and aspect ratio. ----, instantaneous values (equations (7) and (2), using displacement thickness); ——, predictions averaged over vortex wandering for $\nu/\kappa = 0{\cdot}25$ using δ_1 and δ_2. Intercepts are at $\alpha^2 R_c^{\frac{1}{2}} = 8{\cdot}9 \times 10^5$ and $3{\cdot}5 \times 10^5$ for an aspect ratio of 6·18. α measured in degrees.

Model 1	◇	△	□	○
Model 2	◆	▲	■	●
x/c	5	10	20	60

that the theory is an approximation formally valid in the limit of light loading and/or large downstream distances. Radial velocities in the cores are neglected, and these will be most important close to the wing. Also, our choice of β is not free from uncertainty.

Figure 6 shows the axial velocity defect. We have plotted $(\overline{\Delta U}/U_0)(x/c)^{\frac{1}{2}}$ *vs.* $\alpha^2 R_c^{\frac{1}{2}}(c/b)(1+0{\cdot}5\pi c/b)^{-2}$. There is some arbitrariness in the choice of δ. It appears

	Uncorrected		Corrected for free-stream turbulence level of 1 %	
x/c	$\delta = \delta_1$	δ_2	δ_1	δ_2
10	0·0625	0·031	0·063	0·0325
60	0·0255	0·0125	0·0275	0·016

TABLE 1

that δ_1 is marginally better than δ_2. The instantaneous value of ΔU is shown with δ_1. The agreement is encouraging, and demonstrates again the importance of allowing for vortex wandering in the interpretation of experimental data. In particular, the slope of the theoretical line is reversed, and excess average velocities are predicted at the centre of the vortex when $\alpha^2 R_c^{\frac{1}{2}} \geqslant 8{\cdot}9 \times 10^4$, using δ_1 for the boundary-layer retardation with $b/c = 6{\cdot}18$. In this flow there would be a large instantaneous axial velocity deficit as measured, say, by flow visualization techniques. The data from figure 4 of Orloff & Grant (1973) fall on the extrapolation of the curve representing averages over the vortex wandering shown in our figure 6, using δ_1, for abscissa values of about 100. The value of ν/κ of 0·25 determined in the present experiment leads also to predictions of tangential velocity consistent with the data of Orloff & Grant's figure 3.

Finally, we have computed the apparent turbulence intensity of the axial velocity due to vortex wandering. We calculated

$$\overline{u^2(r,x)} = \iint \{u([(r-\eta)^2+\zeta^2]^{\frac{1}{2}},x)\}^2 p(\eta,\zeta)\,d\eta\,d\zeta, \tag{12}$$

using the profile of (6) in the integrand. Then the apparent turbulence intensity is

$$(\overline{u'^2})^{\frac{1}{2}}/U_0 = \{\overline{u^2(r,x)} - [\overline{u}(r,x)]^2\}^{\frac{1}{2}}/U_0. \tag{13}$$

The predicted turbulence levels on the mean axis are shown in table 1 for the experimental case of figure 2. The second set of values in table 1 has been corrected for a free-stream turbulence level of 1 %, assuming statistical independence.

Since the measured values of the turbulence level shown in figure 2 do not seem to depend upon x/c and the theoretical predictions behave as $(x/c)^{-\frac{1}{2}}$, there cannot be complete agreement. However, since the theory is likely to be more valid for $x/c = 60$, we see that the predicted value there of 0·0275 using δ_1 is close to the experimentally measured value.

The authors are indebted to the U.S. Air Force Office of Scientific Research for their support of this work.

REFERENCES

ABRAMOVITZ, M. & STEGUN, I. A. 1965 *Handbook of Mathematical Functions*. Dover.

ADRIAN, R. 1972 *J. Phys.* E, *Sci. Instrum.* **5**, 91.

CAIGER, B. & GOULD, D. 1971 An analysis of flight measurements in the wake of a jet transport aircraft. In *Aircraft Wake Turbulence and its Detection* (ed. Olsen), pp. 125–136. Plenum.

CHEVALIER, H. 1973 *J. Aircraft*, **10**, 14.

GEORGE, W. 1972 Limitations on the measurement of unsteady flow velocities with a laser doppler velocimeter. In *Proc. DISA Conf. on Flow in Industrial & Medical Environments* (ed. Cockrell), pp. 88–99. Leicester University Press.

GOLDSTEIN, R. 1967 *Phys. Fluids*, **10**, 1349.

KNAPP, R. & LEVY, J. 1948 The hydrodynamics laboratory of the California Institute of Technology. *Trans. A.S.M.E.*, p. 437.

LEZIUS, D. 1973 Study of the far wake vortex field generated by a rectangular airfoil in a water tank. *A.I.A.A. Paper*, no. 73-682.

MASON, H. & MARCHMAN, J. 1972 The farfield structure of aircraft wake turbulence. *A.I.A.A. Paper*, no. 72-40.

MILLER, E. & BROWN, C. 1971 An experimental study of trailing vortex wakes using a large towing tank. *HYDRONAUTICS Tech. Rep.* no. 7105-1.

MOORE, D. W. & SAFFMAN, P. G. 1973 *Proc. Roy. Soc.* A **333**, 491–508.

OLSEN, J. H. 1971 Results of trailing vortex studies in a towing tank. In *Aircraft Wake Turbulence and its Detection*, pp. 455–472. Plenum.

ORLOFF, K. & GRANT, G. 1973 The application of a scanning laser-doppler velocimeter to trailing vortex definition and alleviation. *A.I.A.A. Paper*, no. 73-680.

SAFFMAN, P. G. 1974 The structure and decay of trailing vortices. (To be published.)

WANG, C. 1972 *Appl. Phys. Lett.* **20**, 339.

REFERENCES

Alder, B., Fernbach, S. and Rotenberg, M. Eds. 1970 Methods of Computational Physics, 9. Academic Press.

Baker, G.R., Saffman, P.G. and Sheffield, J.S. 1976 Structure of a linear array of hollow vortices of finite cross-section. J.F.M. 74, 469-476.

Batchelor, G.K. 1970 An Introduction to Fluid Dynamics. Cambridge University Press.

Birkhoff, G.D. and Fisher, J. 1959 Do vortex sheets roll up? Rc. Circ. mat. Palermo Ser 2, 8, 77-90.

Bofah, K.K. 1975 A study of the trailing vortices behind a ring wing. Ph. D. Thesis. California Inst. of Tech.

Brown, G.L. and Roshko, A. 1974 On density effects and large structure in turbulent mixing layers. J.F.M. 64, 775-816.

Chorin, A.J. and Bernard, P.S. 1972 Discretization of a vortex sheet, with an example of a roll-up. Univ. California, Berkeley Engng. Rep. FM-72-5.

Christiansen, J.P. 1973 Numerical simulation of hydrodynamics by the method of point vortices. J. Comp. Phys. 13, 363-379.

Christiansen, J.P. and Zabusky, N.J. 1973 Instability, coalescence and fission of finite-core vortex structures. J.F.M. 61, 219-243.

Crow, S.C. 1974 Motion of a vortex pair in a stably stratified fluid. Poseidon Research Rep. no. 1, Poseidon Research, Los Angeles, California.

Fink, P.T. and Soh, W.K. 1974 Calculation of vortex sheets in unsteady flow and applications in ship hydrodynamics. Tenth Symp. Naval Hydrodynamics. Cambridge, Mass.

Freymuth, P. 1966 On transition in a separated laminar boundary layer. J.F.M. 25, 683-704.

Hill, F.M. 1975a Ph. D. Thesis. Imperial College, London.

Hill, F.M. 1975b A numerical study of the descent of a vortex pair in a stably stratified atmosphere. J.F.M.

REFERENCES (cont.)

71, 1-13.

Hockney, R.W. 1970 The potential calculation and some applications. in Methods of Computational Physics, 9. Eds. Alder, B., Fernbach, S. and Rotenberg, M. Academic Press.

Isaacson, E. and Keller, H.B. 1966 Analysis of Numerical Methods. Wiley.

Jeffreys, H. and Jeffreys, B.S. 1950 Methods of Mathematical Physics. Cambridge University Press.

Kaden, H. 1931 Aufwicklung einer unstabilen unstetigkeitsflache. Ing. Archiv. 2, 140. (English trans. R.A.E. Library Trans. no. 403.)

Kuwahara, K. and Takami, H. 1973 Numerical studies of two-dimensional vortex motion by a system of point vortices. J. Phys. Soc. Japan 34, 247-253.

Lamb, H. 1932 Hydrodynamics, 6th edn. Cambridge University Press.

Maskew, B. to be published in J. of Aircraft.

Moore, D.W. 1971 The discrete vortex approximation of a vortex sheet. California Inst. of Tech. Rep. AFOSR-1084-69.

Moore, D.W. 1974 A numerical study of the roll-up of a finite vortex sheet. J.F.M. 63, 225-235.

Moore, D.W. 1975 The rolling up of a semi-infinite vortex sheet. Proc. Roy. Soc. A345, 417-430.

Moore, D.W. and Griffith-Jones, R. 1974 The stability of an expanding circular vortex sheet. Mathematika 21, 128-133.

Moore, D.W. and Saffman, P.G. 1971 Structure of a line vortex in an imposed strain. in Aircraft Wake Turbulence and its Detection. Eds. Olsen, Goldberg, Rogers. p. 339-354.

Moore, D.W. and Saffman, P.G. 1973 Axial flow in laminar trailing vortices. Proc. Roy. Soc. A333, 491-508.

REFERENCES (cont.)

Moore, D.W. and Saffman, P.G. 1975 The density of organized vortices in a turbulent mixing layer. J.F.M. 69, 465-473.

Morse, P.M. and Feshbach, H. 1953 Methods of Theoretical Physics. McGraw-Hill.

Narain, J.P. and Uberoi, M.S. 1974 The motion of a trailing vortex-wake in a stratified medium. Atmospheric Environment 8, 459-473.

Patnaik, P.C., Sherman, F.S. and Corcos, G.M. 1976 A numerical simulation of Kelvin-Helmholtz waves of finite amplitude. J.F.M. 73, 215-240.

Pierce, D. 1966 Photographic evidence of the formation and growth of vorticity behind plates accelerated from rest in still air. J.F.M. 11, 460.

Rosenhead, L. 1931 Formation of vortices from a surface of discontinuity. Proc. Roy. So. A134, 170-192.

Saffman, P.G. 1972 The motion of a vortex-pair in a stratified atmosphere. Stud. Appl. Math. LI, 107-119.

Scorer, R.S. and Davenport, L.J. 1970 Contrails and aircraft downwash. J.F.M. 43, 451-464.

Takami, H. 1964 Numerical experiment with discrete vortex approximation, with reference to the rolling up of a vortex sheet. Dept. Aero. and Astronaut. Stanford Univ. Rep. SUDAER 202.

Tombach, I.H. 1971 Transport of a vortex wake in stably stratified atmosphere. in Aircraft Wake Turbulence and its Detection, 41-56. Plenum Press, New York.

Turner, J.S. 1960 A comparison between buoyant vortex rings and vortex-pairs. J.F.M. 7, 419-432.

Westwater, F.L. 1935 Rolling up of the surface of discontinuity behind an aerofoil of finite span. Aero. Res. Counc. R & M. no. 1962.

Winant, C.D. and Brownand, F.K. 1974 Vortex pairing; the mechanism of turbulent mixing layer growth at moderate Reynolds number. J.F.M. 63, 237-255.